INFORMATION TO USERS

This manuscript has been reproduced from the microfilm master. UMI films the text directly from the original or copy submitted. Thus, some thesis and dissertation copies are in typewriter face, while others may be from any type of computer printer.

The quality of this reproduction is dependent upon the quality of the copy submitted. Broken or indistinct print, colored or poor quality illustrations and photographs, print bleedthrough, substandard margins, and improper alignment can adversely affect reproduction.

In the unlikely event that the author did not send UMI a complete manuscript and there are missing pages, these will be noted. Also, if unauthorized copyright material had to be removed, a note will indicate the deletion.

Oversize materials (e.g., maps, drawings, charts) are reproduced by sectioning the original, beginning at the upper left-hand corner and continuing from left to right in equal sections with small overlaps. Each original is also photographed in one exposure and is included in reduced form at the back of the book.

Photographs included in the original manuscript have been reproduced xerographically in this copy. Higher quality 6" x 9" black and white photographic prints are available for any photographs or illustrations appearing in this copy for an additional charge. Contact UMI directly to order.

UMI

A Bell & Howell Information Company
300 North Zeeb Road, Ann Arbor MI 48106-1346 USA
313/761-4700 800/521-0600

Downloaded from SHAREOK. Persistent Handle URL: https://hdl.handle.net/11244/5602

UNIVERSITY OF OKLAHOMA

GRADUATE COLLEGE

Abundances in Planetary Nebulae
An Autopsy of Low and Intermediate Mass Stars

A Dissertation

SUBMITTED TO THE GRADUATE FACULTY

In partial fulfillment of the requirements
for the degree of

Doctor of Philosophy

by

JAMES F. BUELL

Norman, Oklahoma
1997

UMI Number: 9822818

UMI Microform 9822818
Copyright 1998, by UMI Company. All rights reserved.

This microform edition is protected against unauthorized
copying under Title 17, United States Code.

UMI
300 North Zeeb Road
Ann Arbor, MI 48103

© James F. Buell 1997
ALL RIGHTS RESERVED

ABUNDANCES IN PLANETARY NEBULAE: AUTOPSIES OF LOW AND INTERMEDIATE MASS STARS

A Dissertation APPROVED FOR THE
DEPARTMENT OF PHYSICS AND ASTRONOMY

BY

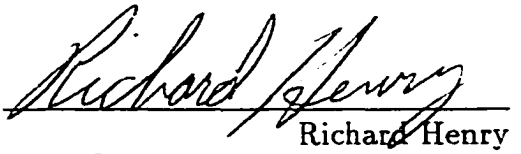

Richard Henry

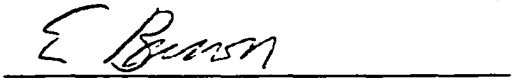

Edward Baron

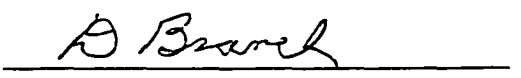

David Branch



Marilyn Ogilvie



William Romanishin

Acknowledgments

I wish to express appreciation for those people who have directly or indirectly supported this work.

First, I wish to acknowledge my wife Brenda without whose love and support this work would not have been possible.

I would also like to thank the faculty of the Department of Physics and Astronomy at the University of Oklahoma for supporting me through my years of study. In particular, I would like to thank my advisor, Dr. Henry, for allowing me to work independently. I would like to thank Dr. Baron for teaching me all about stellar evolution and always taking the time to answer my questions. I would like to thank Dr. Branch for always giving me an answer and asking very probing questions.

I would also like to thank Drs. Alvio Renzini, Arnold Boothroyd, and Grant Bazan for providing me with valuable information

Finally, I would like to thank the secretaries and the staff of the physics department for their help.

Contents

1 Introduction **1**
- 1.1 The Importance of Stellar Evolution 2
- 1.2 The Importance of Population 7
- 1.3 Thesis Goals 8

2 Multivariate Data Analysis **9**
- 2.1 The Sample 11
- 2.2 Multivariate Data Analysis 12
  - 2.2.1 Principal Components Analysis 12
  - 2.2.2 Cluster Analysis 15
- 2.3 Results and Discussion 16
  - 2.3.1 Results of Principal Components Analysis 16
  - 2.3.2 Results of Cluster Analysis 22
- 2.4 Discussion 30
- 2.5 Conclusions 35

3 Thermally Pulsing AGB Models **37**
- 3.1 Models 39
  - 3.1.1 The Structure of the Envelope 39
  - 3.1.2 Mass Loss on the AGB 40
  - 3.1.3 Surface Luminosity 42
  - 3.1.4 The Third Dredge Up 51
  - 3.1.5 Other Third Dredge-Up Parameters 56
  - 3.1.6 Conditions at the First Pulse 57
  - 3.1.7 Core Mass 61

4 Model Predictions of Element Production in Intermediate-Mass Stars **62**
- 4.1 Effect of Mass and Metallicity on Element Production 63
- 4.2 Summary of Results 74
  - 4.2.1 The Importance of Mixing Length 75

5 The Galaxy **80**
5.1 Data Sets Used 80
5.2 Metallicity of Galactic PNe 81
5.3 Comparison of Models to Data 84
5.3.1 He/H vs. N/O 84
5.3.2 He/H vs. C/O 92
5.3.3 Other Diagrams 102
5.4 Summary 103
5.5 Discussion 104
5.5.1 Correlations with Mass and Core-Mass 104
5.5.2 Hot-bottom Burning 105
5.6 Comparison to Other Models 107

6 On the Origin of Planetary Nebula K648 in Globular Cluster M15 109
6.1 Introduction 109
6.2 Models 112
6.3 Results and Discussion 114
6.3.1 Observational Parameters 114
6.3.2 Delayed Scenario 117
6.3.3 Prompt Scenario 121
6.4 Discussion 124

7 Conclusions **126**
7.1 Future Work 128

A Model Results **129**

B Yields **136**

List of Figures

2.1 The correlation vector diagrams generated by our PCA runs. The diagrams are labeled as follows: (a) The unrotated diagram for the bulge PNe subset, (b) the rotated diagram for the bulge PNe, (c) the rotated diagram for the disk PNe subset, and (d) the rotated diagram for our bulge and disk PNe set. In each diagram the distance from the origin to the end of the dotted line is 0.6. It should be noted that it was impossible to get the angles between the vectors exactly correct due to limitations of our plotting package. 19

2.2 The dendridic diagram generated by our cluster analysis using the parameters R. V_{LSR}, He, N, O, Ne, and N/O. The branches where each of the clusters and subclusters are located are labeled. 23

2.3 Cluster comparison diagram for log(He/H)+12 versus log(N/O). Cluster membership of each PN is indicated by a number. Members of subcluster 1b are indicated by circled 1's, members of 3b by circled 3's and members of 3c by a 3 enclosed by a diamond. The solar values are indicated by the solid square. 26

2.4 Cluster comparison diagram for log(Ne/H)+12 versus log(O/H)+12. The symbols have the same meaning as in figure 2.3. 27

2.5 Cluster comparison diagram for log(O/H)+12 versus log(N/H)+12. The symbols have the same meaning as in figure 2.3. 28

2.6 log(He/H)+12 versus log(N/O) for bulge and disk PNe. The filled symbols represent the bulge objects and the open symbols the disk objects. The circles represent the cluster 1 objects and the squares the non-cluster 1 objects. The two PNe of cluster 3c have been removed. 31

2.7 log(Ne/H)+12 versus log(O/H)+12 for bulge and disk PNe. The symbols have the same meaning as in the previous graph. The line is a least squares fit to the data. 34

3.1 Shown in the figure is the interpulse luminosity at the time of the first thermal pulse as a function of core-mass. The Z=0.02, 0.01, and 0.0044 models of Boothroyd and Sackmann (1992) are respectively shown by circles, squares, and stars. The solid line is a least squares fit to the Z=0.02 models. 45

3.2 The initial rate of rise is shown as a function of core-mass. No metallicity dependence is shown. The two component fit to the data is shown. 47
3.3 The mass correction factor f is plotted versus mass for the Boothroyd and Sackmann models. The solid line is our fit to the asymptotic value of f. 49
3.4 The behavior of the interpulse surface luminosity of a 5 $M_\odot$, solar metallicity model, and mixing length parameter α=2.0 model. M_H is the mass of the hydrogen exhausted core. The open circles indicated the luminosities of each interpulse. The solid line indicates the low-mass core-mass luminosity relationship of Boothroyd and Sackmann 1988b. The text on the page indicates the model stars total mass at various points. 50
3.5 The fraction of each interpulse spent below 75% of the maximum luminosity achieved during each interpulse. The line is a least squares fit to the data, and the points are models obtained from table 3 of BS88a 52
3.6 The minimum luminosity of the helium burning shell during a thermal pulse required for dredge-up to occur. 55

4.1 Expected value of He/H in PN for model mass between $1M_\odot$ and $8M_\odot$. The solid line, dashed line, long dashed line and the dotted line respectively indicate models calculated with [Fe/H]=0.0, 0.1, 0.2, and -0.1. The dashed-dotted line indicates the abundance of He/H at the first pulse for the [Fe/H]=0.0 model. 65
4.2 The panels from top to bottom indicate the time the model spends on the TP-AGB, the number of pulses, and the maximum base temperature achieved at the bottom of the convective envelope. The lines have the same meaning as figure 4.1 66
4.3 Same as figure 4.1 except N/O is compared to ZAMS mass. 72
4.4 Same as figure 4.1 except C/O is compared to ZAMS mass. 73
4.5 Same as figure 4.1 except log O/H+12 is compared to ZAMS mass. 74
4.6 Behavior of He/H as a function of α and ZAMS mass. all models have [Fe/H]=0.0. The dotted, solid, and dashed lines indicate respectively model grids with the mixing length parameter, α, respectively set to 1.9, 2.3, and 2.5. 76
4.7 Same as figure 4.6 except C/O is compared to α and ZAMS mass. . 77
4.8 Same as figure 4.6 except N/O is compared to α and ZAMS mass. . 78
4.9 Same as figure 4.6 except O/H is compared to α and ZAMS mass. . 79

5.1 Distribution of the O/H abundance ratio of the Kingsburgh and Barlow (1994) and the HK PNe. The open bars indicate the distribution of all the PNe. The solid bars indicate the distribution of PNe with N/O>0.5. 82

5.2 Same as 5.1 except the distribution of Ne/H is shown. 83
5.3 Same as 5.1 except the distribution of Ar/H is shown. 83
5.4 The circles and squares represent the KB and HK data sets, respectively. Open and closed symbols respectively indicate PNe with N/O$\leq$0.5 and N/O>0.5, respectively. The solid, dashed, long-dashed, and dash-dotted lines refer to models calculated respectively with [Fe/H]=0.0, 0.1, 0.2, and -0.5. The mixing length parameter, α, of each model was set to 2.3. Only models with M<4.6$M_\odot$ are shown for the [Fe/H]=0.2 and only models with M<2$M_\odot$ are shown for the [Fe/H]= -0.5. The solid diamonds indicate the results of models with [Fe/H]=0.0 and masses of 1.0, 1.6, 2.5, 4.0, 4.1, 6.0, and 8.0 $M_\odot$. Also the position of the model with [Fe/H]=0.2 and mass of 4.6 $M_\odot$ is indicated. 86
5.5 The symbols and lines have the same meaning as they do in figure 5.4. Also included is a dotted line, which shows the predicted abundances for stars with [Fe/H]=-0.5 and masses of 0.9, 1.0, 1.1, and 1.2 $M_\odot$ using a first dredge-up model based on the recent results of Boothroyd and Sackmann (1997) as explained in the text. The light solid line is a rough approximation of the divide between the allowed and forbidden regions of the plane. The symbols with stars in them indicate PNe with C/O>0.8. Note that many objects do not have an observed C/O ratio. 88
5.6 The symbols have the same meaning as figure 5.4. The dotted line are the [Fe/H]=-1.0 models. 92
5.7 Superimposed on the grid of [Fe/H]=0.0 α=2.3 models are the masses of those models. 94
5.8 Galactic PNe plotted on the He/H-O/H plane. The symbols have the same meaning as in figure 5.4. 95
5.9 Same as figure 5.8 except the model curves have been shifted down by 0.25*dex* as indicated in the text. 96
5.10 Comparison of He/H vs Ne/H. The low and high N/O PNe are indicated by open and closed circles, respectively. Note that the maximum He/H for low N/O objects increases with Ne/H. 98
5.11 The symbols have the same meaning as in figure 5.10. Note the maximum He/H for low N/O objects increases with Ar/H. 99
5.12 Galactic PNe plotted on the C/O-Ne/H plane. The symbols have the same meaning they do in figure 5.4. Note the narrow range in Ne/H of PNe with C/O>1.0. 101
5.13 Comparison of models to data on the C/O to N/O plane. 102
5.14 103

6.1 Shown in the panels of this figure are the evolution of our thermally pulsing AGB models and the parameters of our prompt model. The dotted line and open squares track model 1, the solid line and open circles track model 2, and the solid diamonds are the parameters of the prompt model. The abscissa of the graphs tracks the mass of the models in solar masses. Due to mass loss the stars move from right to left on the graphs. The parameters in the panels are for the interpulse phase. From top to bottom the parameters are stellar luminosity (in $L_\odot$), radius (in $R_\odot$), the mass-loss rate (in $M_\odot$ yr^{-1}), and the mass of the core. The observed upper and lower limits of the AGB tip luminosity are indicated with dark long dashed lines, the lower limit on the AGB tip mass-loss rate is indicated with a long dashed line, and the upper and lower limits of the central star mass are indicated with long dashed lines. 118

6.2 Shown in the panels of this figure is the evolution of the surface abundance ratios. The symbols have the same meaning as the first figure. In the C/O panel the upper and lower observational limits are shown on the figure with the dark long dashed line. The range of possible He/H and N/O is encompassed by the ordinates of these figures. 121

List of Tables

2.1 Objects used in Multivariate Data Analysis 13
2.2 Residuals and Eigenvalues 17
2.3 Components of Vectors in the Rotated Bulge Parameter Space . . . 20
2.4 Components of Vectors in the Rotated Disk Parameter Space 20
2.5 Components of Vectors in the Rotated Bulge and Disk Parameter Space 21
2.6 Shows the breakdown of each subcluster into Peimbert types, bulge and disk members, and into objects with $V_{LSR} > 60$ km/s. Only composition criteria are used in the Peimbert scheme classification. 24
2.7 Shown in this table are the parameter averages for each PNe Cluster. 25

4.1 Table of Input Model Parameters 62

5.1 Comparison of our model enhancements of log N/O against those of Boothroyd and Sackmann (1997). Their calculations indicate enhancements in N/O depend mainly on mass and appear to depend only very weakly on metallicity at least in the mass range considered. 91

6.1 Observational Data for K648: This table is a summary of the observed and inferred parameters for PN K648. The effective temperature, T_{eff}, refers to the central star, while the distance, d, is the adopted distance to K648. The following nebular parameters are also listed: the angular size of the nebula, θ; the expansion velocity, v_{exp}; the electron density, n_e; the ionized gas temperature, T_e; and the log of the measured Hβ flux in erg cm^{-2} s^{-1}. The large range in θ and n_e arise from differences between newer HST data and ground based data, The HST data give higher a value of θ and a lower value for n_e. The references are as follows: (1) Adams et al. 1984; (2) Bianchi et al. 1995; (3) Durell and Harris 1993; (4) Acker et al. 1992; (5) Gathier et al. 1983 114

6.2 Observational Data and Models Compared: This table compares the observed and predicted parameters for PN K648. The observed luminosity, L, refers to the central star, while the predicted luminosity is the luminosity on the AGB, but since the tracks are nearly horizontal they should be comparable. The following nebular parameters are also listed: the mass of ionized gas in the nebula, M_{PN}; the mass of the central star, M_c; the dynamic timescale, τ_{dyn}; and the abundance ratios He/H, C/O, and N/O by number. The abundances for the prompt scenario are calculated assuming 0.00014 $M_\odot$ of helium and carbon rich material is removed by mass-loss from the CSPN. The observed value for the dynamical timescale, τ_{dyn}, corresponds to an upper limit for the age of the nebula. The theoretical values correspond to evolutionary time scales required to reach a given central star temperature. The large range in L and $M_{\rm PN}$ arise from differences between HST data and ground based radio and optical data. The HST data give higher values for L and $M_{\rm PN}$. References: (1) Adams et al. 1984; (2) Bianchi et al. 1995; (3) Henry, Kwitter, and Howard 1996; (4) Howard, Henry, and McCartney 1997 116

6.3 Input Parameters and Results for Delayed Models: Note, the masses are in $M_\odot$ 119

6.4 Adopted Prompt PN Ejection Parameters: The values in this table are estimated from figure 2 of BS88a for a 1.0 $M_\odot$, Z=0.001 model. All values are appropriate between point C and the vertical dashed line on this figure. The radius and luminosity are the estimated lower limits. The mass and core mass are taken from their listed values. The mass-loss rate is calculated from our mass-loss prescription. The time in this stage is estimated from the BS88a graph. 122

A.1 [Fe/H]=0.0 α=2.3 Galaxy 130
A.2 [Fe/H]=0.1 α=2.3 Galaxy 131
A.3 [Fe/H]=0.2 α=2.3 Galaxy 132
A.4 [Fe/H]=-0.1 α=2.3 Galaxy 133
A.5 [Fe/H]=-0.2 α=2.3 Galaxy 133
A.6 [Fe/H]=-0.5 α=2.3 Galaxy 134
A.7 [Fe/H]=-1.0 α=2.3 Galaxy 134
A.8 [Fe/H]=0.2 α=1.9 Galaxy 135
A.9 [Fe/H]=0.2 α=2.5 Galaxy 135

B.1 [Fe/H]= 0.0 and α= 1.90 136
B.2 [Fe/H]= 0.0 and α= 2.30 137
B.3 [Fe/H]= 0.1 and α= 2.30 138
B.4 [Fe/H]= 0.2 and α= 2.30 139
B.5 [Fe/H]=-0.1 and α= 2.30 140

B.6 [Fe/H]=-0.2 and α= 2.30 140
B.7 [Fe/H]=-0.5 and α= 2.30 141
B.8 [Fe/H]=-1.0 and α= 2.30 141
B.9 [Fe/H]= 0.0 and α= 2.50 142
B.10 [Fe/H]= 0.1 and α= 2.50 143
B.11 [Fe/H]= 0.2 and α= 2.50 144
B.12 [Fe/H]=-0.1 and α= 2.50 144

Chapter 1

Introduction

The planetary nebula (PN) phase is one of the final stages of stellar evolution for 1-8$M_{\odot}$ stars. A planetary nebula is created when an asymptotic giant branch (AGB) star sheds its hydrogen-rich envelope via stellar wind, exposing the underlying hot carbon-oxygen (CO) core. The surface of the remnant star has a surface temperature T>30000K and therefore it emits a significant number of photons with wavelengths, (λ), less than 912 Angstroms. These photons with energy greater than 13.6eV are sufficiently energetic to ionize hydrogen in the ejecta. The free electrons collisionally excite the ions in the nebula. The excited atoms then radiatively de-excite creating emission lines. PNe appear green in a small telescope or binoculars because of the [OIII]λ5007.

The energy input from the star is balanced by the energy emitted by lines from the nebulae. Photons from the star which photoionize the nebulae are the primary energy source. Emission lines carry this energy away. This energy balance determines the temperature of the nebulae and the relative numbers of each ionization stage of each atomic species.

PN emission lines can be used to determine to reasonable accuracy the nebular abundances of several atomic species. The density in most PNe is too low for ions to be collisionally de-excited. Therefore, these ions must emit one or more photons to get back to the ground state. By balancing the number of collisional excitations

with the number of radiative deexcitations, the abundance of some ionic species can be determined, e.g., using the [OIII]λ5007 line we can get the abundance of O^{+2}. To get the nebular abundance of an atom, an ionization correction factor is used to account for the unseen ionization stages. Therefore, the uncertainties in each element vary depending on how much of the element is in each stage. The procedure for determining elemental abundances is described in more detail in elementary textbooks on the subject (e.g. Osterbrock 1989).

Recently, detailed photoionization models have become widely available, allowing detailed calculations of the nebulae (i.e. CLOUDY). Such models improve our ability to determine nebular abundances.

The abundances of several important elements can be inferred for PNe. The list includes hydrogen, helium, carbon, nitrogen, oxygen, neon, sulfur, and argon. Some of these such as neon and argon can not be measured AGB phase which preceeds the PN phase.

The gas that makes up a PN has been processed via stellar evolution. This processing leads to the difference between the abundances in PNe and the differences in solar or HII region abundances. The abundances in the Sun and in HII regions are respectively believed to reflect the composition of the interstellar medium (ISM) at 5Gyrs and the current epoch, respectively. The material making up PNe has been processed by stellar evolution. This probably leads to enhancements in the abundances of He, C, and N.

1.1 The Importance of Stellar Evolution

The progenitors of PNe are zero-age main sequence (ZAMS) stars in the mass range 0.8-8.0$M_{\odot}$. The upper limit is uncertain and is set by the minimum mass star capable of igniting carbon-burning in the core. The lower limit is set by the minimum mass star which has had sufficient time to reach the PN stage. In fact at least two and possibly more PNe exist in globular clusters. It is popular to divide

this region into two mass ranges, the low (0.8-4$M_\odot$) and intermediate (> 4$M_\odot$) mass ranges.

The progenitors of PNe all appear to go through a number of distinct and important stages. All of them start on the ZAMS where they burn hydrogen in the core. When the hydrogen in the core is exhausted the core contracts but the outer layers expand, causing an increase in the luminosity and a decrease in the temperature. They continue to evolve "redward" on the HR diagram until hydrogen is reignited in a shell at which time the stars enter the first giant branch (FGB). By the time they reach the FGB they have expanded from $\sim R_\odot$ to $\sim 100R_\odot$. On the FGB, the luminosity of these stars increases until the helium in the core ignites. The onset of core helium burning causes the outer layers to contract. This results in an increase in the surface temperature which causes the stars to evolve "blueward" on the HR diagram. When helium is exhausted in the core, the star once again expands and moves redward on the HR diagram, and when a helium shell ignites it has entered the asymptotic giant branch (AGB). The AGB is divided into two distinct stages. When helium burns in a thick shell and produces the majority of the luminosity this is the early-AGB (E-AGB) stage. When the helium burning shell narrows and a hydrogen shell also ignites this is the thermally pulsing asymptotic giant branch (TP-AGB). The double shell burning mode of the TP-AGB is unstable and quasi-periodically the luminosity of the helium shell increases by several orders of magnitude in a few years, a process which extinguishes the hydrogen burning shell. The sudden increase in the He shell luminosity is known as a thermal pulse (TP) or as a helium shell flash. During the TP-AGB stage the mass-loss grows from $10^{-8}M_\odot$ yr^{-1} to $10^{-4}M_\odot$ yr^{-1}, a process which ejects the envelope and allows the PN phase to begin.

During the process of evolution from the main-sequence to the PN phase, a star can experience a number of possible events in which material from layers which have been processed by nuclear burning can be mixed into the surface layers,

thereby changing the composition. Three possible mixing events or "dredge-ups" have been identified (Iben and Truran 1978, Iben and Renzini 1983).

Iben (1964, 1967) showed when a star first enters the FGB, the convective envelope of the star can reach into layers where hydrogen burning has occurred. The term coined for this event is the "first dredge-up". This increases the abundances of ^{4}He, ^{13}C, and ^{14}N at the expense of ^{12}C and ^{16}O. The production of ^{13}C and ^{14}N via the first dredge-up is secondary since these elements are produced from the carbon that existed at the first dredge-up. Recent calculations by Boothroyd and Sackmann (1997) confirm that all stars in the intermediate and low-mass range encounter the first dredge-up.

The existence of the first dredge-up has been established via observations of red giant stars. Observations of the red giant stars confirm both qualitatively and quantitatively the existence and strength of the first dredge-up (see Sneden 1989 for a review of the evidence).

When the star enters the E-AGB, the convective envelope can penetrate the hydrogen exhausted core, mixing to the surface (Becker and Iben 1979). This process is known as the second dredge-up. Material rich in helium and nitrogen and totally depleted in hydrogen, carbon, and oxygen is mixed into the surface layers, increasing the abundances of ^{4}He and ^{14}N at the expense of ^{12}C, ^{13}C, and ^{16}O. Becker and Iben (1979) showed that the second dredge-up occurs only for progenitors with $M \gtrsim 4.5 M_\odot$. This limit is metallicity dependent with the lowest mass model encountering dredge-up decreasing with decreasing metallicity. Recent calculations by Boothroyd and Sackmann (1997) confirm the metallicity dependence and extend it down to very low metallicities.

After each helium shell flash on the thermally pulsing asymptotic giant branch, the convective envelope can mix helium and carbon rich material to the surface. During a thermal pulse, a convective helium burning shell develops (Schwarzschild and Härm 1967). The luminosity of this shell is very high ($\sim 10^7 L_\odot$), and a

significant amount (but not all) of the ^{4}He is burned into ^{12}C. At the end of the thermal pulse, the outer convective envelope can extend into the ashes of this shell (Iben 1975, 1976, 1977). This process is known as the third dredge-up. Note that it does not necessarily occur on every thermal pulse.

Third dredge-up has been used to explain the presence of carbon (C-)stars. Some very luminous stars which are most likely on the AGB have an abundance ratio (by number) C/O>1. This is different from other stars where C/O is generally in the solar ratio (C/O$\approx$ 1/3). Schwarzschild and Härm realized that the third dredge-up could explain the existence of C-stars.

One problem that developed was that the stellar evolution theory of the 1970's (Iben 1975, 1976, 1977) predicted minimum and maximum luminosities for carbon stars that do not agree with the observed values. The minimum luminosity carbon star is less luminous than predicted and so is the maximum luminosity carbon star. Since luminosity roughly correlates with the mass, the predicted mass range of carbon stars ranged from $3 - 8M_\odot$, whereas the observed mass range is $\sim$ 1.5– $\sim$4.0$M_\odot$. This is the so called "carbon-star" problem.

More recent calculations of the third dredge-up (Iben and Renzini 1982, Lattanzio 1986, Boothroyd and Sackmann 1988abcd) including improved physics (i.e. better opacities for carbon, semi-convection) and improved numerical procedures (Straniero et al. 1997), find the third dredge-up in the low-mass range ($1.5-3M_\odot$). These improved calculations bring the predictions of the low end of the luminosity range into agreement.

Scalo (1976) first examined another process which affects the surface abundances of intermediate mass stars. Between TP-AGB helium shell flashes, a gigantic convective zone exists between the surface of the star and the hydrogen exhausted core. For intermediate mass stars, the base of the convective envelope can get hot enough for the CNO bicycle to effectively operate. This process, called hot-bottom burning, effectively converts ^{12}C to ^{14}N via the CN cycle. It also can

convert some ^{16}O to ^{14}N via the ON cycle. Renzini and Voli (1981) showed that this process prevents high luminosity AGB stars from becoming C-stars, thereby reducing the upper mass limit for C-star formation.

The recent calculations of Blöcker and Schönberner (1991) and confirmed by Boothroyd and Sackmann (1992), Lattanzio (1992), and Forrestini and Charbonel (1997) indicate that the luminosity produced by hot-bottom burning is much larger than previously thought. These studies have found that up to 50% of the luminosity of the intermediate mass star between thermal pulses can be produced by this envelope burning. This effect has significant effects on the lifetime and nucleosynthesis of intermediate mass stars.

Planetary Nebulae provide an excellent observational test of the dredge-up theory as well as hot-bottom burning. They immediately follow the TP-AGB phase, so the PNe should retain the final surface abundances. The elements most affected by the three dredge-ups and hot-bottom burning are hydrogen, helium, carbon, nitrogen, and oxygen; all of which can be measured in PNe. Also, PNe span the entire range of mass where the three dredge-ups and hot-bottom burning occur allowing us to examine objects where the different processes have affected the surface abundances by different relative effects.

Qualitative studies of the abundances in planetary nebulae have confirmed the general picture outlined above. These studies show that they differ significantly from those in HII regions and the Sun. The difference in abundances reflects the processing by stellar evolution of the PN gas. Recent studies confirm that in some PNe the abundance ratio N/O is 2-4 times higher than that found in the Sun or in HII regions. The same studies indicate the PN helium abundance can be 10-40% higher than that found in HII regions or the Sun. The C/O abundance ratio is enhanced in some PNe (Rola and Stasinska 1993, Henry and Kwitter 1995, 1996, 1997). The C/O ratio can be greater than 1. The enhancements in the abundances of helium, carbon, and nitrogen are all expected in the picture of stellar evolution

outlined above.

Recent quantitative studies also confirm a general pattern. Using trends in TP-AGB models, Renzini and Voli (1981), Groenewegen and deJong (1993, 1994). and Marigo et al. (1996) created models to make synthetic TP-AGB populations. Each of these studies examined the evolution of stars with masses between 1 and 8 $M_{\odot}$ incorporating the three dredge-ups and hot-bottom burning to PNe models. All found that nitrogen is enhanced in intermediate mass stars via hot-bottom burning and that carbon is enhanced in low-mass stars via third dredge-up. These studies also provide *qualitative* agreement with the trends in the PN data.

1.2 The Importance of Population

The mass range of PNe progenitors means that PNe will represent a range of populations. PNe are known to be members of the bulge, disk, and halo. Using kinematics, studies have established the differences between older and younger disk PNe (Acker 1980, Maciel and Dutra 1992). Bulge and halo PNe are also distinguishable via their kinematics.

Abundance studies have established differences between different populations. PNe nearest the Galactic Plane typically have the highest average N/O and O/H. Both these quantities generally decrease with distance from the plane.

Several halo PNe have been discovered which give us a unique window into the advanced stages of very low-mass stellar evolution. There is a PN in globular cluster M15 (K648) for which we can reliably infer most of the stellar parameters, e.g., mass, age, luminosity. The wealth of information on K648 will strongly constrain the parameters used to model it. By using this PN we hope to establish a model(s) for the origin of halo PNe.

1.3 Thesis Goals

1. Establish the differences in chemistry between PNe of different stellar populations. in particular the differences between bulge and the disk.

2. Create a new and more detailed model for computing synthetic TP-AGB populations and the resulting PNe. This model incorporates an improved treatment of hot-bottom burning based on the latest calculations. This model will also incorporate many updated parameters and physics.

3. Explore the range of possible PNe parameter space. In particular. we will explore models of other than solar metallicity to improve agreement between model results and PN data.

4. By incorporating new results, we hope to improve the quantitative agreement between models and data.

5. Establish models for the TP-AGB evolution of halo PNe.

Chapter 2

Multivariate Data Analysis

Planetary nebulae (PNe) are a heterogeneous set of objects, believed to have zero-age main sequence (ZAMS) masses between 0.8 to 8.0 $M_{\odot}$ and pre-PN lifetimes of ~0.03-10 Gyrs, implying a variety of nucleosynthetic histories, membership in all but the youngest stellar populations, and a significant range of initial metallicities. Thus, a good, objective classification scheme which effectively separates the entire PN population into useful subsets according to empirical data is extremely useful when one desires to understand the relationship of these empirical properties to the underlying characteristics of PNe.

A number of classification schemes based on a variety of criteria are currently in use: the Peimbert scheme (Peimbert 1978, Faúndez-Abans and Maciel 1987) based on the He and N abundances and the kinematic properties of the nebula population; the classification system of Balick (1987) based on morphology; and the scheme of Amnuel, Guseinov, and Rustanov (1989) which relies on a number of characteristics related to the masses of the nebula and central star. These systems have recently been employed as bases of comparison while examining correlations between chemical abundance ratios (Amnuel 1993, Clegg 1991, Henry 1989, 1990, Perinotto 1991, Kingsburgh and Barlow 1994), radial abundance gradients (Amnuel 1993 , Maciel and Köppen 1994, Pasquali and Perinotto 1993), vertical abundance gradients (Faúndez-Abans and Maciel 1988), the kinematics of PNe (Dutra

and Maciel 1990, Corradi and Schwarz 1995) . correlations between abundance ratios and morphology (Corradi and Schwarz 1995), and correlations between central star parameters and morphology (Stanghellini, Corradi, and Schwarz 1993). In addition, all of these schemes derive from a parameter space whose properties have not been precisely determined.

Components of the bulge and disk are expected to be different, as the disk should contain a mix of old and young stars (0-10Gyrs old), whereas the bulge is expected to contain older stars (> 9Gyr old). Comparison of disk and bulge PNe has revealed that the average abundances of heavy elements in bulge PNe excluding He and N is $\sim$ 25% less than solar values (Ratag 1991). The same study also found a paucity of central star masses above $0.65M_{\odot}$. PNe with enriched nitrogen and helium have been found in the galactic bulge (Ratag 1991, Webster 1988). By comparing bulge and disk PNe with multivariate data analysis we hope to find a simple method of distinguishing the two.

The purpose of this study is to use multivariate analysis techniques to determine: 1) the effective dimensionality of PN parameter space and the specific parameters that represent each dimension; 2) the most appropriate classification system, given all of the data now extant; 3) the differences and similarities between bulge and disk PNe; and 4) a classification scheme for the bulge PNe. Multivariate data analysis (MVDA) allows a formal, objective, and detailed examination of an observational data set consisting of many objects, each of which is described by numerous parameters. In this chapter we specifically employ principal components analysis to probe the dimensionality of planetary nebula parameter space, while the taxonomy of planetary nebulae is explored using cluster analysis. The parameter space we investigate extends over numerous abundance ratios as well as kino-spatial properties of both disk and bulge PNe in the galaxy.

2.1 The Sample

Our sample of PNe comprise objects of the galactic disk and bulge compiled in Henry (1989b) and Henry (1990). The nine parameters considered in our study include six abundance ratios He/H, N/H, O/H, Ne/H, N/O, and Ne/O; and three kino-spatial parameters R, Z, and V_{LSR}, i.e. the galactocentric distance, the height above the galactic plane, and the radial velocity, respectively. The abundance information was taken from Henry (1989b) and Henry (1990). Values for R and Z for each PN, both in kpc, were calulated using the relations

$$R = [R_0^2 + d^2 cos^2(b) - 2R_0 d \cdot cos(b)cos(l)]^{1/2}, \tag{2.1}$$

$$Z = d \cdot sin(b) \tag{2.2}$$

where d is the distance from the sun from Cahn, Kaler, and Stanghellini (1991), l and b are galactic latitude and longitude, respectively, from Perek and Kohoutek (1967) or Blackwell and Burton (1981), and R_0 is the sun's galactocentric distance, which is assumed to be 8.5kpc. Values for V_{LSR} were taken from Schneider et al. (1983). Objects in Henry (1989b) and Henry (1990) for which data for any of the study parameters were unavailable were excluded from our analysis altogether. PNe NGC 2022, M2-6, M4-3, M2-10, H1-18, H2-18, M3-15, and NGC 6804 were excluded because of lack of complete data. Also, because of the large uncertainty in their galactocentric distances, the halo PNe were not included in our sample.

Objects within 20° of the galactic center and having $|V_{LSR}| \geq 25 kms^{-1}$ were designated bulge objects. The resulting list of 17 bulge objects are all contained in the lists compiled by Ratag (1991) and Webster (1988). Note, some bulge objects with low velocities maybe misclassified as disk objects, but this should not be a serious problem.

Our final list of 76 PNe is presented in table 2.1, where, for ease of analysis later on, objects are grouped according to the cluster analysis results. For each PN, column 1 provides the object's most common name, columns 2 and 3 list our

calculated values for R and Z in kpc, column 4 refers to cluster analysis results which will be discussed below, and the designation of a PN as either a bulge (B) or a disk (D) object is indicated in column 5.

2.2 Multivariate Data Analysis

Given a database comprising numerous parameters for a large sample of objects, principal components analysis (PCA) enables one to determine the minimum dimensionality of the parameter space required to adequately characterize the sample. On the other hand, cluster analysis (CA) objectively groups objects according to their location in parameter space. Here we present only short discussions of the principal components and cluster analysis techniques. For more detailed information the reader is referred to one of many texts on the subject, e.g., Kendall (1975), Murtagh and Heck (1987; MH87), and Rummel (1970). An excellent practical astronomical example of principal components analysis can be found in Whitmore (1984). Throughout our analysis we employed modified versions of the computer programs found at the end of chapters 2 and 3 of MH87.

2.2.1 Principal Components Analysis

Given a set of N objects with n observational parameters, each object can be represented in n-space by a set of coordinates $x_{ij'}$ ($1 \leq i \leq N$; $1 \leq j' \leq n$), where the orthogonal axes ($\mathbf{e}'_1, ..., \mathbf{e}'_n$) correspond to the n observational parameters. The goal of PCA is to find a set of m ($m \ll n$) parameters which are sufficient to describe the objects, i.e. the original coordinate system is rotated to a new coordinate system ($\mathbf{e}_1, ... \mathbf{e}_n$) such that a subspace of dimension m ($\mathbf{e}_1, ... \mathbf{e}_m$) is sufficient to describe the data set.

To proceed, the data are standardized to values $y_{ij'}$, where

$$y_{ij'} = \frac{x_{ij'} - \overline{x_{j'}}}{\sqrt{n}\sigma_{j'}}. \tag{2.3}$$

PN	R	Z	CL	Pop.	PN	R	Z	CL	Pop.
Hub4	6.4	0.11	1a	B	M1-80	11.4	0.22	2b	D
N6620	0.9	0.94	1a	B	N7354	9.0	0.05	2b	D
Hub6	6.8	0.05	1a	B	Hu1-1	13.1	0.79	2b	D
N6439	4.6	0.42	1a	B	I1747	10.6	0.07	2b	D
N6778	6.2	0.36	1a	B	I2003	11.7	3.32	2b	D
N6781	7.5	0.08	1a	D	N2346	9.7	0.09	2b	D
N6803	6.8	0.22	1a	D	N2452C	10.1	0.05	2b	D
Me1-1	6.8	0.24	1a	D	N2452S	10.1	0.05	2b	D
M1-75	8.0	0.00	1a	D	I4634	5.8	0.59	3a	D
N6894	8.1	0.08	1a	D	N6629	6.6	0.17	3a	D
N7026	8.7	0.01	1a	D	N6210	7.4	1.22	3a	D
N650	9.0	0.13	1a	D	N6826	8.5	0.35	3a	D
N2371W	9.9	0.51	1a	D	I5117	8.6	0.12	3a	D
N2371E	9.9	0.51	1a	D	N7662	8.9	0.36	3a	D
N2452N	10.1	0.05	1a	D	M1-1	14.6	2.28	3a	D
Hub5	7.3	0.02	1a	B	M1-4	11.1	0.12	3a	D
M1-42	3.1	0.45	1b	B	M2-2	12.4	0.32	3a	D
M1-35	4.5	0.16	1b	B	I351	13.6	1.44	3a	D
Me2-2	10.6	0.76	1b	D	J320	14.3	1.86	3a	D
I4776	4.7	0.91	2a	D	J900	11.2	0.13	3a	D
I4673	5.3	0.14	2a	D	N1535	10.1	1.50	3a	D
N6309	6.1	0.64	2a	D	I2165	10.1	0.43	3a	D
N6578	6.3	0.07	2a	D	N3242	8.7	0.58	3a	D
N6818	6.9	0.58	2a	D	Ha2-1	4.9	0.28	3a	D
N6751	6.4	0.27	2a	D	I4593	6.4	2.09	3c	D
N6807	5.9	0.61	2a	D	H1-23	3.8	0.15	3c	D
M1-74	6.8	0.29	2a	D	N6833	9.2	0.95	3b	D
N6891	7.1	0.67	2a	D	K3-67	11.8	0.38	3b	D
N6879	7.6	1.15	2a	D	K3-68	14.4	0.26	3b	D
N6905	7.8	0.28	2a	D	M2-21	2.4	0.27	4a	B
N6881	8.2	0.09	2a	D	M2-33	1.8	0.74	4a	B
N6884	8.5	0.26	2a	D	M2-23	4.6	0.19	4a	B
I418	9.0	0.25	2a	D	M3-20	3.8	0.18	4a	B
N6369	7.8	0.07	2b	B	M2-30	0.5	0.61	4a	B
N6790	7.4	0.17	2b	D	I4732	3.7	0.58	4a	B
Hu1-2	8.5	0.23	2b	D	N6567	6.2	0.03	4a	B
N6543	8.6	0.50	2b	D	I4846	5.4	0.64	4a	D
I5217	10.4	0.43	2b	D	CN2-1	4.6	0.30	4b	B

Table 2.1: Objects used in Multivariate Data Analysis

In this expression $\overline{x_{j'}}$ is the average value for parameter j', while $\sigma_{j'}$ is the standard deviation of parameter j' for all N points. As a result, $\sum_{i=1}^{N} y_{i,j'} = 0$, $\sigma_{j'} = 1$, and each $y_{i,j'}$ is unitless. The next step is to rotate the n-dimensional coordinate system so that the $y_{i,j'}$'s are transformed into $y_{i,j}$'s with axes $\mathbf{e}_1, ..., \mathbf{e}_n$. The direction of each axis in the new coordinate system is determined sequentially, i.e. $\mathbf{e}_1$ is determined first, followed by $\mathbf{e}_2$, etc. The variance, λ_j, is maximized for each axis, where the variance of the jth axis is defined as

$$\lambda_j = \sum_{i=1}^{N} y_{ij}^2; \tag{2.4}$$

and the jth axis must be perpendicular to all the axes determined before it, i.e. the third axis ($\mathbf{e}_3$) must be perpendicular to the first ($\mathbf{e}_1$) and second ($\mathbf{e}_2$) axes. This puts a constraint on λ_j such that

$$\lambda_1 \geq \lambda_2 \geq \lambda_3 \geq ... \geq \lambda_n. \tag{2.5}$$

The above procedure of maximizing the λ_j is equivalent to finding the eigenvalues (λ_j's) and the eigenvectors ($\mathbf{e}_k$'s) of the $n \times n$ correlation matrix.

The next step in the analysis is to determine the dimensionality m ($m < n$) of the subspace which can best describe the data. This stage of the analysis is more subjective than the previous ones, as there is no standard way to do it. For instance, it is possible to use the three criteria set forward by Gutman (1954), one of which states that any principal component with an eigenvalue greater than one is significant. However, this criterion can only be considered as a rule of thumb. In this work, the dimensionality is determined by matching the residual to the average observational error. There are two types of residuals, individual and average. Using the n dimensional rotated coordinate system, it is possible to reconstruct for each object the values of the observational parameters. For an m dimensional subspace, it is also possible to reconstruct a value for each observational parameter for each object. However there will be some difference between this reconstructed value

and the actual value of the observation for the individual object. The difference between the reconstructed value for each parameter and the actual value is the residual for the individual object. The average residual is the average of all the individual residuals for a particular observational parameter. We compute the average residual, $r_{j'}$ using the formula in table 4 of Brosche (1973). The average residual $r_{j'}$ is a measure of how well, on average, we can reconstruct the value of the *j'th* observational parameter using the m dimensional subspace.

2.2.2 Cluster Analysis

The goal of cluster analysis is to group objectively a set of objects according to distances of separation in n-dimensional space. Cluster analysis is an iterative procedure which starts with a set of N data points, each described by n parameters, and identifies the pair of points with the smallest dissimilarity, subsequently agglomerating this pair into a single composite point. The new composite point and the other points now form a new set of N-1 data points and the least dissimilar pair of points is identified and agglomerated. This procedure is repeated until the set has been agglomerated into a single point. Then, for the results of our cluster analysis to be useful one looks at the agglomeration process in reverse, starting with the single composite point, to find a functional set of points or groups.

Dissimilarity is a mathematical measure of the differences between each pair of points in n dimensional space. There are several types of dissimilarity, Euclidean distance being the most familiar type. Out of several possible methods for performing cluster analysis, we have chosen Ward's method (1963), which is distinguished by the type of dissimilarity employed as well as the method for determining new composite points. In this method the cluster center g is the composite point consisting of l individual points, where g represents the center of gravity of the l points. Thus, if x_{ij} is the jth component of the ith point, then the jth

component of the cluster center is

$$g_j = \frac{1}{l}\sum_{i=1}^{l} x_{ij}, \tag{2.6}$$

where the sum is over all points comprising the composite. The average variance of each cluster is then defined as

$$Variance = \frac{1}{l}\sum_{j=1}^{n}(\sum_{i=1}^{l}(x_{ij}^2 - g_j^2)) \tag{2.7}$$

where m is the dimension of the parameter space. In Ward's method the dissimilarity between a pair of points is defined as the increase in the average variance of the potential cluster which is introduced by adding the new point.

2.3 Results and Discussion

2.3.1 Results of Principal Components Analysis

To examine the effect of population differences on our PCA results, our analysis was performed separately on bulge (B) and disk (D) subsamples as well as the combined (C) sample[1] All runs were made with the following parameters: log(He/H)+12, log(N/H)+12, log(O/H)+12, log(Ne/H)+12, log(N/O), log(Ne/O), and V_{LSR} designated from now on as He, N, O, Ne, N/O, Ne/O, and V_{LSR} respectively. The parameters R and Z were included in the D and C runs but omitted from the B run.

The main PCA results are reported in Table 2.2. Letters in column 1 indicate the set of objects, while the parameters are listed in column 2. Values for residuals for dimensionalities 1-5 are given in columns 3-7. Estimated observational uncertainties and the eigenvalues appear in columns 8 and 9, respectively.

To illustrate the use of Table 2.2, consider the case of the bulge (B) objects. First, the feasibility of using a one-dimensional parameter space (m=1) for representing these objects is tested. Note, except for Ne/O, none of the residuals is less

[1]We note that when placed in the He-N/O plane the disk objects I4593 and H1-23 appear anomalous relative to the remainder of disk PNe. Therefore, we have ignored these two objects in our analysis.

Set	Var	Residuals[a]					OU[b]	EV[c]
		m=1	m=2	m=3	m=4	m=5		
B	He	16%	11%	10%			10%	$\lambda_1 = 3.12$
	N[d]	0.26	0.16	0.16			0.15	$\lambda_2 = 2.22$
	O[d]	0.18	0.10	0.07			0.15	$\lambda_3 = 0.77$
	Ne[d]	0.20	0.06	0.00			0.10	$\lambda_4 = 0.61$
	N/O[d]	0.38	0.13	0.12			0.20	$\lambda_5 = 0.27$
	Ne/O[d]	0.08	0.07	0.07			0.20	
	V_{LSR}[e]	62.9	51.0	9.3			10.0	
D	He	11%	10%	9%	9%	9%	10%	$\lambda_1 = 3.23$
	N[d]	0.19	0.17	0.12	0.11	0.10	0.15	$\lambda_2 = 1.87$
	O[d]	0.21	0.09	0.06	0.03	0.00	0.15	$\lambda_3 = 1.28$
	Ne[d]	0.18	0.09	0.09	0.05	0.04	0.10	$\lambda_4 = 1.04$
	N/O[d]	0.30	0.11	0.10	0.10	0.10	0.21	$\lambda_5 = 0.69$
	Ne/O[d]	0.10	0.10	0.07	0.07	0.04	0.20	$\lambda_6 = 0.53$
	V_{LSR}[e]	33.5	32.3	16.3	16.2	9.6	10.0	$\lambda_7 = 0.36$
	R[f]	2.2	2.0	2.0	1.3	0.8		
	Z[f]	0.52	0.52	0.52	0.31	0.22		
C	He	12%	10%	10%	10%	10%	10%	$\lambda_1 = 3.24$
	N[d]	0.20	0.18	0.18	0.18	0.09	0.20	$\lambda_2 = 1.79$
	O[d]	0.21	0.06	0.06	0.06	0.02	0.20	$\lambda_3 = 1.21$
	Ne[d]	0.20	0.06	0.03	0.02	0.02	0.10	$\lambda_4 = 0.93$
	N/O[d]	0.31	0.14	0.13	0.13	0.09	0.31	$\lambda_5 = 0.89$
	Ne/O[d]	0.10	0.10	0.09	0.08	0.04	0.21	$\lambda_6 = 0.58$
	V_{LSR}[e]	46.1	46.1	31.7	18.0	16.3	10.0	$\lambda_7 = 0.45$
	R[f]	2.8	2.8	2.0	2.0	1.3		
	Z[f]	0.49	0.49	0.46	0.21	0.21		

Table 2.2: Residuals and Eigenvalues

a. m is the number of dimensions being considered.
b. Observational Uncertainty
c. Eigenvalue for each dimension
d. Residuals and observational uncertainty in dex
e. Residuals and observational uncertainty in km/s
f. Residuals and observational uncertainty in kpc

than its associated observational uncertainty. Therefore, the bulge PNe cannot be represented satisfactorily by a one dimensional parameter space. On the other hand. for two-dimensional space (m=2), all of the residuals with the exception of the one associated with V_{LSR}, are less than or approximately equal to their uncertainties. Thus, the two dimensional space satisfactorily describes the base set of chemical parameters: He, N, O, Ne, N/O, and Ne/O. For the three dimensional space (m=3), all residuals are now less than or equal to their associated uncertainties. and thus three dimensional parameter space also adequately represents the set of bulge PNe.

Using the same method of comparing residuals to observational uncertainties. the D and C sets are shown to require five dimensions, with the base set of chemical parameters being described by the first two dimensions and V_{LSR}, R. and Z by the last three.

A correlation vector (CV) diagram is a graphical method for representing the relationship between the parameters. The CV diagram is created by projecting unit vectors lying along the individual parameter axes. i.e. He, N. O. etc.. into the space defined by the eigenvectors determined by the PCA. Figure 2.1a is the CV diagram for the B set. Our CV diagrams are shown in two dimensions only. since higher dimensional diagrams become visually confusing. The cosine of the angle between any two vectors is approximately equal to the correlation coefficient[2] of the corresponding quantities. For example, the correlation between N and N/O is 0.90, implying an angle of 26°. which is very close to the actual angle of 29° between the vectors.

For greater clarity, it is useful to rotate the coordinate system orthogonally so that the eigenvectors $\mathbf{e}_1$, $\mathbf{e}_2$, and $\mathbf{e}_3$ are aligned as closely as possible with the parameters. Such a rotation does not change the relationship between the vectors

[2]Correlation coefficients were computed as part of the PCA analysis but are not tabulated here.

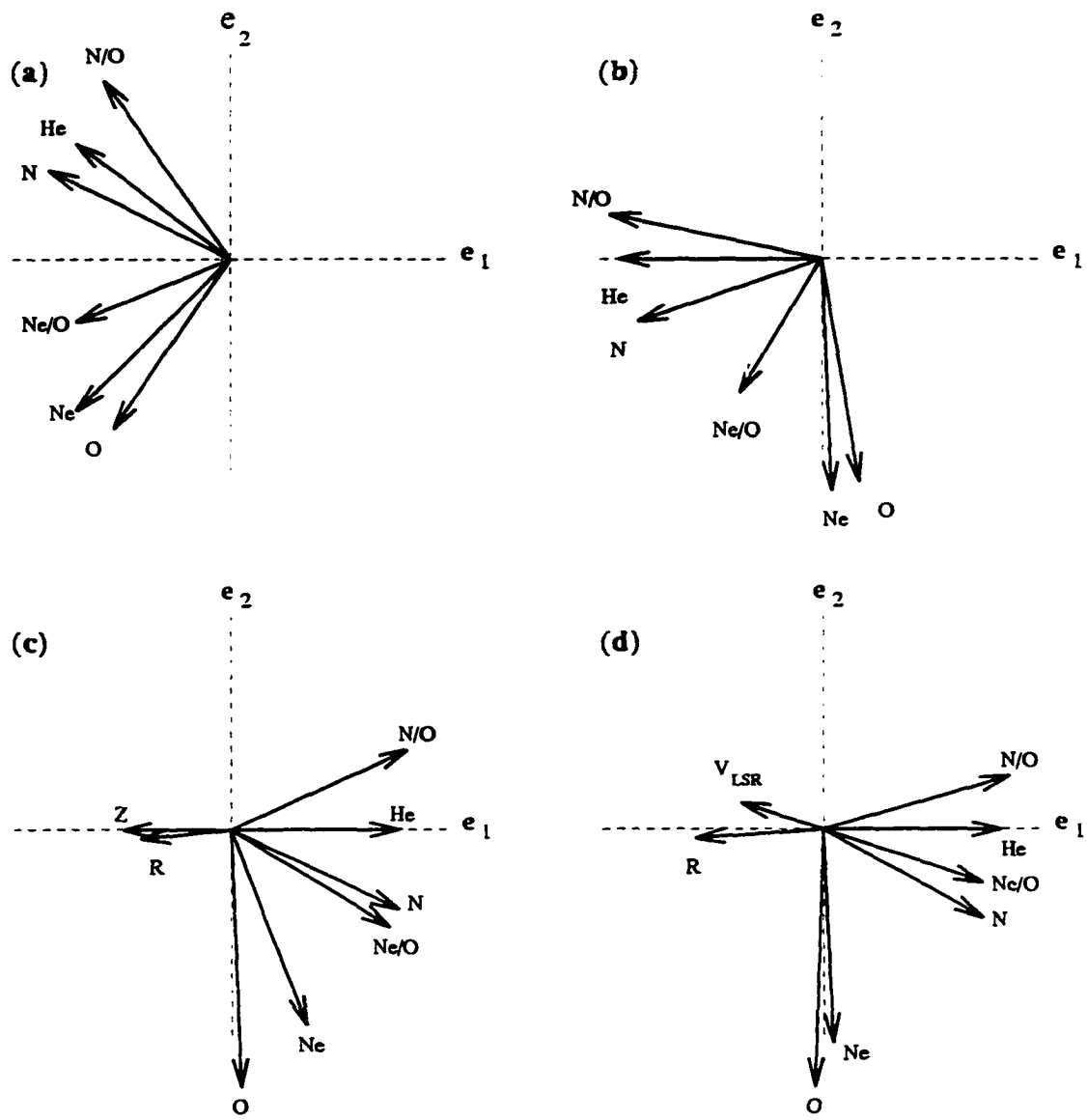

Figure 2.1: The correlation vector diagrams generated by our PCA runs. The diagrams are labeled as follows: (a) The unrotated diagram for the bulge PNe subset. (b) the rotated diagram for the bulge PNe, (c) the rotated diagram for the disk PNe subset, and (d) the rotated diagram for our bulge and disk PNe set. In each diagram the distance from the origin to the end of the dotted line is 0.6. It should be noted that it was impossible to get the angles between the vectors exactly correct due to limitations of our plotting package.

Var	e_1	e_2	e_3
He	-0.5626	0.0000	0.0045
N	-0.5032	-0.1720	0.1592
O	0.1289	-0.6315	0.0000
Ne	-0.0286	-0.6399	-0.0433
N/O	-0.5837	0.1125	0.1663
V_{LSR}	-0.1616	0.0642	-0.9656
Ne/O	-0.2158	-0.3812	-0.1128

Each vector, i.e. He, is a unit vector in the 7 dimensional space, its direction lies in the direction of the original axis. The numbers in columns 2-4 are the components of each parameter in the new space. The vectors shown are the projections of the original axes (i.e. He, N, etc.) into the first two new axes.

Table 2.3: Components of Vectors in the Rotated Bulge Parameter Space

Var	e_1	e_2	e_3	e_4	e_5
R	-0.2512	-0.0085	0.6871	-0.4782	-0.0848
Z	-0.2975	-0.0009	0.1974	-0.2099	0.7484
V_{LSR}	0.0549	-0.0050	0.3511	0.7409	0.3494
He	0.4489	0.0000	0.0503	-0.3045	-0.0612
N	0.4414	-0.2184	0.3535	0.0520	-0.0552
O	0.0123	-0.7231	0.0000	0.0000	0.0000
Ne	0.2118	-0.5543	-0.1284	-0.1195	0.2314
N/O	0.4687	0.2276	0.3816	0.0550	-0.0604
Ne/O	0.4294	0.2651	-0.2755	-0.2561	0.4966

Table 2.4: Components of Vectors in the Rotated Disk Parameter Space
Same as table 2.3 except that the first 5 components of each vector are presented.

Var	e_1	e_2	e_3	e_4	e_5
R	-0.2583	-0.0287	-0.5896	-0.4868	-0.1639
Z	-0.2194	-0.0858	0.1075	-0.3222	-0.7632
V_{LSR}	0.1252	-0.0599	0.0377	0.6364	-0.5926
He	0.4833	0.0000	-0.0420	-0.1681	0.0362
N	0.4290	-0.2579	-0.3757	0.0099	-0.1030
O	-0.0874	-0.7293	0.0000	0.0000	0.0000
Ne	0.1092	-0.5917	0.2365	-0.1934	0.0510
N/O	0.5049	0.1403	-0.3987	0.0944	-0.1090
Ne/O	0.4211	0.1416	0.5306	-0.4340	-0.1145

Table 2.5: Components of Vectors in the Rotated Bulge and Disk Parameter Space Same as table 2.3 except that the first 5 components of each vector are presented.

but allows easier inspection of the relationships between them. For each set, the original orientation of the parameter vectors has been rotated so that the He and O vectors now have no e_2 and e_3 components, respectively. The resulting CV diagrams for B, D, and C are respectively shown in figures 1b,c,d, while the vector components are given in Tables 2.3, 2.4, 2.5. If we consider only the first two eigenvectors in each set, i.e. e_1 and e_2, the He, N, O, Ne, and N/O vectors show a clear pattern: the vectors He, N, and N/O are all roughly correlated with each other, while the same is true of the vectors O and Ne. At the same time, these two vector sets are uncorrelated with each other. This pattern is evident from the general orthogonal orientation of these two vector groups in the CV diagrams as well as the component values in Tables 2.3, 2.4, 2.5. Finally, the same diagrams and tables indicate clearly that the kino-spatial parameters V_{LSR}, R, and Z are orthogonal to each other as well as to the chemical parameters.

Studies of PNe, both observational (Henry 1990, Clegg 1990, Kingsburgh and Barlow 1994, Perinotto 1991) and theoretical (Iben and Renzini 1983, Renzini and Voli 1981), suggest He, N, and N/O are related to the nucleosynthesis which occurs in the progenitor star and O and Ne are related to the progenitor metallicity. Thus, considering the parameters associated with each eigenvector in the CV diagrams,

$\mathbf{e_1}$ is related to nucleosynthesis during progenitor star evolution, while $\mathbf{e_2}$ is related to progenitor metallicity. At the same time, the spatio-kinematic quantities do not correlate with one another nor with the abundance parameters, although it is important to remember that since our study is confined to linear correlations, possible higher order relationships between the kinematic and chemical quantities may be masked. Of particular interest is the absence of projection of these three vectors along the $\mathbf{e_2}$ eigenvector, i.e. the one closely associated with progenitor metallicity, as seen in Tables 2.3.2.4.2.5. Our results would seem to indicate that for the bulge and disk, kino-spatial properties and progenitor metallicity are uncorrelated.

2.3.2 Results of Cluster Analysis

It is possible to classify the PNe according to their location in the subspace derived by PCA. To locate the natural groups in this subspace we perform cluster analysis on the sample using the seven variables: R, V_{LSR}, He, N, O, Ne, and N/O. The five abundance parameters were chosen because they correlate with the first two principal components. R and V_{LSR} have been included to account for the kinematic differences between the bulge and disk objects. The height above the galactic plane (Z) has been excluded, since it is meaningless for bulge objects. Finally, the ratio Ne/O has been excluded since it is unclear if differences in this parameter among PNe are real or simply due to observational scatter.

The inclusion of R as a parameter may seem questionable since the determination of R depends on the distance derived to the PNe. The distances to galactic PNe are poorly known (see Terzian 1993 for a recent review). However, R turns out to be an important classification parameter only between objects with large differences in galactocentric radii, i.e. between the bulge and disk objects. Therefore, it is probable the uncertainties in R will not have a large impact on the results.

Starting at the top and moving downward, the dendridic diagram in figure 2.2 shows the reverse of the agglomeration process, i.e., it shows how CA divided

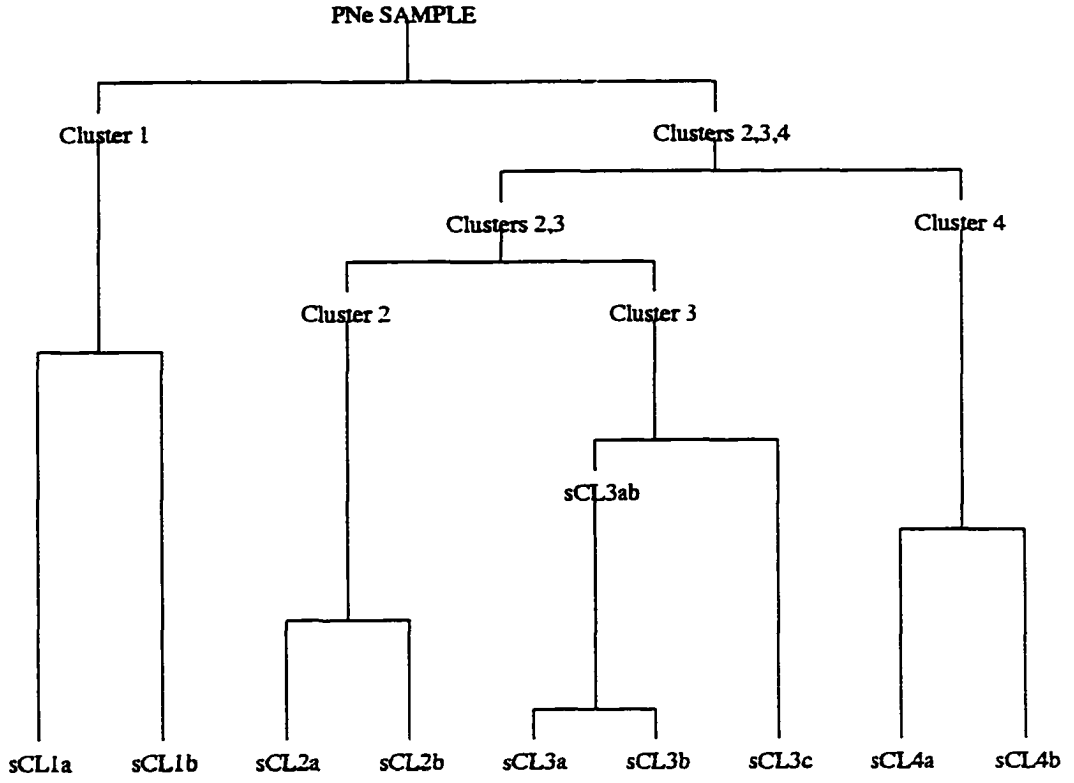

Figure 2.2: The dendridic diagram generated by our cluster analysis using the parameters R, V_{LSR}, He, N, O, Ne, and N/O. The branches where each of the clusters and subclusters are located are labeled.

Cluster	Type I	Type IIa	Type IIb	Total	$V_{LSR} > 60$	Disk	Bulge
1a	11	5	0	16	3	10	6
1b	3	0	0	3	3	1	2
2a	1	6	7	14	0	14	0
2b	3	8	2	13	3	12	1
3a	0	0	16	16	0	16	0
3b	2	0	1	3	1	1	2
3c	2	0	0	2	2	1	1
4a	0	0	8	8	8	1	7
4b	0	1	0	1	1	0	1

Table 2.6: Shows the breakdown of each subcluster into Peimbert types, bulge and disk members, and into objects with $V_{LSR} > 60$ km/s. Only composition criteria are used in the Peimbert scheme classification.
a The total number of PNe in each subcluster
b Number of PNe with $V_{LSR} > 60$km/s

the PNe sample into subsets. We decided to first analyze the first four subgroups which we label as clusters 1, 2, 3, and 4. Each of these groups contains a reasonable number (≥ 9) objects which are hopefully fairly homogeneous. The four clusters were divided further into 9 subclusters, labeled on figure 2.2 as sCL. The relative vertical distances of connection points from the bottom indicate the order in which the points were combined, e.g., the first two points to be joined were 3a and 3b (these two groups of PNe are the most similar), followed by the joining of 2a and 2b, and so on. The cluster and subcluster membership of each PN is listed in column 4 of table 2.1.

The parameter averages for each cluster and subcluster are presented in table 2.7. The average of the chemical parameters and the radial velocity V_{LSR} decrease along the sequence of clusters: 1, 2, and 3, whereas the parameters R and Z increase along the same sequence. Cluster 4 appears distinct from the others as it has the smallest average R and the largest average V_{LSR}. However, the average chemical abundances of cluster 4 resemble those of clusters 2 and 3.

CL	R[a]	Z[a]	V_{LSR}[b]	He/H[c]	N/H[c]	O/H[c]	Ne/H[c]	N/O[d]	Ne/O[d]
Solar[e]	—	—	—	10.99	8.05	8.93	8.09	-0.88	-0.84
Clusters									
1 all	7.11	0.27	47.69	11.12	8.67	8.80	8.14	0.02	-0.66
2 all	8.34	0.45	35.79	11.03	8.10	8.77	7.96	-0.58	-0.77
3 all	9.36	0.74	31.43	11.00	7.64	8.51	7.71	-0.73	-0.79
4 all	3.66	0.39	156.6	11.00	8.07	8.73	7.97	-0.71	-0.79
Subclusters									
1a	7.3	0.23	36.8	11.11	8.64	8.85	8.19	-0.18	-0.65
1b	6.1	0.46	105.8	11.19	8.81	8.33	7.59	0.48	-0.74
2a	6.9	0.44	24.6	11.03	8.01	8.86	8.03	-0.78	-0.76
2b	9.9	0.46	47.9	11.03	8.19	8.64	7.86	-0.43	-0.78
3a	9.8	0.73	20.6	10.98	7.62	8.55	7.76	-0.91	-0.79
3b	11.8	0.53	76.8	10.95	7.90	8.07	7.34	-0.21	-0.76
3c	5.1	1.12	50.4	11.16	7.02	8.58	7.71	-1.47	-0.87
4a	3.5	0.41	143.4	10.99	7.80	8.58	7.78	-0.74	-0.80
4b	4.6	0.30	262.2	11.04	8.74	9.24	8.56	-0.50	-0.68

Table 2.7: Shown in this table are the parameter averages for each PNe Cluster.
a. in units of kpc
b. in units kms^{-1}
c. in form log(X/H)+12
d. in form log(X/O)
e. Solar abundances calculated from Anders and Grevasse (1989)

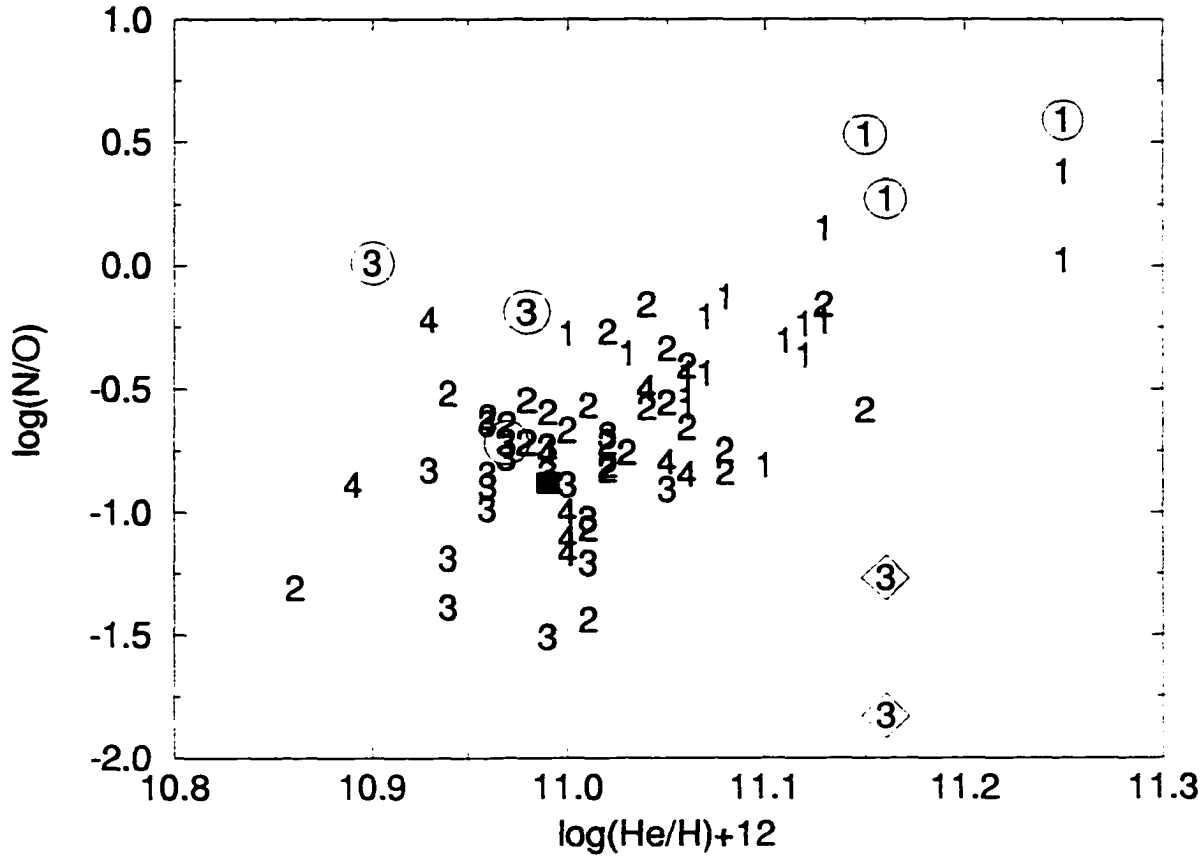

Figure 2.3: Cluster comparison diagram for log(He/H)+12 versus log(N/O). Cluster membership of each PN is indicated by a number. Members of subcluster 1b are indicated by circled 1's, members of 3b by circled 3's and members of 3c by a 3 enclosed by a diamond. The solar values are indicated by the solid square.

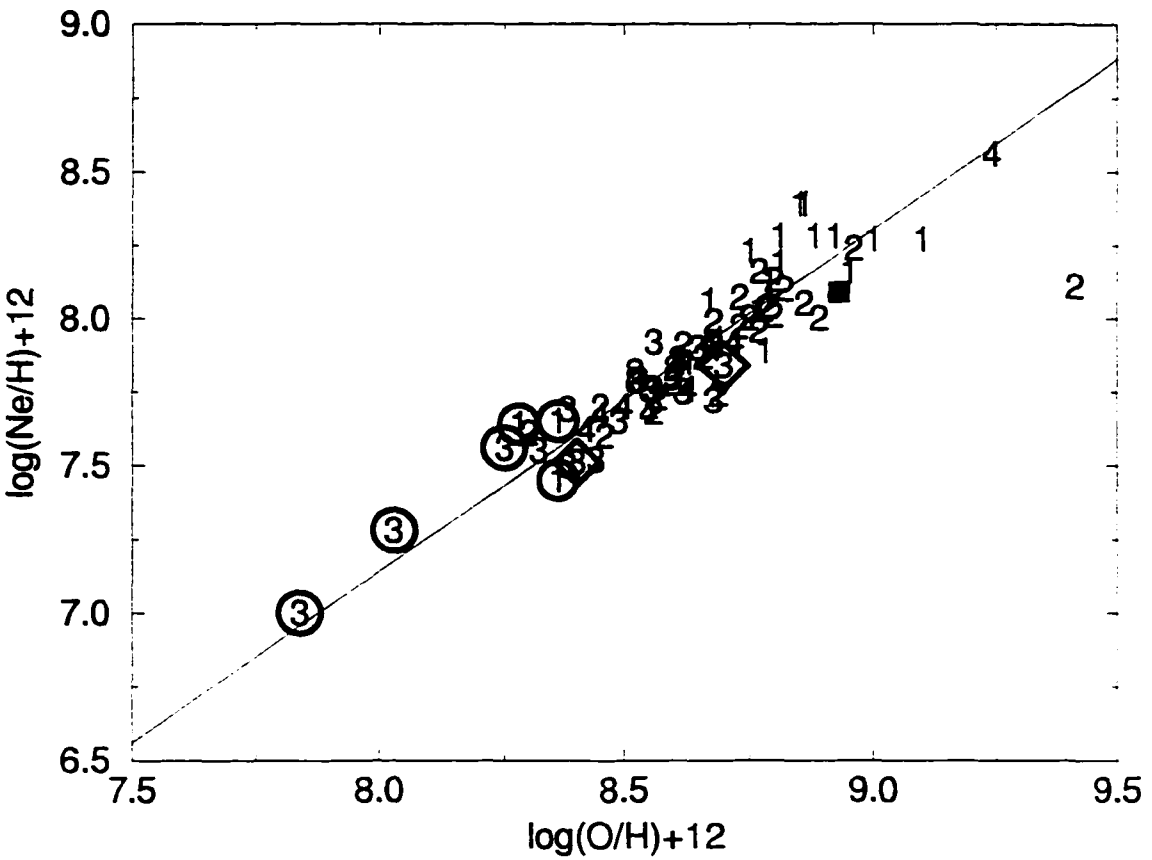

Figure 2.4: Cluster comparison diagram for log(Ne/H)+12 versus log(O/H)+12. The symbols have the same meaning as in figure 2.3.

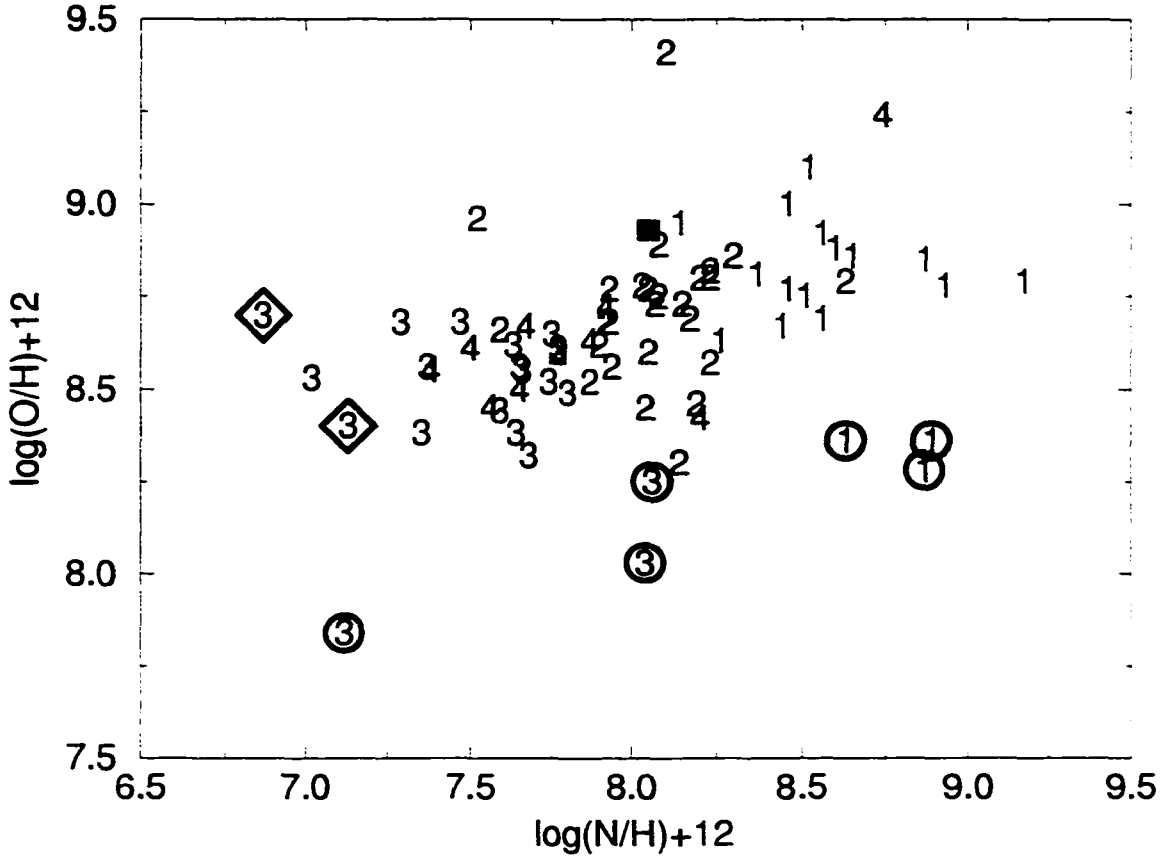

Figure 2.5: Cluster comparison diagram for log(O/H)+12 versus log(N/H)+12. The symbols have the same meaning as in figure 2.3.

Figures 2.3, 2.4, and 2.5 are used to explore the ranges of the chemical parameters for each cluster and subcluster. Figures 2.3 and 2.5 show a clear separation of clusters 1, 2, and 3 on the He-N/O plane and in the abundance of N, i.e. it is possible to draw lines on these figures which separate the clusters[3]. The ratios He/H, N/H, and N/O increase along the sequence cluster 3, 2, and 1. There is no clear line of separation between clusters 1, 2, and 3 that can be seen on figures 2.4 and 2.5, although the average O/H and Ne/H also increases along the sequence cluster 3, 2, 1. At the same time, cluster 4, while overlapping clusters 2 and 3 in abundance patterns, is significantly separated from these clusters in parameter space because of systematic differences in velocity and galactocentric distances.

The bulge PNe in the sample are almost exclusively confined to clusters 1 and 4. Cluster 1 contains a mix of bulge and disk PNe with similar abundances and it is very striking how similar the bulge and disk PNe appear to be in abundance space. To test how well the bulge and disk PNe could be separated by using only abundances as classification parameters a trial cluster analysis was carried out using only the abundance parameters resulting in the bulge and disk PNe being completely mixed together in 3 clusters that roughly correspond to clusters 1, 2, and 3. *The conclusion is that it is impossible to distinguish between individual bulge and disk PNe based on abundances alone.*

We now turn our attention to the subclusters arising in figures 2.3, 2.4, and 2.5. The importance of the subclusters is that each may contain objects which require explanation or may contain objects with significant errors in the parameter determination. In clusters 1, 3, and 4, the subcluster containing the most objects is designated "a". The "a" subclusters of clusters 1, 3, and 4 each contains 75% or more of the total number of cluster objects, whereas subclusters other than "a" each contain less than four objects. The subclusters of clusters 1 and 3 have been

[3]The most straightforward way to put other objects into these categories by using the nitrogen abundances. Cluster 1 objects generally have $logN/H + 12 \geq 8.3$, cluster 2 objects have $8.3 \leq logN/H + 12 \geq 7.8$, and cluster 3 objects have $logN/H \leq 7.8$.

distinguished in figures 3a-c, the three 1b members are indicated by circled ones, the three 3b members by circled threes and the two 3c members by threes enclosed by a diamond.

In figs. 2.3 and 2.4, the 1b objects have He/H and N/O values that are generally higher than the 1a objects, but the 1b objects have O/H and Ne/H that are $0.4dex$ less than the closest 1a object. This difference is larger than the average observational uncertainties, however this does not rule out the possibility of observational error. If this gap is real then the 1a and 1b PNe respectively represent oxygen-rich and oxygen-poor cluster 1 objects.

Subcluster 4b contains a single bulge PN, CN2-1, which is high in O/H and Ne/H, while subcluster 4a contains bulge planetaries with much lower abundances.

The subclusters of cluster 3 are widely separated in parameter space. The PNe in cluster 3c are I4593 and H1-23 which appear anomalous as discussed in the PCA section. The PNe of cluster 3a have $V_{LSR} < 40kms^{-1}$ and $log(O/H) + 12 > 8.55$ and those of cluster 3b have $V_{LSR} > 50kms^{-1}$ and $log(O/H) + 12 < 8.55$. The low abundances and large velocities of the 3b objects suggests that these objects are thick disk objects and the abundances and velocities of the 3a objects suggest a thin disk origin.

2.4 Discussion

The results of our cluster analysis confirm the expected, the primary classification criterion for PNe is the nitrogen and helium content. Spatio-kinematic criteria determine the population of each PN. There also appears to be some use in looking at the oxygen and neon content of each nebula, since the 1b PNe appear to be a class of oxygen poor nebulae with high nitrogen and helium content.

What accounts for the differences among the clusters produced in the analysis? The models of Becker and Iben (1980) and Renzini and Voli (1981) suggest that as the mass of the progenitor increases, the helium and nitrogen abundances in

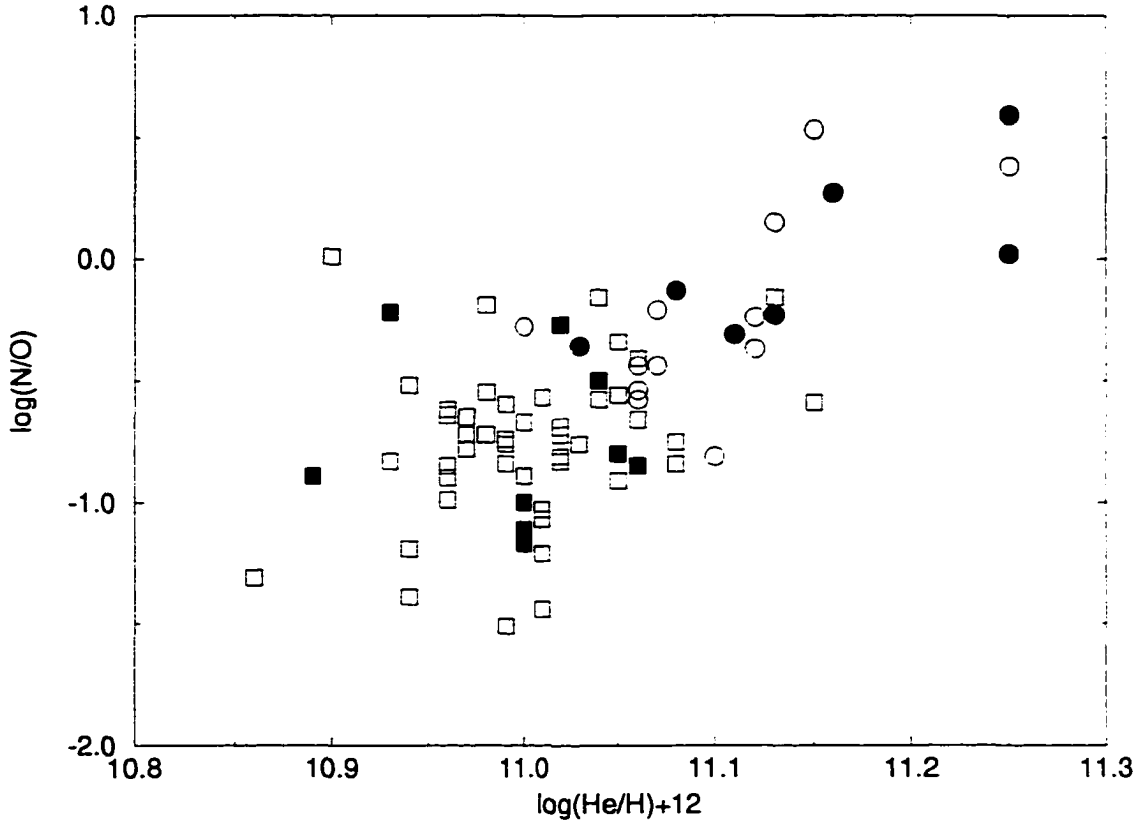

Figure 2.6: log(He/H)+12 versus log(N/O) for bulge and disk PNe. The filled symbols represent the bulge objects and the open symbols the disk objects. The circles represent the cluster 1 objects and the squares the non-cluster 1 objects. The two PNe of cluster 3c have been removed.

the resulting PN increase. Studies comparing N/O to core mass indicate that a correlation exists between these quantities (Kaler and Jacoby 1989, Kaler and Jacoby 1990, Stasińska and Tylenda 1990) for disk PNe. If we make the reasonable assumption that as core mass increases the progenitor mass increases, which is supported by the initial-final mass relation of Weidemann and Koester (1983) then we infer that since nitrogen increases along the sequence from cluster 3 to cluster 1, the progenitor mass also increases.

This picture works for the disk objects. However, eight of nineteen PNe in

cluster 1 are classified as bulge objects. Does this trend hold for them as well? In Fig. 2.6 we have plotted log(N/O) versus log(He/H)+12, where the bulge objects are represented by filled symbols and the disk objects by open symbols. Cluster 1 objects have been distinguished by circles, and members of other clusters by squares. It can be seen that the bulge and disk objects are completely mixed, *suggesting that there is no difference between disk and bulge PNe in terms of their nucleosynthesis.*

The apparent similarity in He/H and N/O (nucleosynthesis) patterns of bulge and disk PNe implies that their progenitors represent the same mass range. However, studies of bulge stars by Terndrup (1988) and van der Veen and Habing (1990) suggest that the upper mass limit for bulge stars is $\approx 2M_{\odot}$, whereas according to theory (Renzini and Voli 1981), to account for the ratios of He/H and N/O seen in our sample, main sequence progenitors of $5 - 8M_{\odot}$ are needed, which is in disagreement with the $2M_{\odot}$ upper mass limit for bulge stars. We suggest the following possibilities to account for this discrepancy:

1. An unidentified population of intermediate mass stars exists in the bulge. This has also been suggested by Webster (1988) on the basis of her study of bulge PNe. The number of Mira variables with $M_{bol} < -5.0$ has been estimated at 100 (Whitelock 1992). These luminous Miras are believed to be the progeny of main sequence stars with $M > 3M_{\odot}$, suggesting that the number of progenitors in the right mass range is small. It has been suggested that these luminous variables are the progeny of binary mergers in the bulge (Renzini 1994).

2. The progenitors of the cluster 1 bulge PNe are low mass stars that formed with He/H and N/O similar to that found in disk PNe. This scenario appears to be a better explanation for the lack of a correlation between N/O and core mass.

3. The progenitors of the cluster 1 bulge PNe are binary stars, where the companion is now an unseen white dwarf, but in the past was an AGB star with an envelope enriched in He and N which was transferred to the PN progenitor. Recently McWilliam and Rich 1994 found a Li rich star in a small sample (12 stars) of galactic bulge K giants, which suggests that this binary scenario may be reasonably common in the galactic bulge, since the most massive intermediate mass stars may become enriched in Li as a result of hot bottom burning (Sackmann and Boothroyd 1992). Lithium rich AGB stars have also been observed in the Magellanic Clouds (Smith and Lambert 1989, Smith and Lambert 1990) and in the galaxy (see, e.g. Abia et al. 1991).

4. The cluster 1 bulge planetary nebulae may really be disk planetaries at the same distance as the bulge (Jacoby 1996). It seems possible that high mass objects near the bulge could look kinematically similar to bulge objects. Kinematic studies of these objects might reveal this possibility.

Is there a difference in progenitor metallicity between the bulge and disk PNe? Figure 2.7 is a plot of Ne vs. O, where the symbol notation is the same as in fig 2.6. We assume that Ne and O trace the progenitor metallicity. The line is a least squares fit to the data, the equation being given by:

$$log(Ne/H) + 12 = (1.034 \pm 0.052)(log(O/H) + 12) + (-1.057 \pm 0.454). \quad (2.8)$$

The bulge PNe clearly fall along the same line as the disk PNe, implying that bulge objects have the same constant Ne/O ratio found in disk PNe. This evidence suggests that the rates of enhancement of the ISM by Ne and O relative to each other are the same in the bulge and disk.

We now draw attention to the obvious fact that the natural separation of PNe in our sample into four distinct clusters forms the statistical equivalent of the well-known Peimbert classification scheme (Peimbert 1978). Table 4 shows a comparison of Peimbert type with our cluster classification. For each of our subclusters

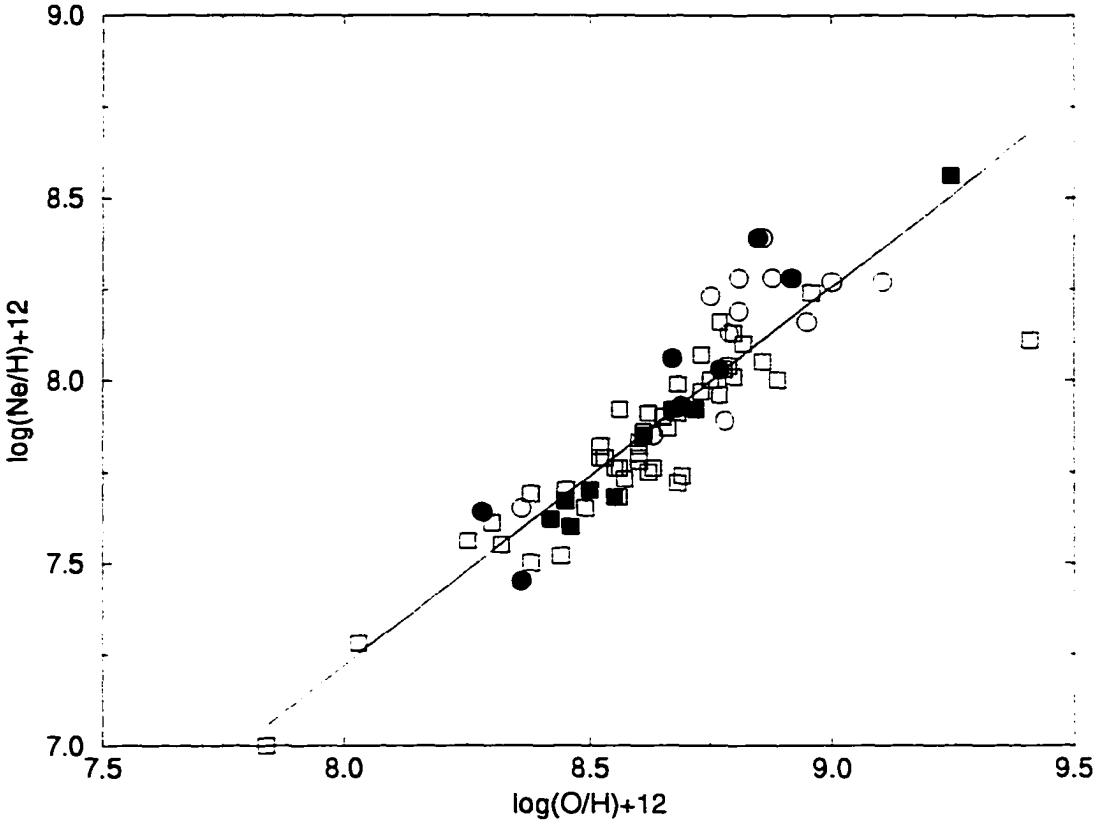

Figure 2.7: log(Ne/H)+12 versus log(O/H)+12 for bulge and disk PNe. The symbols have the same meaning as in the previous graph. The line is a least squares fit to the data.

in column 1, columns 2-5 give the number of objects in that group which belong to the Peimbert types indicated by the headings of those columns. Clearly cluster 1 corresponds to the type I PNe. cluster 2 contains PNe with intermediate nitrogen abundances similar to the type IIa PNe, cluster 3 contains PNe with the lowest nitrogen abundances which is similar to the type IIb and III PNe, and finally the cluster 4 PNe correspond to solar metallicity type V or bulge PNe. The cluster 3 subgroups further bifurcate into type IIb and type III PNe. There also appears to be a bifurcation of the type I PNe. In our scheme the cluster 1a PNe would correspond to an oxygen rich type I and the 1b PNe would correspond to an oxygen poor type I PNe. It seems that the Peimbert scheme is also applicable to the bulge since these planetaries are similar to the disk PNe in composition.

2.5 Conclusions

A multivariate data analysis of galactic planetary nebulae has been carried out with the goal of determining the effective dimensionality of PN parameter space as well as the importance of the numerous observational parameters in classifying PNe. The parameters employed for this study are the abundance ratios He/H, N/H, O/H, Ne/H, N/O, Ne/O, and the spatial and kinematic parameters R, Z, and V_{LSR}. Our main results are:

1. Planetary nebula abundance parameter space is two dimensional, i.e. the data can be described by two principal components. The first and most important one is related to the products of stellar nucleosynthesis during the evolution of PN progenitors. The second component is related to progenitor metallicity.

2. The kinematic properties are not linearly correlated with any other parameters.

3. The disk PNe separate into three clusters, each having a distinct location in the nucleosynthesis-metallicity plane. A fourth cluster comprises many of the bulge PNe. The bulge PNe only separate from the disk PNe because of the inclusion of the parameters R and V_{LSR}.

4. We have identified some unusual type I PNe with extremely low oxygen abundances. However, it is not clear if these are real.

5. Bulge and disk PNe show the same distributions along the nucleosynthesis and metallicity components.

This analysis is a first attempt to characterize planetary nebula parameter space in an objective way. The future addition of parameters such as carbon abundance, nebular expansion velocity, morphology, binarity, and central star mass further improve our understanding of these objects.

Chapter 3

Thermally Pulsing AGB Models

Thermally pulsing asymptotic giant branch (TP-AGB) stars experience two distinct and repeating phases: the helium shell flash or thermal pulse (TP) and the time between pulses or the interpulse phase (IP). The duration of the thermal pulse (t_p) is short compared to the duration of the interpulse phase (t_{ip}) with $t_p/t_{ip} \approx 0.01$. During the TP-AGB, these stars spend most of the time in the interpulse phase, burning both He and H burn quiescently in thin shells. During the interpulse phase, most of the luminosity is produced by the hydrogen burning shell. However. the helium shell in this configuration is unstable, and it will eventually result in a helium shell flash. Thermal pulses occur quasi-periodically, resulting in the luminosity of the helium burning shell increasing by several orders of magnitude. The increased luminosity causes the outer layers of the star to expand, including the hydrogen burning shell. The luminosity generated by hydrogen burning during the shell flash decreases to essentially zero due to the expansion. After the thermal pulse the star resumes its interpulse configuration. This cycle repeats until the envelope is lost via mass-loss.

The two distinctive phases of the TP-AGB have important consequences for the surface abundances of the star. At the end of a thermal pulse it is possible for the convective envelope to penetrate into regions where He has been partially burned into ^{12}C and minor amounts of ^{16}O, mixing these products to the stellar surface.

This process is called the third dredge-up and is believed to be the process by which carbon stars are produced. In the more massive TP-AGB stars it is possible for the base of the convective envelope to get hot enough to burn ^{12}C to ^{13}C and ^{14}N and ^{16}O to ^{14}N in a process known as hot-bottom burning. This process is believed to produce the nitrogen rich PNe. Hot bottom burning can take the carbon dredged-up into the envelope and process it into nitrogen. This is one of the possible solutions to the so-called carbon star mystery.

The third dredge-up occurs at the end of a thermal pulse and mixes helium and carbon rich material into the stars outer layers. During the thermal pulse a convective shell appears in the helium burning zone. This convection zone spans the mass range from the base of the interpulse He burning shell to just below the position of the convective envelope during the preceding interpulse phase. In this zone these important helium burning reactions take place:

- $^{4}He + {}^{4}He \longrightarrow {}^{8}Be + \gamma$
- $^{8}Be + {}^{4}He \longrightarrow {}^{12}C + \gamma$
- $^{12}C + {}^{4}He \longrightarrow {}^{16}O + \gamma$

with the first two being the most important. The third reaction does not occur very often. Therefore, the convective shell at the end of the pulse is composed primarily of helium and carbon. During the transition period between the thermal pulse and the resumption of the interpulse phase the convective shell disappears and the convective envelope can penetrate into this region. The mixing of carbon and helium rich material to the surface layers of the star at the end of a thermal pulse is known as the third dredge-up to distinguish it from the first two dredge-ups which we will describe later.

3.1 Models

3.1.1 The Structure of the Envelope

Computing the structure of a TP-AGB star during the thermal pulse is a difficult task. To follow the thermal pulse from beginning to end requires the computation of a new stellar model with several hundred mass zones over several hundred time steps for each thermal pulse. This process is obviously very time consuming. In addition, these computations are beset by numerical difficulties, in particular the difficulty getting these models to converge (e.g. Frost and Lattanzio 1996). It is also difficult to get the third dredge-up to occur without the presence of some form of extra mixing, i.e. overshoot, semi-convection, etc. Most of these difficulties can be traced to the rapid changes of the stars structure.

Calculating the structure during the interpulse phase is a far less demanding task than doing the same during the thermal pulsing phase. During the interpulse phase the structure changes slowly, so at most only a few models are needed. It is possible to parameterize the effects of the thermal pulses on the star and to partially parameterize the interpulse phase. This technique is known as synthetic modeling and was pioneered by Iben and Truran (1978). The thermal pulses are parameterized so as to calculate the amount of dredge-up and the change in the abundances of all the regions of the star. The parameterization of the interpulse phase is limited to calculating the luminosity as a function of the stellar parameters. The evolution of the envelope of the star can then be calculated using standard techniques.

Our computer code, XYCNO, calculates synthetic TPAGB models. XYCNO is a significantly updated version of a code kindly supplied to us by Dr. Renzini. The changes in the star due to the thermal pulses are parameterized, allowing rapid computation of this phase. The changes in the star (chemical and physical) during the interpulse phase are done by first computing a model of the envelope. The

code computes the envelope structure by taking as an input the interpulse surface luminosity, L_s, guessing T_{eff} and integrating the equations of stellar structure from the surface to the base of the convective envelope. This procedure is iterated until the mass position of the base of the convective envelope, M_{ce}, is the same as the position of the hydrogen-exhausted core, M_c. The output of each envelope integration is the T_{eff} of the model and the structure of the envelope, which are then used to calculate some important parameters such as mass loss and also the envelope nucleosynthesis.

The code follows the abundances of ^{4}He, ^{12}C, ^{13}C, ^{14}N, and ^{16}O in the surface layers of the star. The following nuclear reactions are followed:

- $^{12}C(p,\gamma)^{13}N(e^+\nu_e)^{13}C$
- $^{13}C(p,\gamma)^{14}N$
- $^{14}N(p,\gamma)^{15}O(e^+\nu_e)^{15}N(p,\alpha)^{12}C$
- $^{15}N(p,\gamma)^{16}O(p,\gamma)^{17}F(e^+\nu_e)^{17}O(p,\alpha)^{14}N$.

The rate for each reaction was taken from Caughlan et al. (1988) and references therein. The envelope is assumed to be mixed instantaneously.

The 1995 updated OPAL opacities (κ_{OPAL}) which are described in Rogers and Iglesias (1992) are used when T>10000 K and the molecular opacities (κ_{mol}) of Alexander and Ferguson (1994) are used for T<6000 K. At intermediate temperatures a weighted average of the both types of opacities is used. Points not on the grids are computed using the quadratic interpolation scheme of Rogers and Iglesias. Some of the molecular opacities were checked using the PHOENIX code (Hauschildt 1992ab, 1993) and found that they agree to within 1-4% .

3.1.2 Mass Loss on the AGB

The *relationship* between the zero-age main sequence (ZAMS) mass and the white-dwarf (WD) mass M_i–M_f of Weidemann (1987) indicates that low and intermedi-

ate mass stars must lose $\sim 0.3-7.0 M_\odot$ of mass between the main sequence and the white dwarf stages. AGB stars are observed to be losing mass with rates ranging between $10^{-8} - 10^{-4} M_\odot$ yr^{-1} (e.g. Whitelock et al. 1994). Therefore the AGB is probably the evolutionary phase where most of the mass loss takes place.

Observations of AGB stars indicate that the mass-loss rate probably goes through two phases: a period of moderate mass-loss where an ordinary wind operates ($\dot{M} < 10^{-5} M_\odot$ yr^{-1}), then a rapid transition occurs and the star loses mass via a "superwind" where $\dot{M} \sim 10^{-4.3} M_\odot$ yr^{-1} (Renzini 1981). The mass-loss during the ordinary wind phase is often represented by the Reimers (1975) mass-loss relation given by

$$\dot{M}_R = -(4 \times 10^{-13}) \eta LR/M \tag{3.1}$$

where $\dot{M}$ is in $M_\odot$ yr^{-1}, the luminosity L, the radius R, and the mass M are in solar units. η is a parameter of order unity.

Bazan (1991) and Vassiliadis and Wood (1993) have derived relations between $\dot{M}$ and pulsation period P. Both find that the observational data can be fit with two components; Below P$\approx$600 days there is a linear relation between $\dot{M}$ and P and for periods longer the mass loss rate is constant ($\sim 5 \times 10^{-5} M_\odot$ yr^{-1}).

There is considerable scatter in the data with any given period having stars with mass-loss rates that vary by an order of magnitude. In fact, comparison of the relations of Bazan and of Vassiliadis and Wood indicate a qualitative similarity but quantitatively, $\dot{M}$ varies by up to a factor of 5. Iben (1995) also notes that the brightest galactic OH/IR stars are optically invisible but long-period variables in the Magellanic Clouds with similar pulsation periods are optically visible, indicating a smaller mass loss rate. Clearly, there is no unique $\dot{M}$–P relationship.

Bowen (1988), Bowen and Willson (1991), and Willson et al. (1995) have developed a promising theory of AGB mass-loss rates. The pulsations of the long period variable stars causes shocks in the atmosphere. These shocks levitate the atmosphere, increasing the scale height considerably. The outer parts of the atmosphere

have higher densities than they would otherwise have in a static atmosphere, this allows larger grain nucleation further from the star. The grains are accelerated outward by radiation pressure. The grains transfer momentum to the gas and this drives the mass loss. In this formulation, the mass-loss goes through two stages; mass is lost by an ordinary wind until a certain critical luminosity is exceeded at which point the mass-loss rate increases rapidly to superwind like rates. The critical luminosity increases as the metallicity of the star is decreased.

In this model three different mass-loss rates are used:

1. The Reimers mass-loss rate. $\dot{M}_R$, given above.

2. A Pulsation period mass loss rate, $\dot{M}_{PP}$, given by

$$\log \dot{M}(M_\odot \text{ yr}^{-1}) = -11.4 + 0.0123P \tag{3.2}$$

$$\log P \ (days) = -2.07 + 1.94 \log R/R_\odot - 0.9 \log M/M_\odot \tag{3.3}$$

   where R is the radius of the star. Note that we do not include their modification for M> $2.5M_\odot$.

3. A superwind mass-loss rate, $\dot{M}_{SW}$, which we take as $5 \times 10^{-5} M_\odot$ yr^{-1}.

Relation (1) is followed until $\dot{M}_{PP} > \dot{M}_R$, after which relation (2) is used. Relation (2) is used until $\dot{M}_{PP} > \dot{M}_{SW}$, after which a constant mass-loss rate of $5 \times 10^{-5} M_\odot$ yr^{-1} is used.

3.1.3 Surface Luminosity

In synthetic TPAGB modeling, one of the most important parameters to model is the surface luminosity during the interpulse phase. The surface luminosity is one of the outer boundary conditions of the model star. This is not simple as the luminosity depends on mass, core-mass, composition, and pulse number. The luminosity can also vary significantly during each interpulse phase.

The ability in the past to calculate the interpulse luminosity as a function of core-mass is a very useful property for modeling TP-AGB stars. Paczyński (1971) and Uus (1970) discovered that maximum luminosity during the interpulse phase could be represented by the following "core-mass luminosity" relation:

$$L_s = 60000(M_c - 0.495) \tag{3.4}$$

where M_c is the mass of the hydrogen exhausted core or the core-mass. Iben (1975) discovered the following relationship for the luminosity:

$$L_s = 63400(M_c - 0.44)(M/7M_\odot)^{0.19} \tag{3.5}$$

where M is the mass of the star. The above relations were derived from stellar models of mass greater than $5M_\odot$, Wood and Zarro (1981) derived a relation for low-mass stars (M< $3M_\odot$). Boothroyd and Sackmann (1988) derived this core-mass luminosity relation for low-mass stars (M< $3M_\odot$)of solar metallicity:

$$L_s = 52000(M_c - 0.456) \quad 0.52 \lesssim M_c \lesssim 0.7 \tag{3.6}$$

and the following relation for all metallicities:

$$L_s = 238.000\mu^3(Z_{CNO})^{0.04}(M_c{}^2 - 0.0305M_c - 0.1802) \quad 0.5 < M_c < 0.66 \tag{3.7}$$

where Z_{CNO} is the mass fraction of carbon, nitrogen, and oxygen and μ is the mean molecular weight.

Core-mass luminosity relations only give the luminosity at the local "asymptotic" limit. It is well known that the luminosity during the first interpulse does not correspond to the core-mass luminosity relation, and in general 5-10 pulses are needed to reach it. The first thermal pulses occur when the helium burning shell still produces a significant fraction of the luminosity (~50%), but after a few pulses the helium burning shell only produces a few percent of the luminosity.

In recent years, however, it has become apparent that a simple core-mass luminosity relationship (with or without a metallicity dependence) is not appropriate

for intermediate mass stars (M> $3.5M_{\odot}$) The luminosity now appears to depend on the stellar mass as well. Tuchman et al. (1983) showed using semi-analytic arguments that a core-mass luminosity relation holds for AGB stars only when the hydrogen burning shell is separated from the convective envelope. They found that a core-mass luminosity relationship is not appropriate if the convective shell penetrates the hydrogen burning layer. Blöcker and Schönberner (1991) modeled a $7M_{\odot}$ star and found that it did not follow any kind of core-mass luminosity behavior because the convective envelope penetrated the hydrogen burning layer. This effect has been confirmed by the TP-AGB models of Blöcker (1995), Boothroyd and Sackmann (1992), Boothroyd et al. (1993), Lattanzio (1992), and Vassiliadis and Wood (1993).

We have derived a new relation for the surface luminosity for intermediate mass stars (M> $3.5M_{\odot}$). This relation is dependent on mass, core-mass, metallicity, and pulse number. It consists of three parts: 1) a description of the luminosity at the first pulse, 2) the steep rise in luminosity from the first pulse until asymptotic behavior is achieved, and 3) the asymptotic luminosity. The models of Boothroyd and Sackmann (1992), and Boothroyd et al. (1993) with Sharp (1992) molecular opacities. hereinafter Boothroyd and Sackmann models. were used for this purpose. These models were chosen since they compute a reasonably large grid of models in mass and metallicity and the Sharp molecular opacities are probably better than the Los Alamos opacities. Dr. Boothroyd (1995) kindly supplied me with machine readable tables of these models.

As mentioned earlier, the luminosity at the first pulse is less than the asymptotic value. In figure 3.1, the luminosity at the first interpulse of the Boothroyd and Sackmann models are shown. The line is a fit to the Z=0.02 models. The Z=0.01 models also clearly follow a linear relation with a slope nearly identical to the Z=0.02 models. There appears to be a slight trend of decreasing L_s with metallicity. For $M_c > 0.7M_{\odot}$ we adopt the following relation for the luminosity at the first

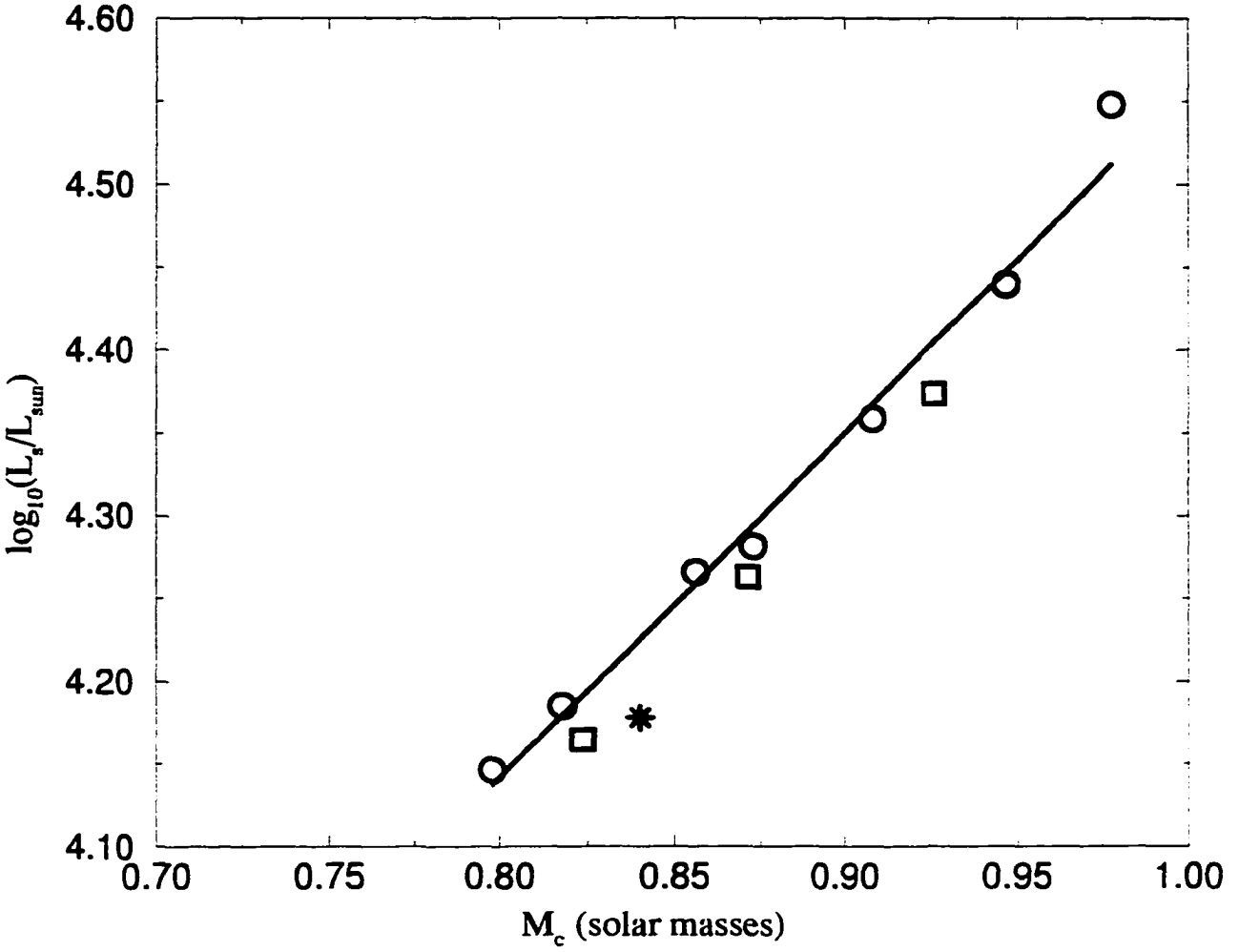

Figure 3.1: Shown in the figure is the interpulse luminosity at the time of the first thermal pulse as a function of core-mass. The Z=0.02, 0.01, and 0.0044 models of Boothroyd and Sackmann (1992) are respectively shown by circles, squares, and stars. The solid line is a least squares fit to the Z=0.02 models.

pulse:

$$\log L_s(0) = 2.07M_c + 2.48 - 3.(.02 - Z) \tag{3.8}$$

where Z is the metallicity of the model. For models with $M_c \leq 0.7M_\odot$ the expressions of Lattanzio (1986) are used:

$$L(0) = 29000(M_c - 0.5) + 1000 \quad Z = 0.001 \tag{3.9}$$

$$L(0) = 27200(M_c - 0.5) + 1300 \quad Z = 0.02, \tag{3.10}$$

where values at other metallicities are found by linearly extrapolating/interpolating in log Z.

A function describing the rise from the luminosity at the first pulse to the local asymptotic limit would be very complicated if it could be described at all. However, in this paper we choose to approximate it with two linear fits, the first describing the rise from the first pulse to a point approximately halfway to the asymptotic value, and the second describing the rise from the halfway point to asymptotic values. The first part, the rise from the first pulse to the halfway point is described by this equation:

$$L_s = A(M_c - M_{c,0}) + L_s(0). \tag{3.11}$$

where A is the slope of the relation. For $M_c > 0.7$ the slope A was found by fitting a line to the luminosity of the first few ($\sim 5 - 7$) interpulses for each Boothroyd and Sackmann model. In figure 3.2 the derived slopes are shown as a function of core-mass and these are fit by two lines. A transition takes place at $M_c \approx 0.87M_\odot$ where the line becomes steeper. We use the following relationship to describe A:

$$A = (218M_c - 182) \times 10^5 \qquad M_c > 0.87 \tag{3.12}$$

$$A = (35.8M_c - 24.2) \times 10^5 \quad 0.71 < M_c \leq 0.87 \tag{3.13}$$

$$A = 1.2 \times 10^5 \qquad M_c \leq 0.71M_\odot. \tag{3.14}$$

For the lowest core-masses we estimated the rate of rise in the low mass models of Boothroyd and Sackmann (1988abcd). When the luminosity is halfway to the

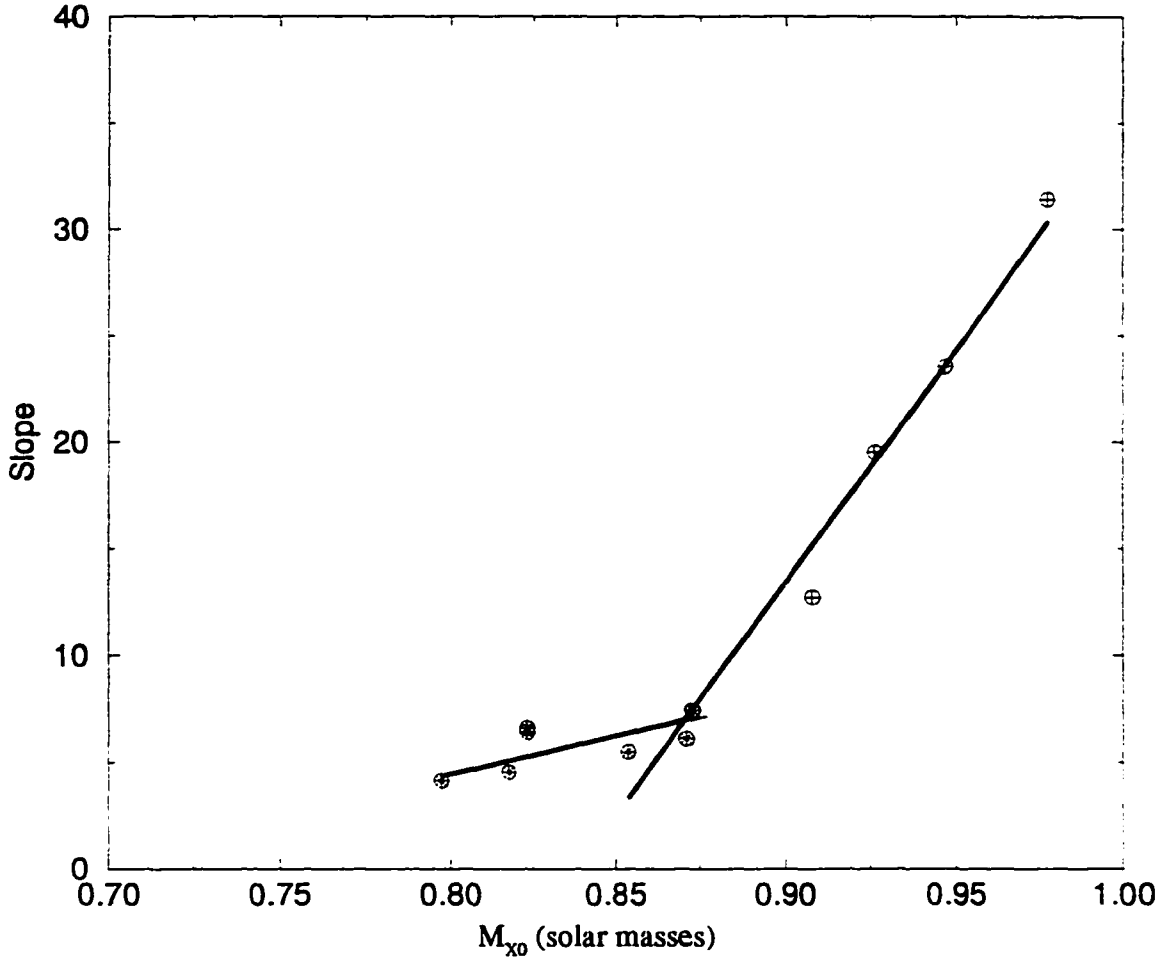

Figure 3.2: The initial rate of rise is shown as a function of core-mass. No metallicity dependence is shown. The two component fit to the data is shown.

asymptotic values. the slope is reduced to half its previous value and is then allowed to continue until asymptotic values are reached. This is done so the shape more closely approximates the behavior of L_s with M_c exhibited by models.

The asymptotic luminosity for all models is found by finding a core-mass luminosity, L_{cm}, and then multiplying L_{cm} by a correction factor, f, which depends on mass. For the Boothroyd and Sackmann models, L_{cm} is calculated from the following:

$$L_{cm} = 52000(M_c - 0.456) \tag{3.15}$$

For each interpulse model f was found by dividing the model luminosity, L_s, by the core-mass luminosity, L_{cm}. The results are plotted in figure 3.3 as a function of mass. The line is a fit to f of the last few interpulses of each model. The fitted line roughly corresponds to the upper luminosity limit of each Boothroyd and Sackmann model. Also, we note the line corresponds to the last few interpulses of several of the Boothroyd and Sackmann models, therefore, we propose to use the line as the asymptotic correction factor.

The asymptotic surface luminosity is found from:

$$L_s = fL_{cm} \tag{3.16}$$

$$f = 1 + 0.186(M - 2.17) \quad M > 2.17M_\odot \tag{3.17}$$

$$f = 1 \quad M \leq 2.17M_\odot \tag{3.18}$$

where M is the mass of the model star and the line fitted in figure 3.3 gives the equation for the correction factor, f. For $M_c < 0.70M_\odot$ equation 7 is used to find L_{cm} and for $M_c > 0.75M_\odot$, it is determined from equation 15. Between $0.70M_\odot$ and $0.75M_\odot$ we linearly interpolate in M_c between the values.

How does the surface luminosity, L_s, behave as a model evolves? In figure 3.4 the evolution of the luminosity of our $5M_\odot$ model with a mixing length parameter, $\alpha = 2.1$, solar metallicity, and a pulsation-period mass-loss law is shown. The model starts with a luminosity slightly below the reference core-mass luminosity

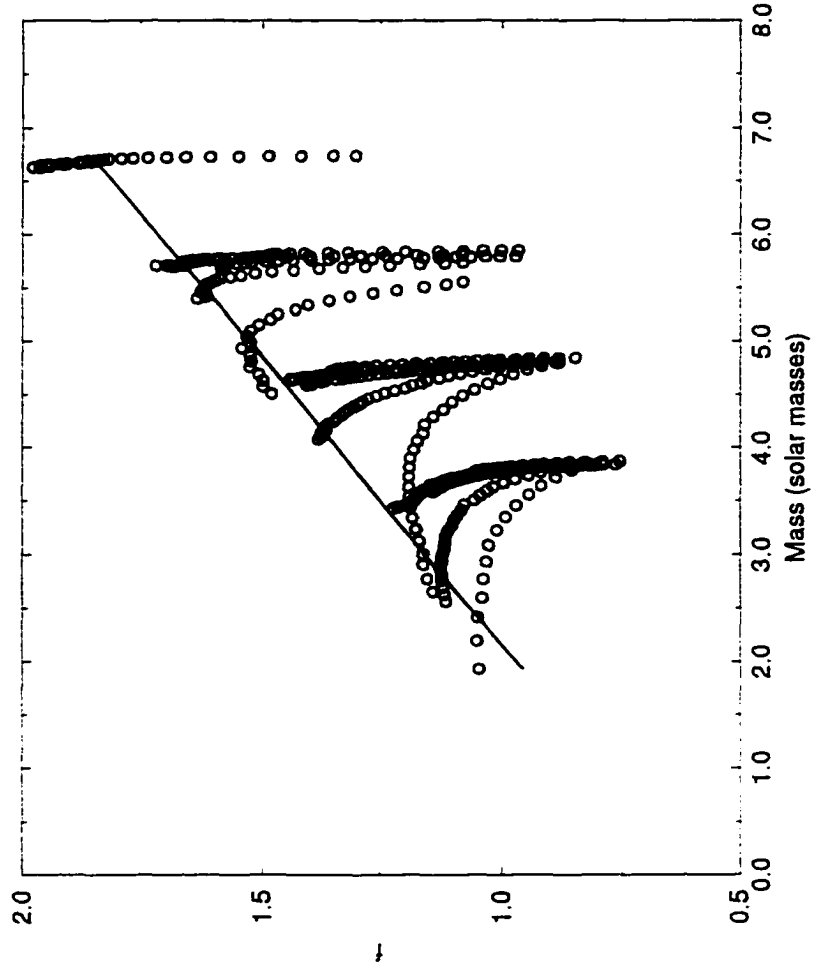

Figure 3.3: The mass correction factor f is plotted versus mass for the Boothroyd and Sackmann models. The solid line is our fit to the asymptotic value of f.

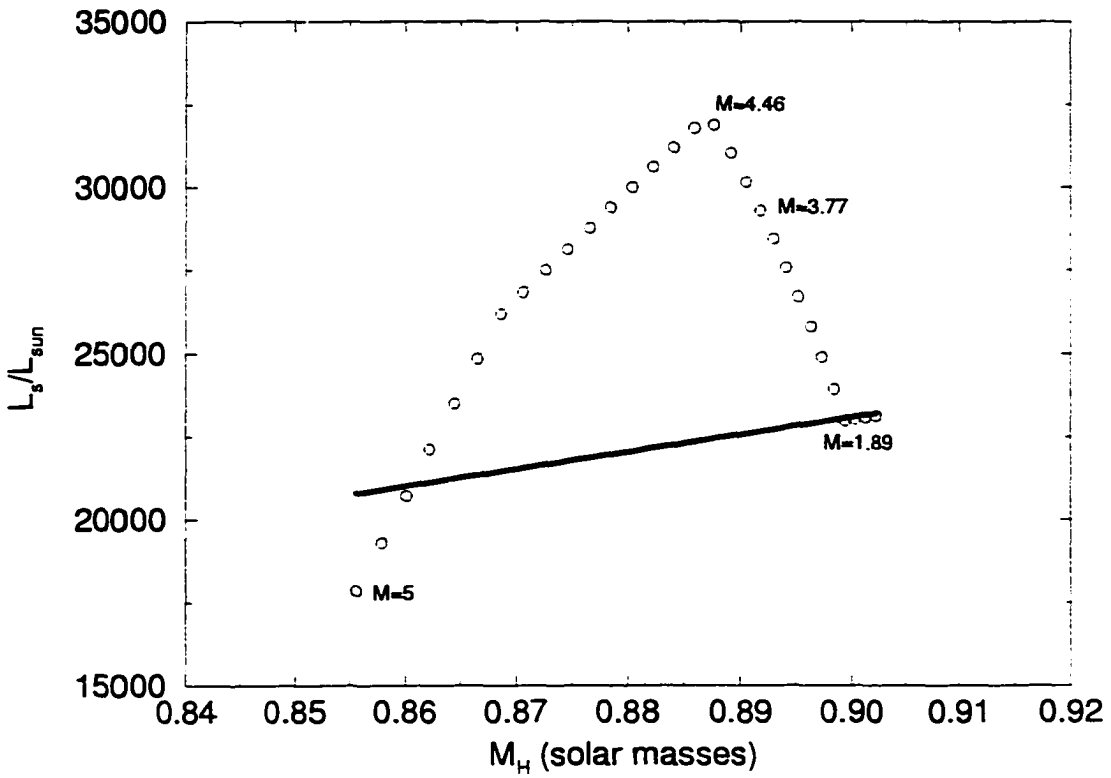

Figure 3.4: The behavior of the interpulse surface luminosity of a 5 $M_\odot$, solar metallicity model, and mixing length parameter α=2.0 model. M_H is the mass of the hydrogen exhausted core. The open circles indicated the luminosities of each interpulse. The solid line indicates the low-mass core-mass luminosity relationship of Boothroyd and Sackmann 1988b. The text on the page indicates the model stars total mass at various points.

relation but it rapidly evolves to nearly twice the core-mass luminosity relation. When the mass reaches $4.77M_{\odot}$ the superwind begins and the star rapidly loses its envelope. During this process the luminosity rapidly decreases and eventually during the last few pulses the luminosity follows a core-mass luminosity relation. This is qualitatively in agreement with the results of Blöcker (1995) and Vassiliadis and Wood (1993) who computed TP-AGB models with mass loss up to envelope ejection. In both of these studies, the models exhibited steep luminosity increases until the superwind began, after which the luminosity dropped until a core-mass luminosity relation was again followed. This occurred because as the mass of the envelope is reduced by the wind, hot-bottom burning contributes less to the total luminosity and eventually the temperature at the base of the envelope drops so that no significant luminosity is produced in the convective envelope. This is the necessary condition for the star to obey a core-mass luminosity relationship.

Another important feature is the variation of the luminosity during the interpulse phase. Examination of the models of Boothroyd and Sackmann (1988a, hereinafter BS88a) and Vassiliadis and Wood (1993) indicate low-mass AGB stars spend an appreciable fraction of the interpulse phase at a luminosity less than the value indicated by our luminosity relations. Using the models of BS88a, plotted in figure 3.5 is a measure of the time spent at lower luminosities plotted against core mass. The equation of the straight line is fitted to the data is given by:

$$g = -2.33M_c + 1.64. \tag{3.19}$$

In the program the luminosity variation is given by a step function with the star spending gt_{ip} at 50% of the interpulse luminosity, L_s and $(1-g)t_{ip}$ time at 100% of L_s.

3.1.4 The Third Dredge Up

At the end of each TP it is possible for ^{4}He and ^{12}C rich material to be mixed from the core into the convective envelope. This event is known as the third dredge up.

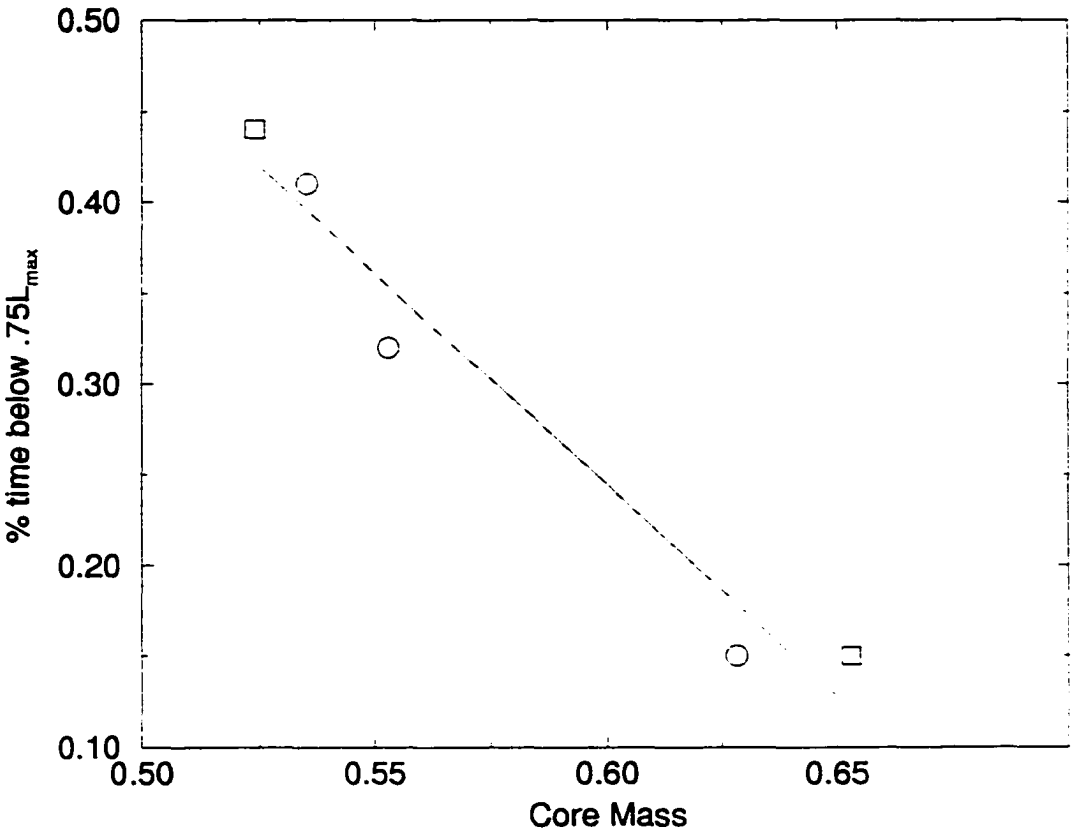

Figure 3.5: The fraction of each interpulse spent below 75% of the maximum luminosity achieved during each interpulse. The line is a least squares fit to the data, and the points are models obtained from table 3 of BS88a

The amount of material mixed upward is determined by the dredge-up parameter

$$\lambda = \frac{\Delta M_{dredge}}{\Delta M_c}. \tag{3.20}$$

where ΔM_{dredge} and ΔM_c are respectively the mass of material dredged up and the advance of the core during the preceding interpulse phase. Recent synthetic models of Groenewegen and de Jong (1993, 1994a, 1994b), van den Hoek and Groenewegen (1996), and Marigo et al. (1996) use a constant λ in their dredge up calculations. While, the use of a constant λ is certainly useful for constraining the amount of dredge up, it is almost certainly too simplistic. Bazan (1991, B91) showed that for dredge-up to occur the peak luminosity of the helium burning shell during the shell flash, $L_{He,max}$, must exceed a certain minimum, $L_{He,min}$, which is dependent on stellar mass. Bazan derived the following equation for the dredge up parameter:

$$\lambda = 0.90(\log L_{He,max} - \log L_{He,min}) \tag{3.21}$$

with the constraint $0 \leq \lambda < 1$.

The peak He shell luminosity, $L_{He,max}$, during each pulse follows a pattern similar to the surface luminosity. At the first pulse the maximum He shell luminosity is well below the local asymptotic value. In the following pulses it experiences a steep rise to the local asymptotic limit. After achieving the asymptotic limit the star continues to follow it. The result is an initially steep rise in $L_{He,max}$ followed by a leveling off or even a decrease once the asymptotic region is reached.

For the peak helium luminosity at the first pulse, $L_{He,max,0}$, we have adopted the expressions in Bazan (1991) with no modification. Note that in this case $L_{He,max,0}$ depends on the initial helium abundance with lower He leading to higher initial luminosities. For the asymptotic values of $L_{He,max}$, different expressions were used for high and low core-masses. For $M_c \leq 0.96 M_\odot$, we use the following expression taken from Bazan (1991):

$$\log L_{He,max} = 48.1 - 125.7 M_c + 84.5 M_c^2 + 62.1 M_c^3 - 63.1 M_c^4. \tag{3.22}$$

For $M_c > 0.96M_\odot$, the expression from Iben (1977) is used:

$$\log L_{He,max} = 3.79 + 3M_c. \tag{3.23}$$

For those pulses between the first and the attainment of the asymptotic values, we approximate $L_{He,max}$ with the following:

$$\log L_{He,max} = A(M_c - M_{c0}) + \log L_{He,max,0} \tag{3.24}$$

where M_{c0} is the core-mass at the first pulse. Bazan (1991) adopts A=34.44, however this is based on models with $M_c \lesssim 0.7M_\odot$. For $M_c \gtrsim 0.8M_\odot$, we estimated that A=65 from the models of Wagenhuber and Weiss (1994). For $0.7M_\odot \leq M_c \leq 0.8M_\odot$, A was found by linearly interpolating in M_c.

A typographical error was found in Bazan's equation for $L_{He,min}$, however we were able to use his model parameters and rederive $L_{He,min}$ as a function of mass, and for $M > 3M_\odot$ we use the following:

$$L_{He,min} = 6.20 + 0.600M - 0.116M^2 + 0.00477M^3 \tag{3.25}$$

while for smaller masses we have created a table of values and interpolate quadratically in mass to get $L_{He,min}$. Shown in figure 3.6 is $\log L_{He,min}$ as a function of mass. The luminosity of the helium burning shell needed for dredge-up to occur is a decreasing function of mass. This result is confirmed by the latest results of Straniero et al. (1997). The results of Straniero et al. indicate $L_{He,max}$'s similar to those of Bazan (1991). Straniero's relation between λ, $L_{He,max}$, and $L_{He,max}$ is similar to Bazan's.

This model has several desirable features and one less than desirable feature. Some of the desirable features are:

1. Dredge-up does not occur during the first few thermal pulses which corresponds to real models.

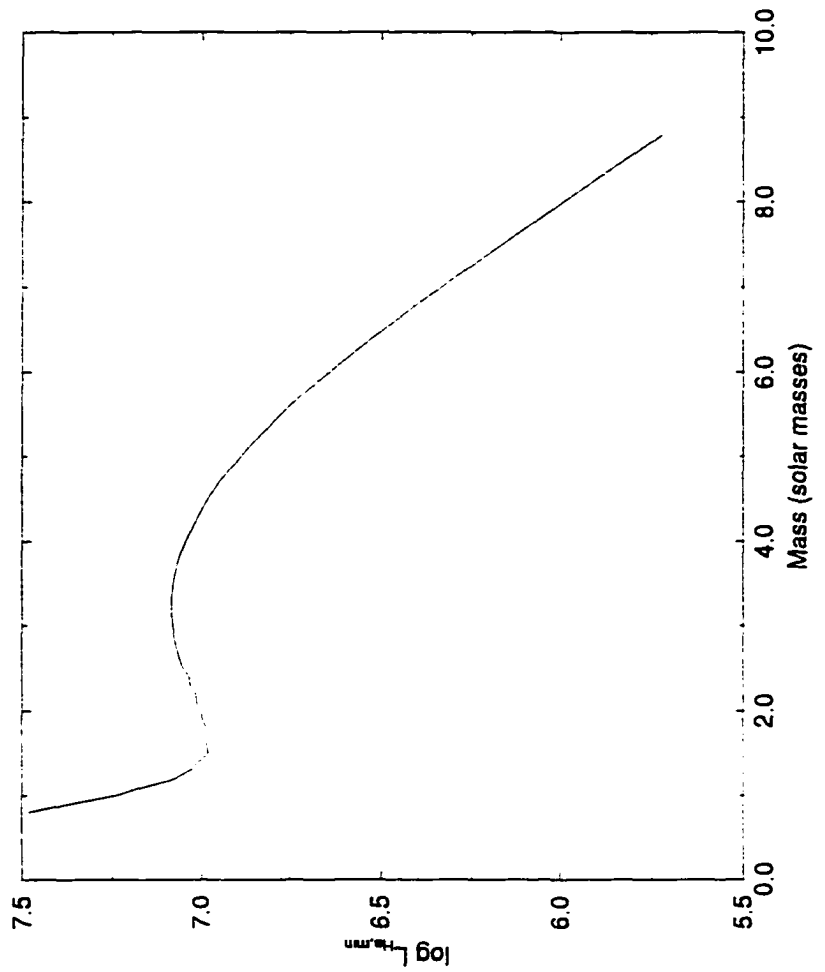

Figure 3.6: The minimum luminosity of the helium burning shell during a thermal pulse required for dredge-up to occur.

2. Once dredge-up begins it starts with a low λ and then grows, which is also predicted by models.

3. The amount of dredge-up is mass dependent, which is also predicted by models.

The undesirable feature is the problem that sometimes dredge-up occurs when the envelope has a low mass. This is a very effective method to pollute the envelope, however, it produces models which do not correspond to observed PNe. In particular, it would produce models of PNe with Galactic metallicity which have high N/O produced by hot-bottom burning, but also high C/O where the enhancement of C/O occurs on the final pulse.

To eliminate the very effective enhancement that can occur at the last thermal pulse, we surpress this pulse if

$$\lambda_{\rm LP} < 0.5\lambda_{\rm max} \tag{3.26}$$

where $\lambda_{\rm LP}$ and $\lambda_{\rm max}$ are respectively the dredge-up parameter of the last pulse and the maximum strength dredge. While this is an ad hoc method of handling this problem, it does to some degree simulate what happens in other models (Straniero et al.1997, Vassiliadis and Wood 1993).

3.1.5 Other Third Dredge-Up Parameters

We determine the composition of the dredged up material from the formulas in Renzini and Voli (1981), with $Y \approx 0.75$, $^{12}C \approx 0.23$, and $^{16}O \approx 0.01$ being the approximate mass fractions.

The mass advance during the preceding interpulse, ΔM_c, is related to the mass of the convective shell formed during the thermal pulse, ΔM_{CSH} by this following expression:

$$\Delta M_c = (1 - r)\Delta M_{CSH} \tag{3.27}$$

where r is the fraction of the current convective shell that will be incorporated into the next pulse. To determine r and ΔM_{CSH} the following expressions from Bazan (1991) are used:

$$r = 11.921M_c^4 - 48.383M_c^3 + 72.288M_c^2 - 47.533M_c + 12.136 \quad (3.28)$$

$$\log \Delta M_{CSH} = -1.2172M_c^2 - 1.1953M_c - 0.47444. \quad (3.29)$$

The above expression for the overlap gives $r > 1$ which is unphysical, therefore for $M_c \lesssim 0.52M_\odot$, so we also use the following expression from Iben (1977):

$$r = 1.5120736 - 1.45932M_c + 0.346M_c^2 \quad (3.30)$$

which is used when the Bazan r exceeds the Iben r.

The duration of each interpulse, t_{ip}, is important for determining the mass-loss and the nucleosynthesis during hot-bottom burning. The interpulse duration is simply the time needed for the core to advance by the proper amount in mass and is therefore given by the following expression:

$$\Delta t_{ip} = 3.14 \times 10^{18} \Delta M_c X_e / L_H \quad (3.31)$$

where X_e is the mass fraction of hydrogen in the envelope and L_H is the average luminosity of the hydrogen burning shell. If hot-bottom burning is taking place then some of the luminosity from the hydrogen burning shell is generated in the convective envelope, any helium produced by hydrogen burning in this region will be mixed up and does not contribute to the advance of the core, therefore L_H is the hydrogen burning luminosity generated beneath the convective shell.

3.1.6 Conditions at the First Pulse

Any AGB code must determine the conditions at the onset of the first thermal pulse as these determine much of the subsequent evolution of the model. The conditions at the first pulse are determined by the preceding evolutionary phases.

The surface abundances at the first thermal pulse are determined by combining published main sequence (MS) levels and changes due to the first and second dredge-ups. The first and second dredge-ups can modify the surface abundances of ^{4}He, ^{12}C, ^{13}C, ^{14}N, and ^{16}O.

The MS levels of the elements are established by scaling the solar abundances of everything except the alpha elements: oxygen, neon, magnesium, sulfur, and silicon to the appropriate metallicity. We chose to set the abundances in the Sun to the levels of Anders and Grevesse (1989). Oxygen, Neon, and Magnesium alpha elements are set as follows:

$$[A/Fe] = 0.4 \quad [Fe/H] < -1.0 \tag{3.32}$$

$$[A/Fe] = -0.5[Fe/H] - 0.1 \quad -1.0 \leq [Fe/H] < -0.2 \tag{3.33}$$

$$[A/Fe] = 0.0 \quad [Fe/H] > -0.2 \tag{3.34}$$

where A is the abundance by number of O, Ne, and Mg. The levels of ^{28}Si and ^{32}S were set to

$$[Si/Fe] = [S/Fe] = 0.2 \quad [Fe/H] < -1.0 \tag{3.35}$$

$$[Si/Fe] = [S/Fe] = -0.25[Fe/H] - 0.05 \quad -1.0 \leq [Fe/H] < -0.2 \tag{3.36}$$

$$[Si/Fe] = [S/Fe] = 0.0 \quad [Fe/H] > -0.2 \tag{3.37}$$

The values for oxygen, magnesium, and silicon were chosen from an examination of the trends in the data of Edvarsson et al. (1993). Henry (1989) (also see Kaler(1975)) showed that neon and oxygen vary in lockstep in PNs and in HII regions, therefore we assume that neon has a similar pattern to oxygen. Other alpha elements such as Ca and Ti have a pattern similar to Si so we assume that S follows the same pattern as Si.

The helium abundance was calculated from the following:

$$Y = Y_0 + \frac{\Delta Y}{\Delta Z} Z \tag{3.38}$$

where Y_0 is the primordial mass fraction of helium. We chose $Y_0 = 0.237$ as this value is close to the recent determinations of Olive and Steigman (1995) and Pagel et al. (1992). We chose the slope so that $Y = Y_\odot$ at $Z = Z_\odot$. The ZAMS hydrogen abundance was chosen so that

$$X = 1 - Y - Z. \tag{3.39}$$

For the Small Magellanic Cloud (SMC) and the Large Magellanic Cloud (LMC), we scaled the metal abundances to solar. The mass fractions of hydrogen, helium, and metals (X, Y, Z) were set to (0.7352, 0.2554, 0.0094) and (0.7491, 0.2462, 0.0047) respectivelly for the LMC and SMC.

The first dredge-up occurs when the star reaches the first giant branch and the convective envelope penetrates into regions where hydrogen burning has occured. This affects the levels of ^{1}H, ^{12}C, ^{13}C, ^{14}N, and ^{16}O. The abundance changes due to the first dredge-up are calculated from the following formulae taken from Groenewegen and deJong (1993). For helium, the change in the mass fraction, ΔY, is dependent on the mass and intial helium content. The change is calculated for two different helium contents shown below:

$$\Delta \mathrm{Y} = \begin{cases} -0.0170\mathrm{M} + 0.0425 & \mathrm{M} < 2 & \mathrm{Y} = 0.3 \\ -0.0068\mathrm{M} + 0.0221 & 2 \leq \mathrm{M} < 3.25 & \mathrm{Y} = 0.3 \\ 0 & \mathrm{M} \geq 3.25 & \mathrm{Y} = 0.3 \\ -0.0220\mathrm{M} + 0.0605 & \mathrm{M} < 2.2 & \mathrm{Y} = 0.2 \\ -0.0078\mathrm{M} + 0.0293 & 2.2 \leq \mathrm{M} < 3.75 & \mathrm{Y} = 0.2 \\ 0 & \mathrm{M} \geq 3.75 & \mathrm{Y} = 0.2. \end{cases}$$

These results are interpolated linearly to get ΔY. The destruction of hydrogen is computed from this formula:

$$\Delta \mathrm{X} = -\Delta \mathrm{Y}. \tag{3.40}$$

$$\Delta^{12}\mathrm{C} = {}^{12}\mathrm{C}(g - 1) \tag{3.41}$$

$$g = \begin{cases} 0.64 - 0.05(\mathrm{M} - 3) & \mathrm{M} < 3 \\ 0.64 & \mathrm{M} > 3. \end{cases}$$

$$\Delta^{14}\mathrm{N} = -1.167\Delta^{12}\mathrm{C}. \tag{3.42}$$

$$\Delta^{16}\mathrm{O} = -0.01^{16}\mathrm{O}. \tag{3.43}$$

with the equations indicating the changes in the mass fractions of the different elements.

For stars in which the second dredge up occurs we use the formulation of Becker and Iben (1980) where the mass of the core before, $\mathrm{M_{cb}}$, and after, $\mathrm{M_{ca}}$, the second dredge up are given by:

$$\mathrm{M_{cb}} = \mathrm{AM} + \mathrm{BM_{ca}} = \mathrm{CM} + \mathrm{D} \tag{3.44}$$

where

$$A = 0.2954 + 0.0195\mathrm{L_Z} + 0.377\mathrm{L_Y} - 1.35\mathrm{L_Y^2} + 0.289\mathrm{L_Z L_Y}$$

$$B = -0.5 - 30.6\mathrm{D_Z} - 412\mathrm{D_Z^2} - 1.43\mathrm{D_Y} + 29.3\mathrm{D_Y^2} - 204\mathrm{D_Z D_Y}$$

$$C = 0.0526 + 0.754\mathrm{D_Z} + 54.4\mathrm{D_Z^2} + 0.222\mathrm{D_Y} - 1.07\mathrm{D_Y^2} + 5.53\mathrm{D_Y D_Z}$$

$$D = 0.59 - 10.7\mathrm{D_Z} - 425\mathrm{D_Z^2} - 0.825\mathrm{D_Y^2} - 44.9\mathrm{D_Y D_Z}$$

and

$$\mathrm{L_Z} = \log \mathrm{Z_i}$$

$$\mathrm{L_Y} = \log \mathrm{Y_i}$$

$$\mathrm{D_Z} = \mathrm{Z_i} - 0.02$$

$$\mathrm{D_Y} = \mathrm{Y_i} - 0.28$$

with $\mathrm{Y_i}$ and $\mathrm{Z_i}$ being the inital He and metal abundances.

The material mixed out by the second dredge-up has experienced complete hydrogen burning. Therefore, all the hydrogen will have been burned to helium

and most of the CNO nuclei will have been converted into ^{14}N. So. the composition of the material in the second dredge is determined by

$$Y_{2dr} = X + Y$$

and

$$X_{14,2dr} = 14(\frac{X_{12}}{12} + \frac{X_{13}}{13} + \frac{X_{16}}{16}) + X_{14}$$

where the mass fractions on the right-hand side of the equations are those of the star before the second dredge-up. All the other mass fractions of the dredged-up material are set to zero.

3.1.7 Core Mass

When convective overshoot is ignored. For low mass stars the mass of the hydrogen exhausted core (M_H) at the first thermal pulse is given by the expression found in Lattanzio (1986).

$$M_c(0) = \begin{cases} 0.53 - (1.3 + \log Z)(Y - 0.20) & Z \geq 0.01 \\ 0.524 + 0.58(Y - 0.20) + (0.025 - 20Z(Y - 0.20))M & 0.01 > Z \geq 0.003 \\ (0.394 + 0.3Y)\exp(0.10 + 0.3Y)M/M_\odot & Z < 0.003. \end{cases}$$

If the second dredge occurs the core mass at the first pulse is given by M_{ca}. The realtion above is used until it reaches M_{cb}.

Chapter 4

Model Predictions of Element Production in Intermediate-Mass Stars

Using the methods described in chapter 3, a large grid of TP-AGB models in mass, metallicity, and mixing length parameter has been computed. The results of these models are presented in Appendix A. Tables of these models are available by anonymous ftp (some computer address to be determined) or via the World Wide Web at (some site to be determined). The model parameters were chosen to form a dense grid in mass. Table 4.1 lists the parameters used in the model grids.

A large number of interesting results can be derived from these models, but the ones we are interested in here are the resulting model planetary nebulae (PNe). The output of each model PN is a set of abundances (He, C, N, O, Ne) and a

α	[Fe/H]	Masses
2.3	0.0	1-8$M_\odot$
2.3	0.1	1-8$M_\odot$
2.3	0.2	1-8$M_\odot$
2.3	-0.1	1-8$M_\odot$
2.3	-0.5	1-4$M_\odot$

Table 4.1: Table of Input Model Parameters

stellar core-mass which can be compared to the PN data.

4.1 Effect of Mass and Metallicity on Element Production

The model PN abundance ratios result from the combined effect of mass-loss, the three dredge-ups, and hot-bottom burning. The different nucleosynthetic events will make different relative contributions of the elements listed below:

1. The first dredge-up occurs when a star enters the first giant branch and the convective envelope dips into regions of the star where CNO reactions have taken place. The material mixed to the surface during the first dredge-up has experienced only partial hydrogen burning, primarily transforming ^{12}C to ^{13}C and ^{14}N. Significant amounts of hydrogen is not converted into helium in these zones. Therefore, the expected result is a significant increase in the ^{14}N abundance (as well as ^{13}C) at the expense of ^{12}C, but only a minimal increase in the helium abundance. The abundance of ^{16}O experiences only minor changes ($\sim$1%).

2. The second dredge-up occurs at the entrance onto the early asymptotic giant branch. The convective envelope reaches into the hydrogen exhausted core and mixes He and N into the surface layers of the star, increasing both the helium and nitrogen abundances.

3. At the end of each thermal pulse, the convective envelope can reach into the He-burning shell. Therefore, the third dredge-up mixes the products of partial He burning to the surface. Nitrogen is destroyed during He burning and will not be dredged-up. The dredged-up material will contain ^{12}C and ^{4}He resulting in increases in the carbon and helium abundances.

4. During the interpulse phase of the TP-AGB, the base of the envelope can reach temperatures high enough for CNO reactions to occur. This is known as hot-bottom burning. This will result in the conversion of ^{12}C to ^{13}C and ^{14}N. Some ^{16}O will also be converted to ^{14}N. Given a long enough time to act some ^{4}He will be produced.

Each of these processes has a strong mass dependence and each may also have a strong dependence on metallicity, therefore, PN models should reflect this. Mass-loss is important because it determines the length of time during which the third dredge-up and hot-bottom burning can operate.

As expected, our model results show the resulting abundances have a strong dependence on mass and metallicity. Figures 4.1, 4.3, 4.5, and 4.4 respectively plot the predicted PN abundance ratios for the models of He/H, N/O, log(O/H)+12, and C/O as a function of the ZAMS mass for several different values of [Fe/H]. The mixing length parameter, α, was held fixed at 2.3, since it also has important effects on the model results which are described in section 4.2.1. To facilitate comparisons of the effects of pre-AGB nucleosynthesis and TP-AGB nucleosynthesis, the model abundances at the first pulse for the [Fe/H]=0.0 models have been included.

The two physical parameters which directly affect the resulting model PN abundances are the mass-loss rate and the temperature at the base of the convective envelope. Mass-loss determines the rate at which the envelope is removed and limits the number of thermal pulses. Mass-loss also determines the envelope mass as a function of time and the mass of the envelope determines the dilution of the material dredged-up. The thermally pulsing lifetime, τ_{TP-AGB}, and the number of pulses, N_p, are related to the mass-loss rate. Hot-bottom burning, which occurs when the base of the envelope is hot enough for CNO reactions to occur, determines the amount of both CN and ON cycling. An indicator of which of the CNO reactions occurred in the hot-bottom burning of each model is the maximum attained temperature at the base of the convective envelope, $T_{6.base}$. In some of

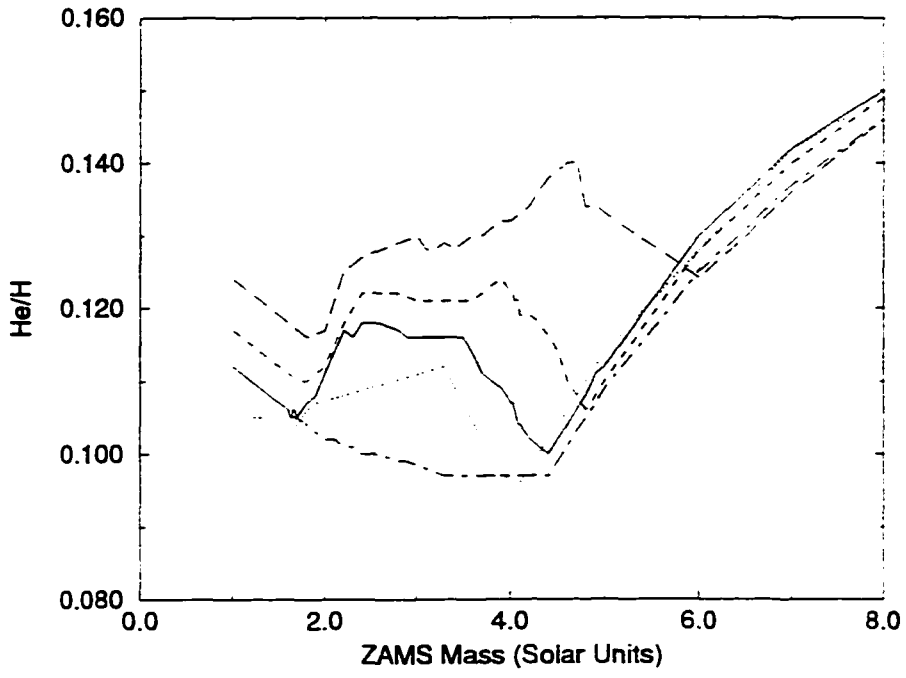

Figure 4.1: Expected value of He/H in PN for model mass between $1M_{\odot}$ and $8M_{\odot}$. The solid line. dashed line, long dashed line and the dotted line respectively indicate models calculated with [Fe/H]=0.0, 0.1, 0.2, and -0.1. The dashed-dotted line indicates the abundance of He/H at the first pulse for the [Fe/H]=0.0 model.

our models. temperatures of nearly 100×10^6K were sometimes attained. Different types of nuclear reactions will be important in different temperature regimes.

1. If $T_{6,base} < 30$K then no hot-bottom burning occurs.

2. If 30K$< T_{6,base} <$50K then ^{12}C is converted to ^{13}C.

3. If $T_{6,base} \gtrsim 50$K then ^{12}C is converted to ^{14}N. Also ON cycling begins converting ^{16}O to ^{14}N.

The panels of figure 4.2 respectively show the age of each model in years. the number of thermal pulses a model experiences. and the maximum temperature achieved at the base of the convective envelope.

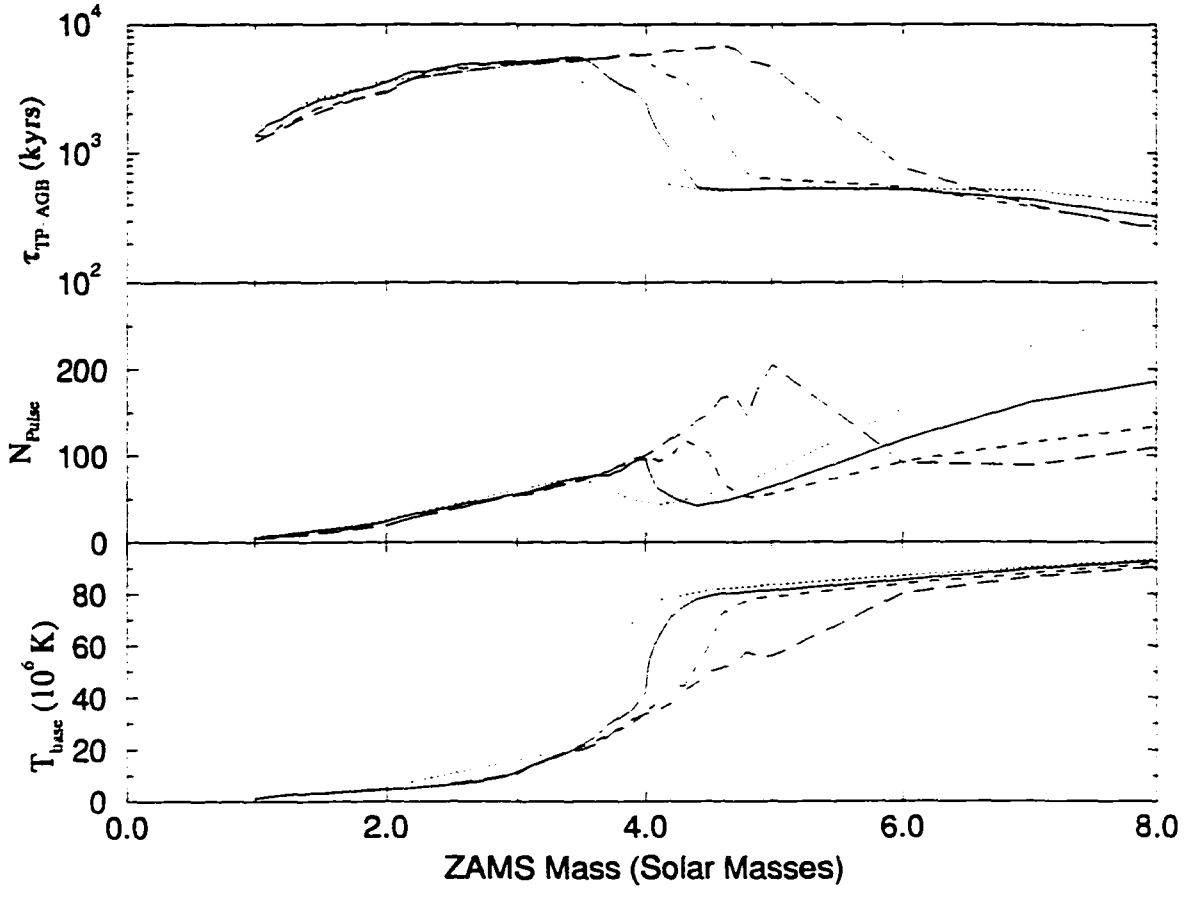

Figure 4.2: The panels from top to bottom indicate the time the model spends on the TP-AGB, the number of pulses, and the maximum base temperature achieved at the bottom of the convective envelope. The lines have the same meaning as figure 4.1

Figure 4.1 shows the He/H ratio to be a complicated function of mass and metallicity. Since helium is produced by each of the three dredge-ups and by hot-bottom burning, it is not surprising that helium shows complex behavior. The resulting PN He/H also appears to depend on the initial helium mass fraction. For each metallicity, He/H has three local maxima and two local minima. The behavior of He/H in between adjoining maxima and minima reflect the dominance of one or more of the acting processes. The first maximum is at $\sim$1.0$M_\odot$ for each metallicity. The second maximum should be regarded as a plateau which stretches from $\sim$2-4$M_\odot$. The third maximum is located at 7-8$M_\odot$ and corresponds to the highest mass model calculated for each [Fe/H] sequence. The first minimum in He/H is located at $\sim$1.7-1.8$M_\odot$ and is weakly metallicity dependent. The second minimum is located at $\sim$4.0-5.5$M_\odot$ and is strongly dependent on metallicity. For the purposes of discussion we divide this mass range into four parts:

1. The region between the first maximum in He/H and the first minimum which we define as the low low mass range,

2. The region between the first minimum and the second maximum which we define as the high low mass range.

3. The region between the second maximum and the second minimum which we define as the low intermediate mass range.

4. The region between the second minimum and the second maximum which we define as the high intermediate mass range.

In the low low mass range ($M \lesssim 1.7M_\odot$), there is no difference between the abundance ratios at PN ejection and the first pulse because no nucleosynthesis occurred during the TP-AGB phase of these models. The base of the envelope never gets hot enough for nuclear reactions to occur. No third dredge-up events occurred in any model in this range, primarily because mass-loss removed the envelope before the strength of the pulses was sufficient to cause it to occur.

In the low low mass range, the third dredge-up does not occur because mass-loss removes the envelope before $L_{He,max}$ reaches values high enough for it to occur. As noted in chapter 3, the peak luminosity of the helium burning shell during the thermal pulse, $L_{He,max}$, controls the occurrence of the third dredge-up. For all TP-AGB stars, $L_{He,max}$ is too small at the first pulse for dredge-up to occur. In subsequent pulses, $L_{He,max}$ rises, and then rises to values high enough for dredge-up to occur. Models in the low-low mass range do not last long enough for $L_{He,max}$ to grow sufficiently to allow dredge-up.

The decrease of He/H with stellar mass in this range is a consequence of the behavior of the He/H ratio with mass in the first dredge-up. Models of the first dredge-up (e.g. Sweigert et al. 1992, Boothroyd and Sackmann 1997) predict that the He/H ratio decreases as a function of mass. Such models also predict in this region an increase in the ratio of N/O. This reflects the transition from the pp cycle to the CNO cycle in stars. Although the scale of figures 4.3 and 4.4 does not clearly show it, in the low low mass range, there is a slight positive correlation between N/O and mass and a corresponding negative correlation between C/O and mass.

The metallicity dependence of the first minimum is tied to the mass-loss scheme. Mass-loss is metallicity dependent. For example, if two AGB stars have the same mass and luminosity but different metallicities, the lower metallicity star will have the smaller radius. In our mass-loss scheme $\dot{M} \propto R^{2.7}$, and therefore the lower metallicity star will take longer to reach the superwind phase and lose its envelope. A longer lifetime on the TP-AGB allows more thermal pulses in which to have a dredge-up. No nucleosynthesis occurs on the TP-AGB for low low mass range objects. The enhancements of abundances over the ZAMS level are due to pre-AGB nucleosynthesis.

Between $1.7M_{\odot}$ and $4.0M_{\odot}$, both the levels of He/H and C/O are modified between the first pulse and PN ejection, but the N/O and O/H ratios remain

approximately constant throughout the TP-AGB phase. The elevation of C/O and He/H results from the action of the third dredge-up. The main components of third dredged-up material are ^{4}He (Y$\approx$0.75) and ^{12}C (X_{12} $\approx$0.23), which leads to significant increases of both He/H and C/O. There is a small decrease in N/O ratio and slight increase in the O/H ratio because of the dredge-up of oxygen on the TP-AGB, which are not visible on figures 4.3 and 4.5, occurs because of the small amounts of ^{16}O dredged-up. The level of ^{14}N is not affected by hot-bottom burning, since the maximum base temperature in this mass range is not sufficient for CN cycling.

According to figure 4.1, the level of He/H found at the second maximum increases with metallicity. The change in the helium mass fraction from the first to final pulse is similar for different metallicities. Therefore the difference in He/H is due to He/H at the first pulse. Pre-AGB mixing episodes in the high-low mass range leave the He/H ratio essentially unchanged. Therefore, the most important factor in determining the level of the second maximum is the ZAMS abundance of He/H.

Between 2 and 4$M_\odot$, figure 4.2 shows metallicity differences have only a minor effect on the number of thermal pulses and τ_{TP-AGB}. The number of thermal pulses is an approximate measure of the number of third dredge-up events, therefore, the mass of helium dredged-up to first approximation does not vary with metallicity.

At $\sim$4$M_\odot$, the beginning of the low intermediate mass range, figures 4.2 indicate a steep drop in both τ_{TP-AGB} and N_P, and a steep increase in the maximum base temperature. Due to the onset of hot-bottom burning, models with mass above $\sim$4$M_\odot$ spend an appreciable fraction of the TP-AGB stage with luminosities in excess of the luminosity indicated by the core-mass luminosity stage. This extra luminosity causes the star to swell to radii larger than if the star followed a core-mass luminosity relationship. Since the mass-loss prescription used here is strongly radius dependent, the average mass-loss is higher and the superwind is reached

earlier. Therefore, there is a significant drop in τ_{TP-AGB}.

The mass of the steep drop in τ_{TP-AGB} and N_P increases with metallicity. Figure 4.1 shows the high mass end of the He/H plateau increases with metallicity. Figure 4.2 shows that the mass of the maximum age model increases with [Fe/H]. The high mass end of the second He/H plateau corresponds to the maximum in age and also to the model with the maximum number of thermal pulses shown. This is not surprising since the number of pulses and the number of third dredge-up events should be correlated.

The precipitous drop in τ_{TP-AGB} and N_P corresponds to the drop in He/H between the plateau and the second He/H minimum. The number of thermal pulses roughly correlates with the number of third dredge-up events and the amount of He dredged-up. Therefore, the cliff in He/H is due to the sharp drop-off in the number of dredge-up events.

The second He/H maximum approximately indicates the lower mass limit to models which undergo hot-bottom burning, M_{HBB}. In the lowest panel in figure 4.2, the rise in the maximum base temperature corresponds to the drop in τ_{TP-AGB} and N_P. When the base temperature exceeds 3×10^7K, significant amounts of CNO burning take place at the base of the envelope, a process known as hot-bottom burning. Clearly, hot-bottom burning is very important in determining the structure of the star. Hot-bottom burning shortens τ_{TP-AGB}, thereby decreasing the number of third dredge-up events and the mass of helium and carbon mixed up by the third dredge-up.

The position in mass of the second He/H minimum and the lower end of the high intermediate mass range is dependent on the lowest mass at which the second dredge-up occurs. On figure 4.1, the second He/H minimum note that there is not much difference between He/H at the first pulse and He/H at the last pulse. Also note, that near the second He/H minimum, there is a steep turn up in He/H at the first pulse (at approximately $4.3M_\odot$). This turn-up indicates the onset of

the second dredge-up. We define this turn-up mass as the mass of the onset of second dredge-up, M_{2dr}. So if the initial mass of the star, M, is greater than M_{2dr}, than the second dredge-up occurs. The amount of helium dredged up depends on M-M_{2dr} in a roughly linear manner.

The lowest mass star of a given mass which experiences second dredge-up, M_{2dr}, is metallicity dependent. Models of second dredge-up (Becker and Iben (1979), Boothroyd and Sackmann 1995) indicate that the minimum mass star which experiences second dredge-up depends on the metallicity. Our second dredge-up prescription is based on the models of Becker and Iben, so the onset of second dredge in our models depends on metallicity.

In the high intermediate mass range, the second dredge-up dominates the other processes in determining the PN He/H. In figure 4.1, for models with [Fe/H]=0.0, there is only a small difference in the models between He/H at the first pulse and at PN ejection. Above $5M_{\odot}$, the level of He/H at the first pulse is due to the second dredge-up. The mixing of helium-rich material due to third dredge-ups into the surface layers causes He/H to increase by a few percent. However, for most of the TP-AGB lifetimes the envelope mass is large compared to the mass dredged-up which strongly dilutes the dredged-up helium.

The behavior of N/O is seen in figure 4.3. N/O is essentially level for $M \lesssim 4M_{\odot}$ at a low value and for $M \gtrsim 4M_{\odot}$ it jumps up to high values. The sudden shift from low N/O to high N/O occurs just before the second He/H minimum. This indicates that the sudden increase in N/O is due to hot-bottom burning. Reference to figure 4.2 indicates N/O begins its steep increase when the maximum base temperature exceeds 50×10^{6}K. Using figure 4.3 and comparing N/O at the first pulse to N/O at the last pulse for the solar metallicity models, N/O has clearly been modified during the TP-AGB for models which experience hot-bottom burning. Therefore, the important factor in determining the N/O abundance is the presence or absence of hot-bottom burning.

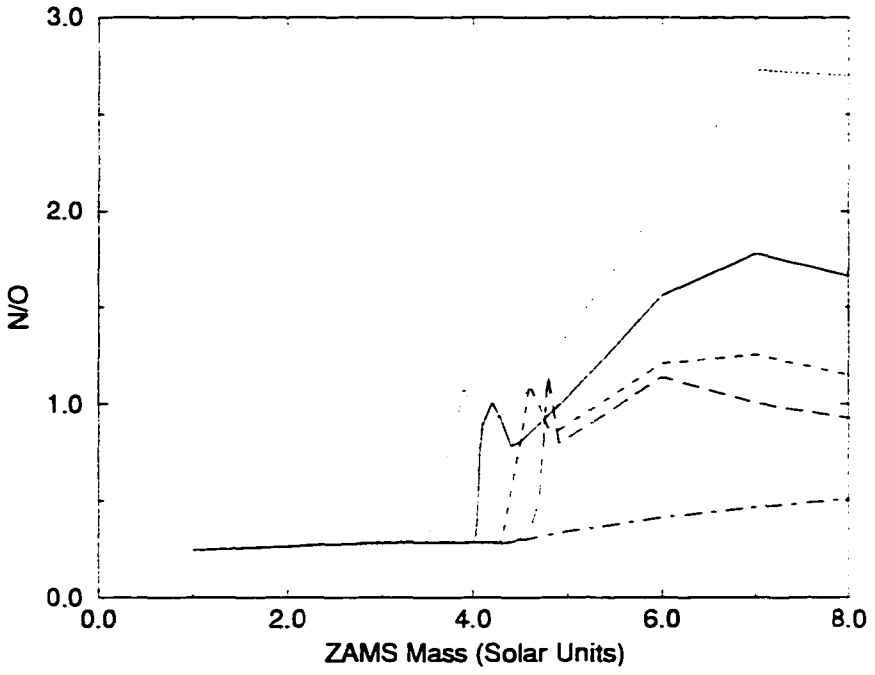

Figure 4.3: Same as figure 4.1 except N/O is compared to ZAMS mass.

It should be noted that N/O can be modified before the TP-AGB phase by both first and second dredge-up. The first dredge-up operates in all models and N/O after the first dredge-up is approximately double its ZAMS value. In figure 4.3. there is a noticeable upturn in the first pulse N/O at $\approx 4.5 M_{\odot}$. This is due to the fact that in these models second dredge-up occurs. Those models which experience second dredge-up also experience hot-bottom burning. Hot-bottom burning dominates nitrogen production when it occurs, therefore, nitrogen can not be used as an indicator of the second dredge-up.

C/O reaches its maximum value in a rather broad plateau in the high-low mass range. In figure 4.4 for all metallicities, C/O is significantly larger than 1 between 2 and $\sim 4 M_{\odot}$. The C/O plateau occurs in the same mass range as the second He/H maximum. The C/O plateau has the same origin as the He/H maximum, third dredge-up. In the region from 2-4$M_{\odot}$, TP-AGB stars have more thermal pulses

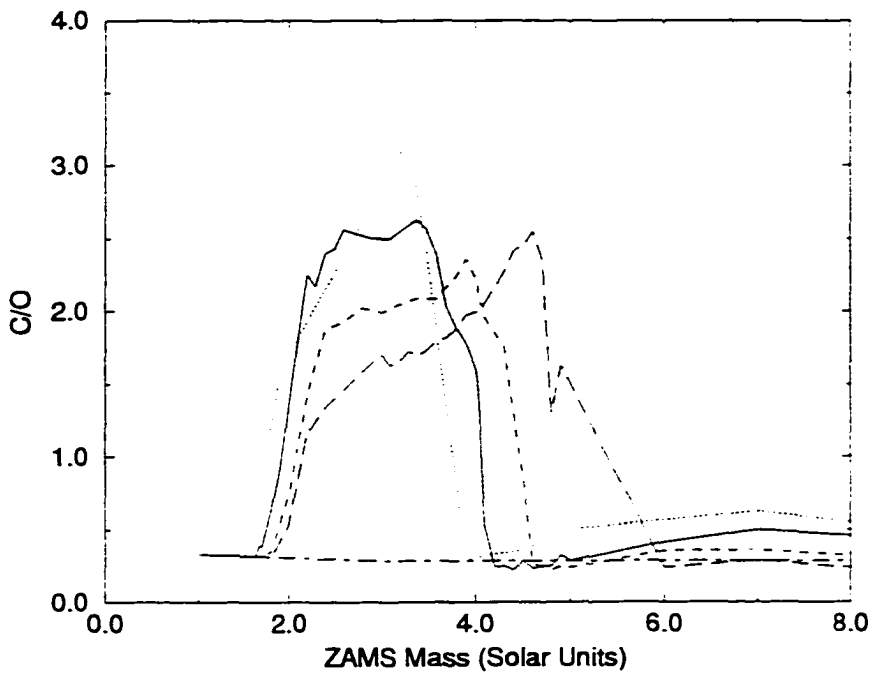

Figure 4.4: Same as figure 4.1 except C/O is compared to ZAMS mass.

than in any other mass range, leading to the largest amount of third dredge-up.

In the low-intermediate and high-intermediate, C/O is much less than in the broad plateau. The drop in C/O corresponds to the increase in N/O in the same range. This is not surprising since carbon will be converted to nitrogen via hot-bottom burning.

In the low-low mass range C/O is low relative to the plateau in the high-low range. Recall, He/H is low in this region because the third dredge-up does not occur. Therefore C/O will be low for the same reason. no carbon is mixed up to the surface layers. This means that level of C/O in the low-low mass range will be determined by the first dredge-up.

Our models indicate that in addition to the CN cycle being active at the base of the envelope during hot-bottom burning, the ON cycle also contributes to the nucleosynthesis. In figure 4.5, for all metallicities, there in the low-low and high-

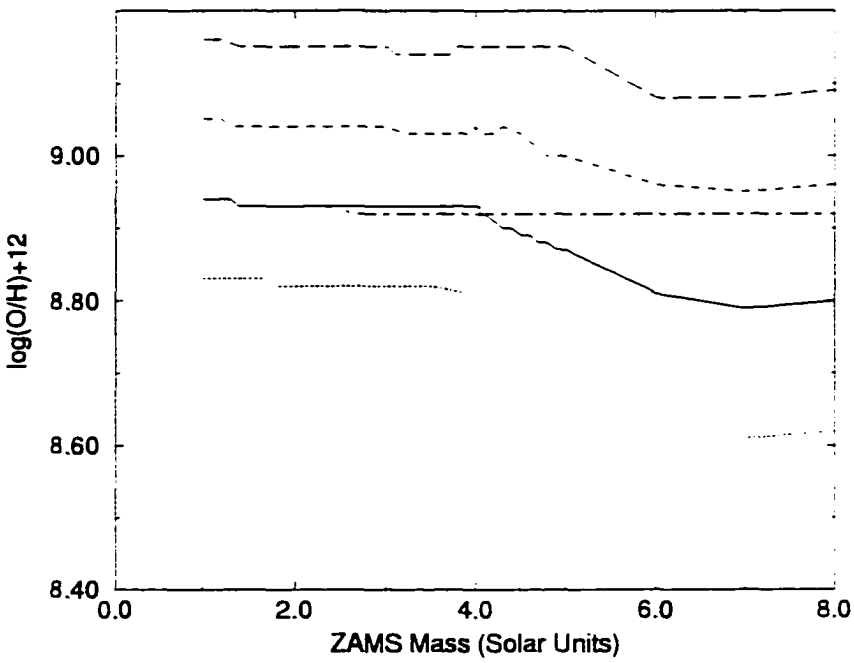

Figure 4.5: Same as figure 4.1 except log O/H+12 is compared to ZAMS mass.

low mass ranges O/H is constant. In contrast, O/H drops significantly in the low-intermediate and high-intermediate mass ranges. The drop occurs in models which experience hot-bottom burning, and it is due to oxygen being converted to nitrogen via the ON cycle. In some of our models the base temperature reaches 60-80$\times 10^6$K, which is hot enough for the ON cycle to operate. Some small amount of oxygen is dredged-up at each thermal pulse, however, in our model this effect does not significantly modify the surface abundance of oxygen.

Note, the decrease in O/H is of the order of 0.1dex (30%). Such a small amount would be difficult to detect unambiguously observationally.

4.2 Summary of Results

The PNe levels of the important abundance ratios He/H, N/O, C/O, and O/H show important changes as a function of the mass of the progenitor star. High

C/O and He/H show up in models in the high-low mass range, which indicates they have undergone multiple third dredge-up events. In the low-intermediate mass range, the models exhibit high N/O but low C/O and low He/H indicating hot-bottom burning but not much dredge-up. In the high-intermediate mass range, models give high PN N/O and He/H but low C/O, indicating hot-bottom burning and second dredge-up. The abundance ratio O/H reflects the presence or absence of hot-bottom burning, in the low-mass range, models exhibit no ON cycling and in the intermediate mass range, ON cycling is indicated.

Some of these results are qualitatively similar to those of other investigators. The models of Renzini and Voli (1981) with hot-bottom burning indicate that C/O is enhanced in the low-mass region and N/O and O/H are respectively enhanced and depleted when hot-bottom burning occurs. Similar results have also been reported by Boothroyd et al. (1993), Forrestini and Charbonnel (1997), Groenewagen and deJong (1993, 1994), and Marigo et al. (1996).

There is general agreement between our models and others on the He/H abundance, however, we believe we are the first to report the possibility of the second He/H minimum.

4.2.1 The Importance of Mixing Length

Important uncertainties result from the use of the mixing length theory. To account for convection, we use the mixing length theory. The distance a convective element travels relative to the pressure scale height before being it is destroyed is a free parameter. Different choices of mixing lengths have significant effects of stellar structure.

The mixing length parameter, α, has important effects on TP-AGB evolution. The stellar radius, $R_\star$, depends inversely on α. In our mass-loss scheme, the mass-loss rate, $\dot{M}$, varies directly with $R_\star$ to some power. The time on the TP-AGB, τ_{TP-AGB}, depends inversely on the mass-loss rate. Therefore, τ_{TP-AGB} is directly

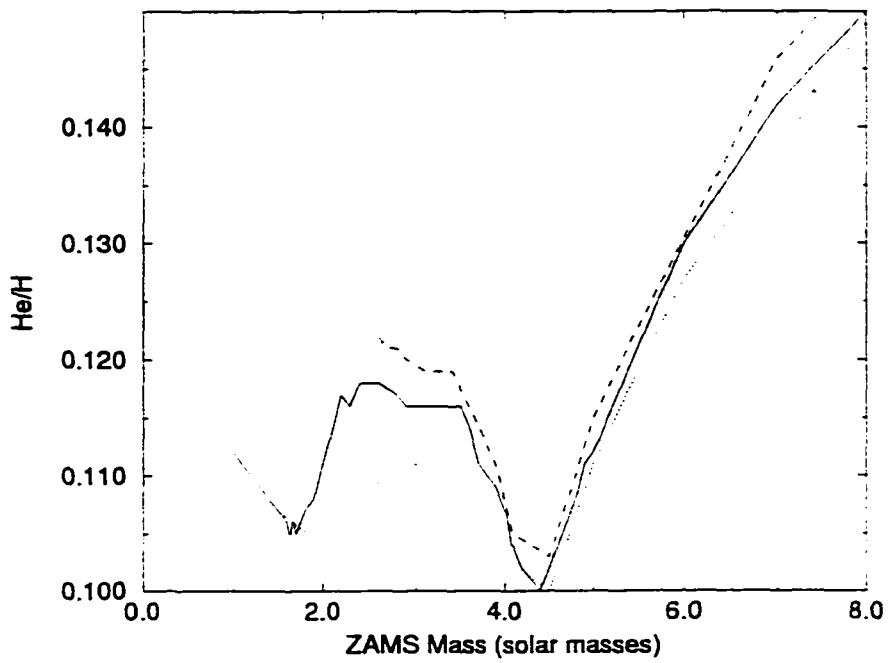

Figure 4.6: Behavior of He/H as a function of α and ZAMS mass. all models have [Fe/H]=0.0. The dotted, solid, and dashed lines indicate respectively model grids with the mixing length parameter, α, respectively set to 1.9, 2.3, and 2.5.

proportional to α, i.e. as α increases so does the mean lifetime.

The increase in lifetime with mixing length parameter, allows more time on the TP-AGB for nucleosythesis. A longer lifetime allows for more thermal pulses and thus more third dredge-up events. This should lead to higher final C/O and He/H in low mass models for higher α. As expected, in figures 4.6 and 4.7 both He/H and C/O increase with α. In the models with $M \gtrsim 4M_{\odot}$ this leads to higher N/O, because more carbon is dredged up and then converted to nitrogen. As expected, N/O increases with α in figure 4.8. By increasing α, the time a model experiences hot-bottom burning increases. If the time of hot-bottom burning increases than so should the amount of ON cycling, this effect of this can be seen in figure 4.9 where O/H decreases with α.

Since there is no simple physical limit on α, the differences in α should be

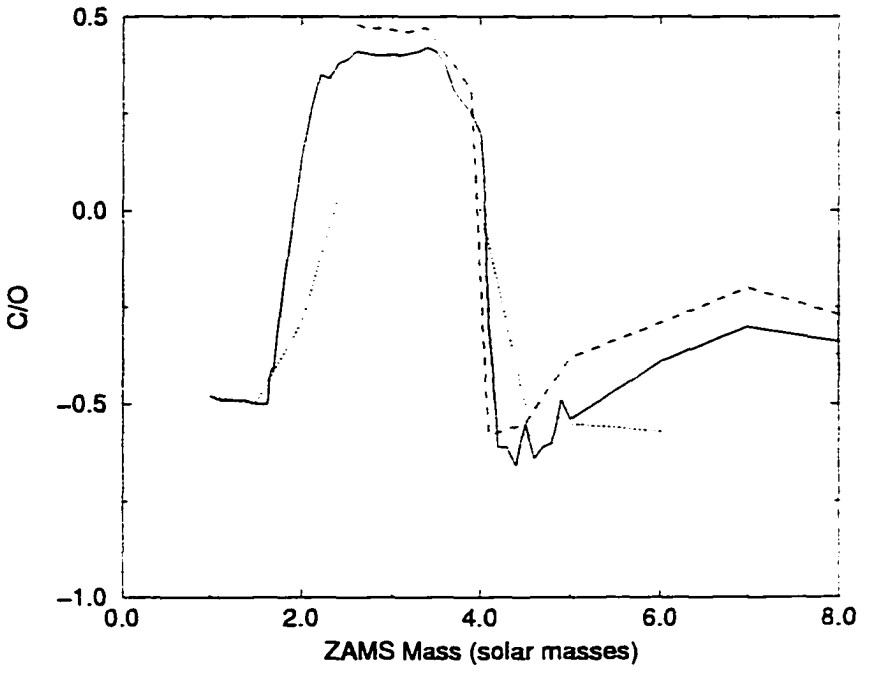

Figure 4.7: Same as figure 4.6 except C/O is compared to α and ZAMS mass.

regarded as the model errors. Clearly changing α makes important differences in the predicted abundances. We determined the "best" value of α by deciding which set of solar metallicity models provided the closest match to the PNe data. We came up with $\alpha = 2.3$. This is similar to the $\alpha = 2.1$ used by Boothroyd and Sackmann on which our luminosity model is based.

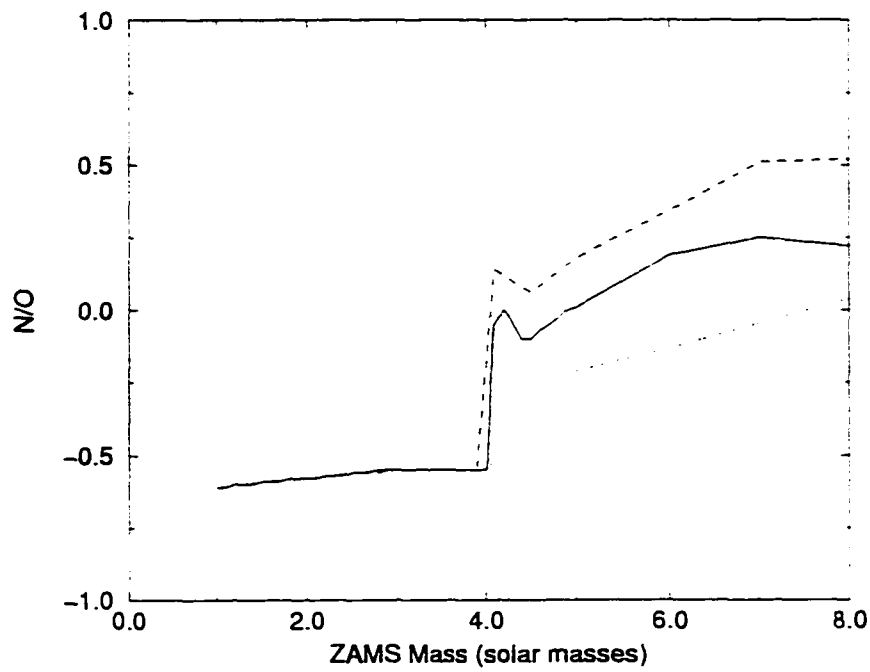

Figure 4.8: Same as figure 4.6 except N/O is compared to α and ZAMS mass.

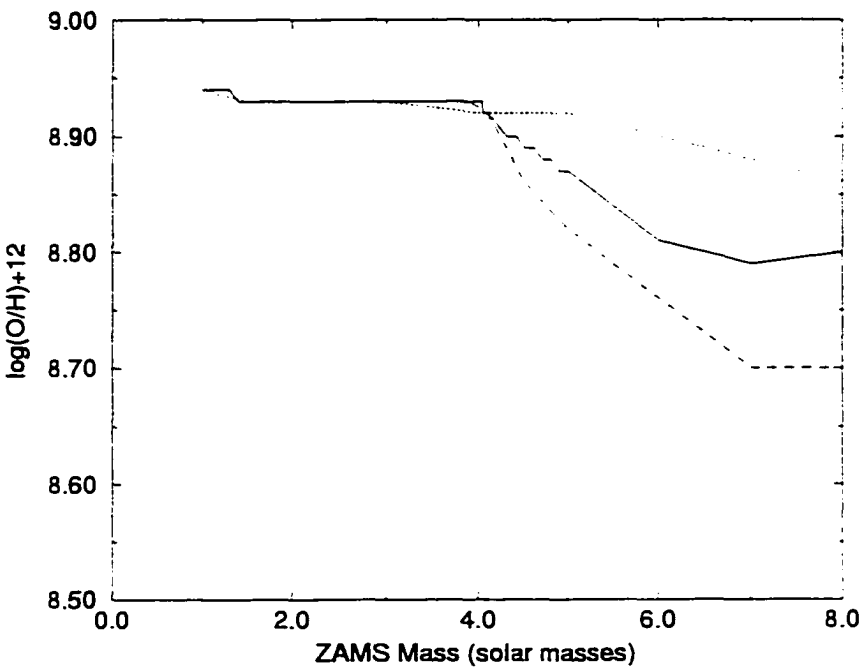

Figure 4.9: Same as figure 4.6 except O/H is compared to α and ZAMS mass.

Chapter 5

The Galaxy

This chapter provides a comparison of the model predictions in chapter 4 with the chemical abundances of Galactic PNe. The comparisons are made on abundance ratio versus abundance ratio plots.

5.1 Data Sets Used

For our comparison between the PNe data and our models, we have chosen two data sets because both have carbon abundances determined from IUE data:

1. The set of Henry and Kwitter described in Henry et al. (1996), Kwitter and Henry (1996), and Kwitter and Henry (1997). This set contains 17 objects for which the abundances of helium, nitrogen, oxygen, neon, and especially carbon have been carefully determined. This data set will be referenced hereinafter as HK.

2. The sample of Kingsburgh & Barlow (1994) which contains 80 southern Galactic PNe, for which the abundances of helium, nitrogen, oxygen, neon, sulfur, and argon were determined. For some PNe the abundance of carbon was also been determined. This data set will be referenced hereinafter as KB.

The abundances in both samples have been determined by using photoionization models to derive ionization correction factors. Both groups determined the abun-

dances of NGC 2440 and NGC 7009. Good agreement is found in the abundance ratios He/H and O/H for NGC2440 and good agreement is found for He/H, N/O, Ne/O, and O/H for NGC7009. When the two samples are placed on abundance ratio-abundance ratio plots, both samples seem to have similar patterns. The halo objects (K648, BB1, DDDM1, and H4-1) are not considered in this chapter since we examine them in chapter 6.

5.2 Metallicity of Galactic PNe

Samples of Galactic PNe usually exhibit a large range in the abundances of O, Ne, and Ar, each of which approximately measures the progenitor's ZAMS composition. In chapter 4, we noted two processes which can affect the surface levels of ^{16}O: hot-bottom burning and third dredge-up, which respectively lower and raise this mass fraction by $\sim$0.15 dex. The abundance of neon can be modified by the production of ^{22}Ne via the reaction chain ^{14}N(α,γ) ^{18}F(β^+,ν) ^{18}O(α,γ) ^{22}Ne which occurs during thermal pulses. The ^{14}N is supplied from the ashes of the hydrogen burning shell. The mass fraction of the dredged-up ^{22}Ne is limited by the mass fractions of the CNO elements and we estimate an upper limit of 0.02 in the case of solar metallicity. Therefore, the surface abundance of ^{22}Ne could have increased by as much as 0.15dex. Such a small change would be difficult to detect although some investigators have claimed it (Perinotto 1991). Sulfur and argon are probably not significantly affected, although *s*-process nucleosynthesis might make small modifications to each element. The possible changes in O/H and Ne/H make them only approximate indicators of progenitor metallicity. However, S/H and Ar/H are better indicators because their surface abundances are less likely to have been modified.

The sample was divided into two subsamples: those with N/O$\leq$0.5 and those with N/O>0.5. From the results of chapter 4, note that models with PN N/O>0.5, the excess nitrogen was produced by hot-bottom burning and second dredge-up.

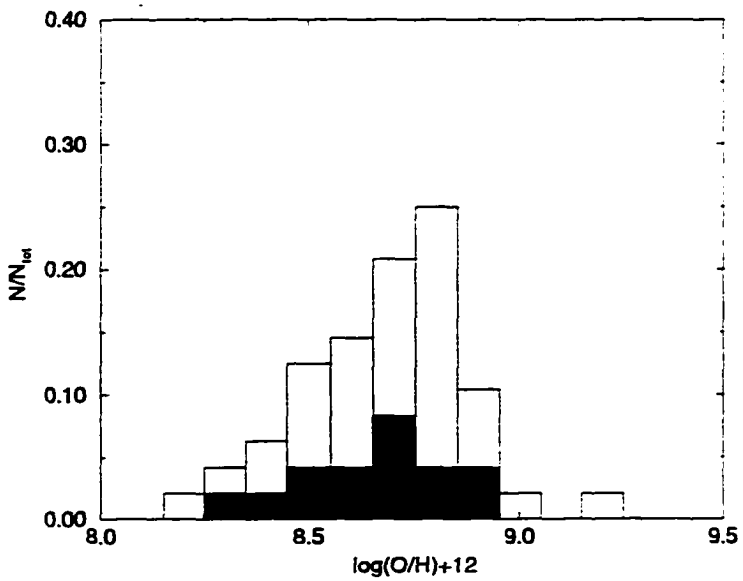

Figure 5.1: Distribution of the O/H abundance ratio of the Kingsburgh and Barlow (1994) and the HK PNe. The open bars indicate the distribution of all the PNe. The solid bars indicate the distribution of PNe with N/O>0.5.

This also appears to be a division in mass with high N/O objects having $M \geq 4.0 M_{\odot}$. Later, we will briefly consider a third subset with intermediate N/O objects, which includes objects with 0.5<N/O<0.7.

Shown respectively in figures 5.1, 5.2, and 5.3 are the O/H and the Ne/H distributions of the KB and HK samples, and Ar/H distributions of the KB sample. Histograms of the full sample and the subsample with N/O>0.5 are indicated on each figure. The majority of high N/O objects lie in a narrow metallicity range: O/H is generally between 8.6 and 8.9, Ne/H is generally between 7.95 and 8.25, and Ar/H is between 6.25 and 6.55. The distribution of sulfur is not shown because the errors in the sulfur abundances are much larger than those of other abundances. If we assume that the random error in the O/H, Ne/H and Ar/H abundances is 0.15dex, then the Ar/H, Ne/H, and O/H data are consistent with a narrow abundance range ($\approx$ 0.1dex). The high N/O objects have a narrower range of X/H than the low N/O objects. High N/O objects from the sample need to be fit by a narrow metallicity range (width=0.1dex) and the low N/O objects need to

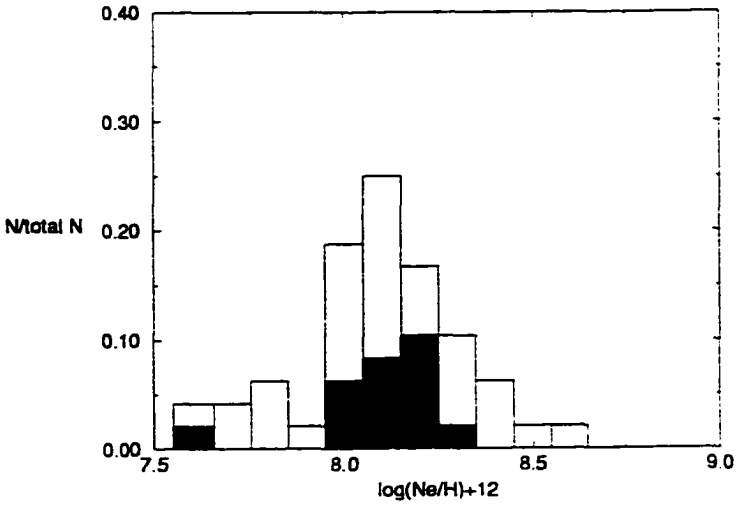

Figure 5.2: Same as 5.1 except the distribution of Ne/H is shown.

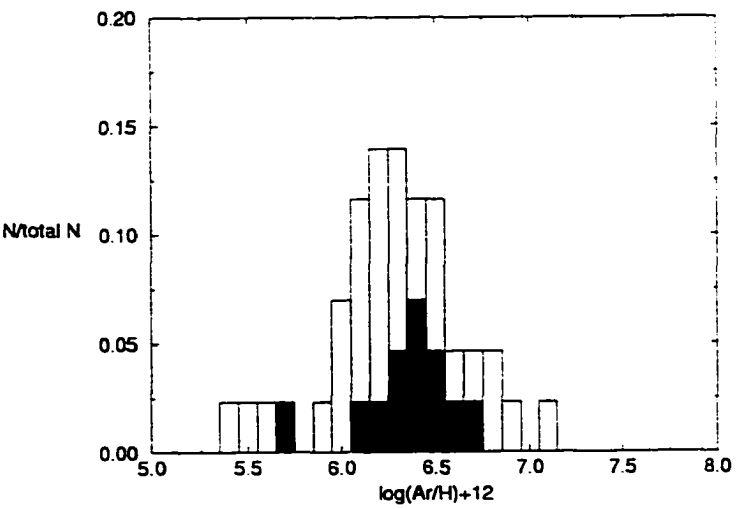

Figure 5.3: Same as 5.1 except the distribution of Ar/H is shown.

be fit by a wide metallicity range.

5.3 Comparison of Models to Data

Comparing the results of TP-AGB star models to PNe data on abundance ratio versus abundance ratio plots gives us insight into what processes are operating. As noted earlier, each abundance ratio results from a unique combination of the nucleosynthetic processes, the initial abundances, and the mass-loss rate. Therefore, by plotting two ratios against each other, one would expect to see features which resulted from the different processes producing the elements.

5.3.1 He/H vs. N/O

Helium and nitrogen are products of hydrogen burning, but models show that each mixing process mixes different relative amounts of each element to the surface. This is different from the simple assumption that one would expect these to vary in lockstep. In fact only the second dredge-up simultaneously produces both substantial amounts of helium and nitrogen. As shown in chapter 4, mass is the most important factor determining which mixing processes operate and to what degree each contributes. Therefore, we expect the signatures of all the different processes to be visible on the He/H-N/O plane.

The abundance ratio N/O is expected to trace the nucleosynthesis of nitrogen. Our models suggest that between ZAMS and PN ejection, the level of oxygen does not change by more than 30% whereas the nitrogen abundance can increase by up to a factor of 4. Therefore, any change in N/O will primarily reflect a change in N and not a change in O. Also, using N/O avoids the difficulty of not knowing the initial N abundance since the ZAMS N/H cannot be easily determined for any individual PN.

Also, using the N/O ratio avoids the potential problems of temperature fluctuations or dust, both of which may reduce the abundances inferred from gaseous

nebulae. Up to 20% of the carbon, nitrogen, and oxygen present can be incorporated onto grains (Meyer 1985) , reducing the inferred abundance by 0.08dex. Temperature fluctuations (Peimbert 1967) can also reduce the inferred nebular abundances. Using N/O avoids these problems since the magnitude of the effects on N and O should be comparable.

The ratio He/H is a measure of the helium production, since He represents the ashes of hydrogen burning.

In figure 5.4, we compare our models to the PNe data on the He/H-N/O plane. Each line consists of several models with different masses but the same [Fe/H]. For the models with [Fe/H]=0.0 to 0.1 we have plotted all of the available models for ZAMS masses between 1 and $8M_{\odot}$. We expect objects with low metallicities to be in the thick disk or to be very old thin disk objects. therefore we have included a series of models with [Fe/H]=-0.5. Since we expect objects with low metallicities to be old we have only included models with a $M_{init} \lesssim 2M_{\odot}$. The metallicity distribution shows tails on both sides of the peak. To account for the high metallicity tail. we included a grid of objects with [Fe/H]=0.2. For the [Fe/H]=0.2 line we have only included objects with $M \leq 4.7M_{\odot}$. Since each line is really a grid of different mass models. we have indicated the positions of certain mass models on the diagram. The range of metallicities is reasonably comparable to the range of metallicities found in dwarf F and G stars by Edvarsson et al. (1993).

Inspection of figure 5.4 suggests that these models fit most of the data reasonably well. We expect the [Fe/H]=0.0 and 0.1 grids to overlap the majority of the PNe. In section 5.2 we showed there are clear peaks in the distributions of metallicity indicators (O, Ne, and Ar) and if we assume the PNe near the peaks have solar metallicity, then most PNe should be explained by the models with [Fe/H]=0.0 and 0.1, particularly those with high N/O. As expected the [Fe/H]=0.0 and 0.1 curves reach most of the high N/O PNe. The near solar metallicity models also

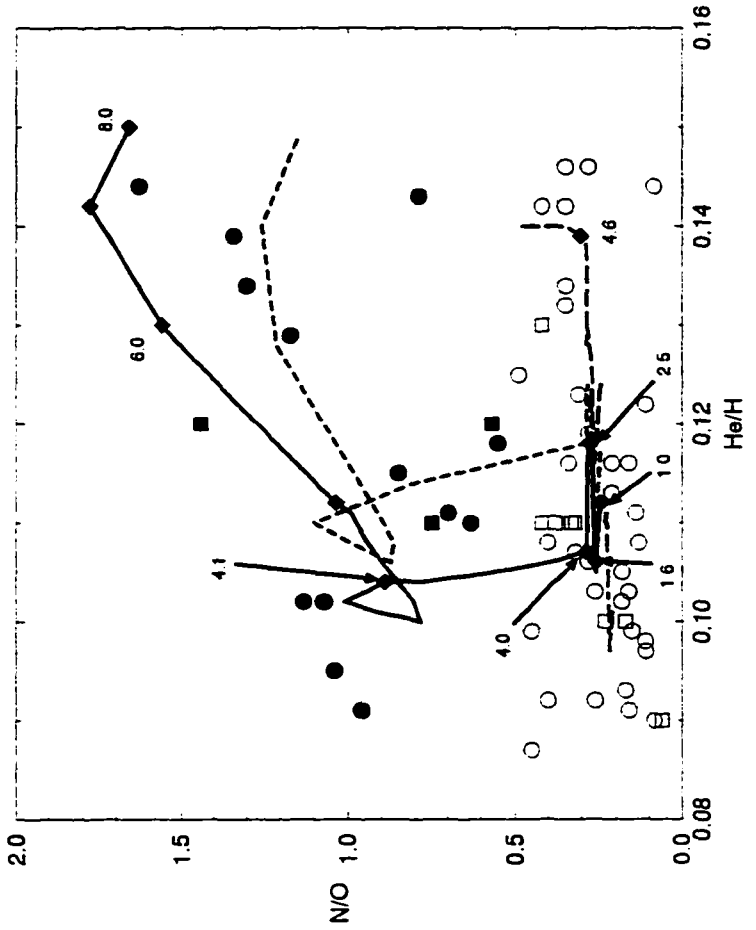

Figure 5.4: The circles and squares represent the KB and HK data sets, respectively. Open and closed symbols respectively indicate PNe with N/O$\leq$0.5 and N/O>0.5, respectively. The solid, dashed, long-dashed, and dash-dotted lines refer to models calculated respectively with [Fe/H]=0.0, 0.1, 0.2, and -0.5. The mixing length parameter, α, of each model was set to 2.3. Only models with M<4.6$M_\odot$ are shown for the [Fe/H]=0.2 and only models with M<2$M_\odot$ are shown for the [Fe/H]= -0.5. The solid diamonds indicate the results of models with [Fe/H]=0.0 and masses of 1.0, 1.6, 2.5, 4.0, 4.1, 6.0, and 8.0 $M_\odot$. Also the position of the model with [Fe/H]=0.2 and mass of 4.6 $M_\odot$ is indicated.

get to most of the low N/O objects. Only two areas where PNe exist cannot be reached by the two near solar metallicity curves:

1. PNe with N/O<0.5 and He/H<0.105, and

2. PNe with N/O<0.5 and He/H≥0.125.

The objects in the first category can be fit with models with less than solar metallicity. Edvarsson et al. (1993) demonstrated that significant numbers of low-mass low-metallicity stars exist in the solar neighborhood, which are probably the progenitors of the PNe in the first category. In figure 5.4 the low-mass [Fe/H]=-0.5 models reach most of the low N/O and low He/H PNe. The figure also shows that objects in the second category can be reached by models with [Fe/H]=0.2 and masses between 2.5 and $4.5M_{\odot}$.

To simplify the comparison between models and data, we have divided the sample and data into 3 subsamples: 1) N/O<0.5, 2) 0.5≤N/O<0.7, and 3) N/O≥0.7. Subsamples 1 and 3 are equivalent to the low and high N/O PNe discussed earlier. We call the lowest N/O PNe type IIb, the intermediate group type IIa, and the high N/O group type I. This classification system resembles the well known Peimbert system (Peimbert 1978), but it is not the same since helium is not included.

To make more detailed comparisons in the models to type IIb PNe, we have "zoomed-in" on the region of figure 5.4 with N/O<0.5 in figure 5.5. For the type IIb PNe, a weak correlation exists between He/H and N/O. Similar correlations have been reported by Henry (1990) and Perinotto (1991) . In general, He/H increases as N/O increases for the type IIb PNe. There is an apparent "forbidden" region on the He/H-N/O plane. The region below and to the right of the light solid line on figure 5.5 is only sparsely populated with PNe.

Our models qualitatively explain both the correlation between He/H and N/O and the "forbidden" region seen in the type IIb PNe. Note that the N/O level of [Fe/H]=-0.5 models is significantly less than that of the solar metallicity models.

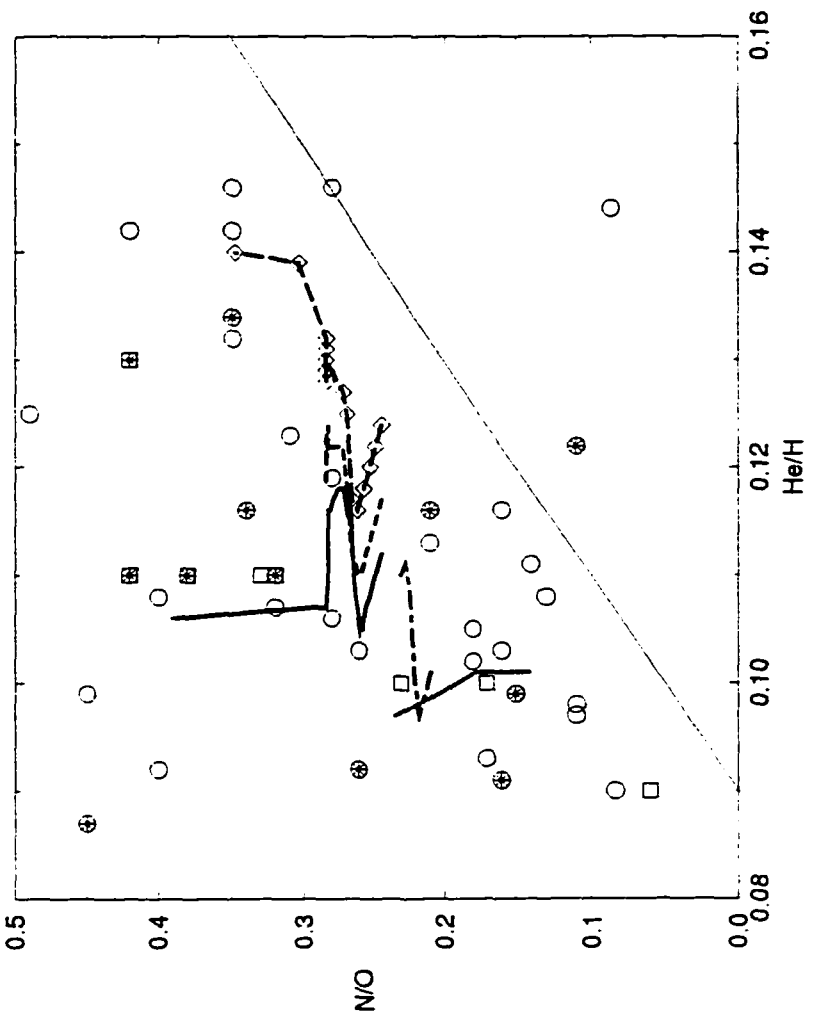

Figure 5.5: The symbols and lines have the same meaning as they do in figure 5.4. Also included is a dotted line, which shows the predicted abundances for stars with [Fe/H]=-0.5 and masses of 0.9, 1.0, 1.1, and 1.2 $M_{\odot}$ using a first dredge-up model based on the recent results of Boothroyd and Sackmann (1997) as explained in the text. The light solid line is a rough approximation of the divide between the allowed and forbidden regions of the plane. The symbols with stars in them indicate PNe with C/O>0.8. Note that many objects do not have an observed C/O ratio.

Also in general, He/H for the thick disk metallicity models are generally lower than those of the solar metallicity models. Examining figure 5.5 and noting the position of the [Fe/H]=0.0 and -0.5 models in particular, the models appear to duplicate the correlation. Each model also predicts a maximum He/H with each given [Fe/H] which explains the existence of the "forbidden" region. In chapter 4, it was noted that the level of the second He/H maxima is a function of [Fe/H]. Since the level of N/O increases with [Fe/H] and there is a maximum He/H for each N/O we expect that the maximum He/H will increase with N/O giving the diagonal boundary of the forbidden region.

The ZAMS level of C/O and N/O have significant effects on the N/O abundance at PN ejection. The most important factor in determining the model type IIb PN N/O is the first dredge-up. The first dredge brings material to the surface from layers where the CN cycle has operated. However, the first dredge can at most double the surface nitrogen abundance. Therefore, if the ZAMS level of C/O and N/O are less than the solar levels, the resulting PN N/O will also be lower. A consequence of our initial abundance is the level of N/O at the first dredge-up will correlate with model [Fe/H] below [Fe/H]=-0.2.

Another minor effect is the increase in the oxygen abundance during the third dredge-up. Increasing the oxygen abundance will cause a corresponding decrease in N/O. The amount of this N/O depletion will decrease with increasing metallicity. This occurs because it is easier to dilute the N/O ratio if the abundance of N is lower.

The first dredge-up increase of N/O with metallicity and the increased impact of the dredge-up of ^{16}O qualitatively explain the He/H-N/O correlation for type IIb PNe, but do they explain it quantitatively? Our diagram indicates reasonable agreement between the models and the data. However, if we consider the models at the extreme metallicities ([Fe/H]=-0.5 and 0.2) they do not have enough range in N/O to reach the lowest or highest N/O PNe. In the case of the high range

in N/O, the disagreement is slight being no more than a 30% difference. Two possibilities exist which would allow the extension of the models to reach the highs and lows of N/O:

1. A slightly different choice of a model for ZAMS C/O and N/O would increase the range of N/O.

2. Our model of first dredge-up needs modification at the lowest masses.

In our model the ZAMS C/O and N/O are constant for [Fe/H]>-0.2. As noted earlier. this reflects the trends in Edvarsson et al. (1993) . This is responsible for the fact that the N/O level in the low mass models ($M \lesssim 4M_{\odot}$) with [Fe/H]$\geq$0.0 is nearly constant on the diagram. However, other models exist (e.g. Boothroyd and Sackmann 1997) in which C/O and N/O never level off but continue to rise as a function of [Fe/H]. If such a model were used it would lower N/O for the [Fe/H]=-0.5 models and raise N/O for the [Fe/H]=0.2 models giving better agreement.

The other possibility was impossible to study until after this work was essentially completed when the tables for the first dredge-up calculations of Boothroyd and Sackmann (1997) became available. They have recalculated the first dredge-up for masses from 0.85-9$M_{\odot}$ and in general their results agree with those of previous investigators. However. they made first dredge calculations at metallicities never before used and also at lower masses than other investigators. Using their results, we estimated that the change in He/H at low mass ranges is unchanged. However, we found that the average change in the nitrogen abundance showed significant differences. In table 5.1. we compare the enhancements predicted by our models and those of Boothroyd and Sackmann. Clearly at the lowest masses significant differences exist. On figure 5.5, we have plotted an estimate of the change in [Fe/H]=-0.5 models with M=0.9, 1.0, 1.1, and 1.2 $M_{\odot}$ using the results of table 5.1. These very low mass models clearly reach low enough in N/O to explain the lowest N/O models. A recalculation of first dredge-up using the models of

Mass	BS97	Our Calc.
0.9	+0.10	+0.26
1.0	+0.20	+0.27
1.1	+0.23	+0.28
1.3	+0.29	+0.29

Table 5.1: Comparison of our model enhancements of log N/O against those of Boothroyd and Sackmann (1997). Their calculations indicate enhancements in N/O depend mainly on mass and appear to depend only very weakly on metallicity at least in the mass range considered.

Boothroyd and Sackmann (1997) may result in slight but important changes in the N/O level. This may bring the high range of N/O into better agreement with the models.

The PNe with He/H$\geq$0.125 and N/O<0.5 deserve more attention. We noted earlier that these objects can be fit by models with [Fe/H]=0.2. However, there is some question whether or not these abundances are real. For one, these objects may be the result of uncertainties in the abundance determination processes, in particular He/H. All but one of the objects in this mass range comes from the KB subsample. Some other samples do not have such objects or have only a few such objects, e.g. Costa et al. (1996) does not have any corresponding objects. Henry (1990) has only one Galactic object with N/O<0.5 and He/H$\approx$0.14. In the HK subsample, the highest He/H is 0.130, which can probably be fit by a model with [Fe/H]=0.1.

Another possibility is those PNe with He/H>0.125 and low N/O have experienced a helium shell flash on the post-AGB, the so-called "born again" phenomena of Iben et al. (1983). If this occurs additional helium-rich material would be ejected into the nebula at the beginning of the PNe stage, substantially increasing the helium abundance in the PN. Can the models of solar metallicity PNe be made to reach He/H=0.140 before the onset of hot-bottom burning? For this to occur He/H must go from 0.100 to 0.140, an increase of 40%. In our models, even with average

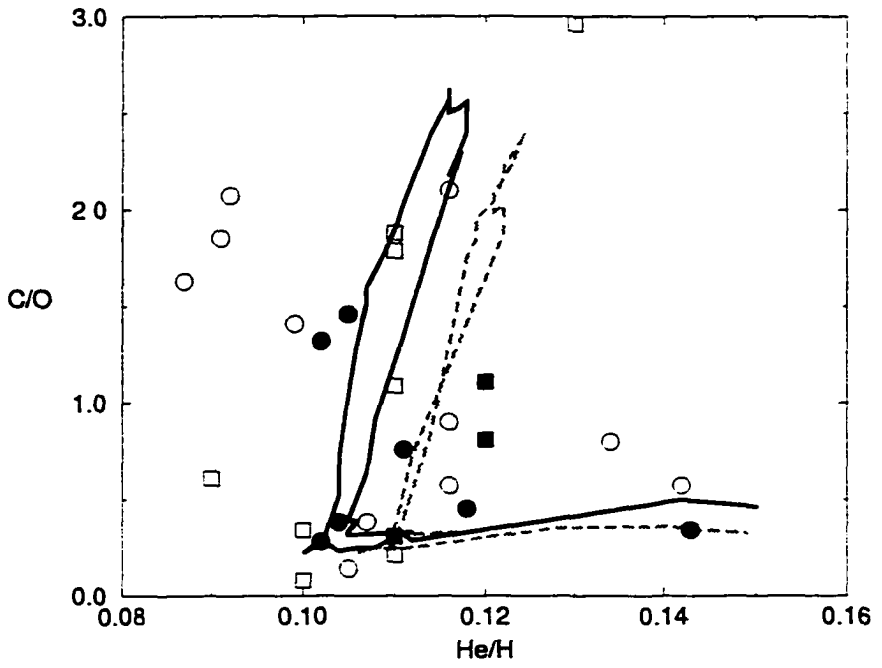

Figure 5.6: The symbols have the same meaning as figure 5.4. The dotted line are the [Fe/H]=-1.0 models.

lambdas of 0.7, this does not seem possible. However, helium is most effectively enhanced during the last few pulses when the mass of the envelope has been reduced. During the last pulse, if the envelope has been reduced to a few tenths of a solar mass or less and a dredge-up occurs it might be possible helium could be enhanced enough to allow a solar metallicity model to reach very high He/H.

5.3.2 He/H vs. C/O

In figure 5.6, a comparison is made between the models and the Galactic PNe on the C/O versus He/H plane. The agreement between models and data is good. Some points of agreement:

1. The near solar metallicity models explain most of the data.

2. The models with the highest C/O seem to correspond to the highest C/O found in the sample (Except for the obvious outlier J900).

3. The models reproduce the overall trends in the data.

The objects with low helium and high C/O (He/H$\lesssim$0.09 and C/O>0.9) present some problem for our model:

1. These could be low metallicity PNe, in which case a model with lower [Fe/H] could be used to fit them. The diagram indicates that these PNe can be reached by models with [Fe/H]=-1.0, suggesting a low metallicity.

2. The measured helium abundances in these objects could be systematically low. For instance, a low helium abundance could be generated if neutral He corrections were required. For two of these PNe, N5873 and I2448, the abundance of He^+ was determined from only a weak λ4471 line. Also, a 10% discrepancy between determinations of He^+/H^+ for the various lines is common in the KB sample. A systematic shift upward by 10% would bring these objects into agreement with the rest.

Either explanation is possible, although we favor the second one, since the objects have extremely low He/H implying a ZAMS He/H of 0.08, which is nearly primordial and therefore seems unlikely.

The masses of selected models are shown in figure 5.7. The objects with C/O>1 are low mass objects. The objects with the highest C/O lie between 2 and 3.5 $M_\odot$. The PNe with intermediate mass progenitors have low C/O due to hot-bottom burning. One discrepancy is the low N/O objects with He/H>0.13. These objects are predicted by these models to have high N/O. These objects could potentially be due to errors in abundance determinations, in particular that of N/O or He/H. For instance Kaler (1983) determined the abundance of N2438 as 0.103 which is significantly different from the value used here. Also if the inferred N/O is too low

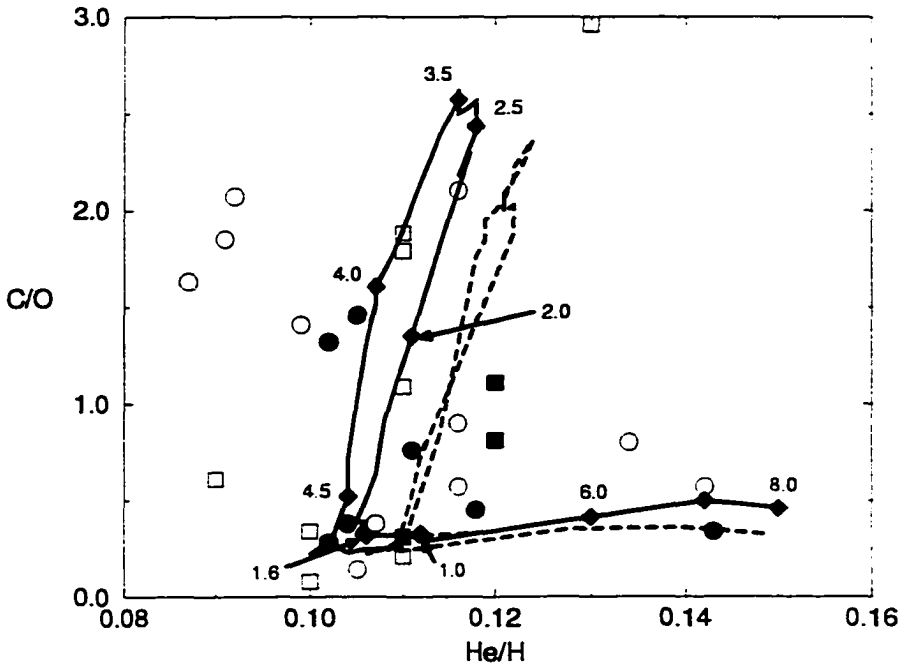

Figure 5.7: Superimposed on the grid of [Fe/H]=0.0 α=2.3 models are the masses of those models.

these objects become high mass objects. Therefore, although these objects are a problem, it is possible they are simply due to errors in abundance determination.

He/H vs. X/H

Our models predict, for low N/O PNe, He/H should reach a different maximum at each metallicity. In figure 5.8, a comparison is made between models and PNe data on the He/H-log(O/H)+12 plane. Clearly, the models do not agree with the data. However, note that the majority of the PNe have observed O/H less than the solar value (8.93, Anders and Grevesse 1989). This is the well known problem that the abundances inferred from lines in gaseous nebulae do not agree with the values determined in the Sun. For instance, several investigators have determined the Orion Nebula to be $\sim$2 less in metallicity than the Sun. Two explanations have been advanced to explain this potential discrepancy.

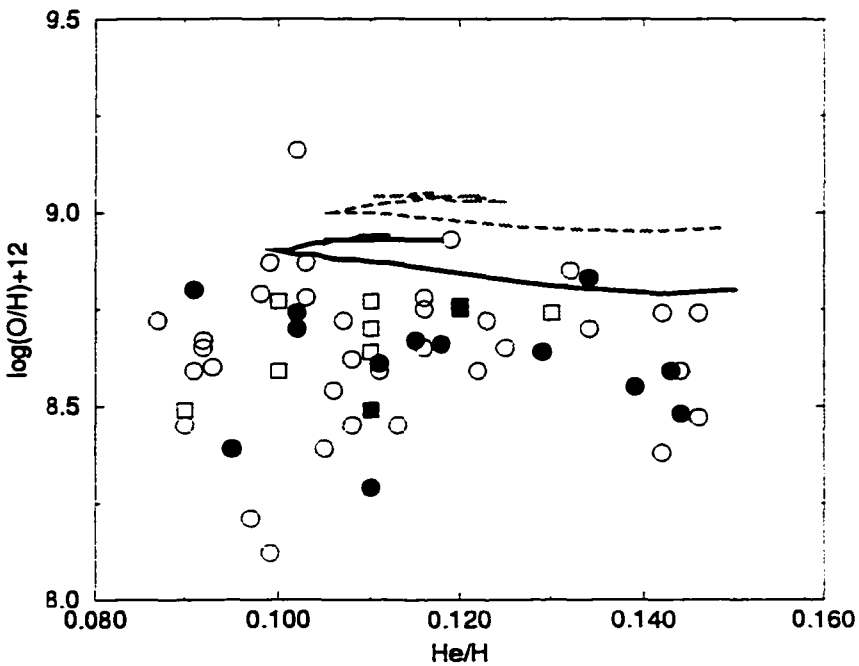

Figure 5.8: Galactic PNe plotted on the He/H-O/H plane. The symbols have the same meaning as in figure 5.4.

1. Strong temperature fluctuations exist (Peimbert 1967) which could reduce the apparent abundances by a factor of 2. Walter et al. (1992) accounted for temperature fluctuations and found the abundances of CNO in the Orion Nebulae matched those of the Sun; but when they did not invoke such fluctuations, the oxygen abundance was $0.45dex$ less.

2. The solar abundances are not representative of the typical interstellar medium. Snow and Witt (1996) make a good case for this possibility. Snow and Witt show the average abundances of B-stars and F and G stars are less than those found in the Sun. In particular, the average O abundance is 0.3dex less than in the Sun. Therefore it may not be necessary to invoke temperature fluctuations to explain the discrepancy.

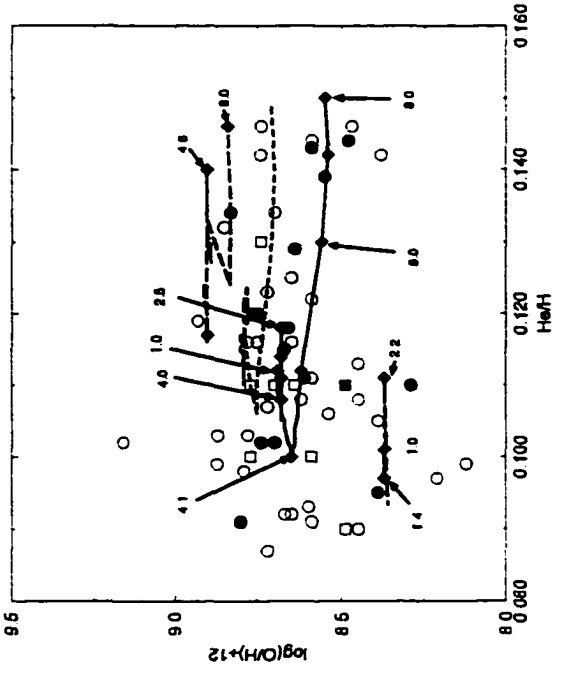

Figure 5.9: Same as figure 5.8 except the model curves have been shifted down by $0.25dex$ as indicated in the text.

Snow and Witt did not look into the average He abundance in the interstellar medium, although it is very important for determining PNe abundances. Kilian (1992) and Gies & Lambert (1992) investigated the He abundance in B-stars. Excluding a few exceptionally large helium abundances, the average He abundance of these samples is approximately solar while the average O abundance is reduced by a factor of $\sim$2. There may also be a real scatter in the initial He/H for any given O/H.

No resolution to the discrepancy shall be proposed here. However, corrections need to be made for it. Therefore, in figure 5.9 the model tracks have been shifted downward in log(O/H)+12 by $0.25dex$ in order to force agreement between data and models. In figure 5.9, we show the effect of the above shift. This is admittedly an ad hoc method, however, we feel it is reasonable given the possible discrepancies mentioned above.

Referring to figure 5.9, it can be seen that the high and low N/O objects both fit the expected pattern. We show in figure 5.9 the position in mass of the various models. Our models predict that the progenitors of $M \gtrsim 4.0 M_{\odot}$ should produce high N/O objects. Since the models from $\sim 4.5 M_{\odot}$-$\sim 8.0 M_{\odot}$ exhibit a slight downward slope on the He/H-log(O/H) plane, we expect the high N/O objects to exhibit a similar pattern and it appears to match the observations. However, the drop in O/H between 4.1 and 8.0 $M_{\odot}$ is less than $0.1 dex$, therefore it would be almost impossible to detect. Also, our models predict that for the low N/O, that the upper limit of He/H should be a function of O/H (also Ne/H and Ar/H). Examination of the PNe in figure 5.9 shows this to be true.

The same effect should be evident with other metallicity indicators. In figures 5.10 and 5.11, the low N/O PNe both seem to have a clear upper limit in He/H as a function of Ne/H and Ar/H, respectively.

Before we further examine figure 5.9, an examination of the metallicity of the high C/O PNe is in order. In figure 5.12, we have plotted C/O vs log(Ne/H) and a simple trend clearly jumps out, the high C/O (C/O>1) PNe tend lie between $12 + \log \mathrm{Ne/H}$ =8.0-8.2. This very narrow range in Ne/H suggests these objects all came from essentially the same metallicity progenitors. Also in figure 5.12 many of the high N/O objects lie in this same region, suggesting that both PNe with C/O>1 and PNe with N/O>0.5 come from the *same* narrow range of metallicity ($\sim 0.1 - 0.2 dex$).

The narrow metallicity range for high N/O and high C/O objects suggests that nearby objects with $M \gtrsim 2.0 M_{\odot}$ come from progenitors with a range in metallicity of $\sim$0.1-0.2dex. Our models and those of several other investigators (Bazan 1991, Boothroyd and Sackmann 1988abcd, Boothroyd and Sackmann 1992, Boothroyd et al.1993, Busso et al.1992, Busso et al.1995, Forestini and Charbonnel 1996, Groenewegen and deJong 1993, Groenewegen and deJong 1995, Marigo et al.1996, Lattanzio 1986 , Vassiliadis and Wood 1993) suggest that the minimum mass for

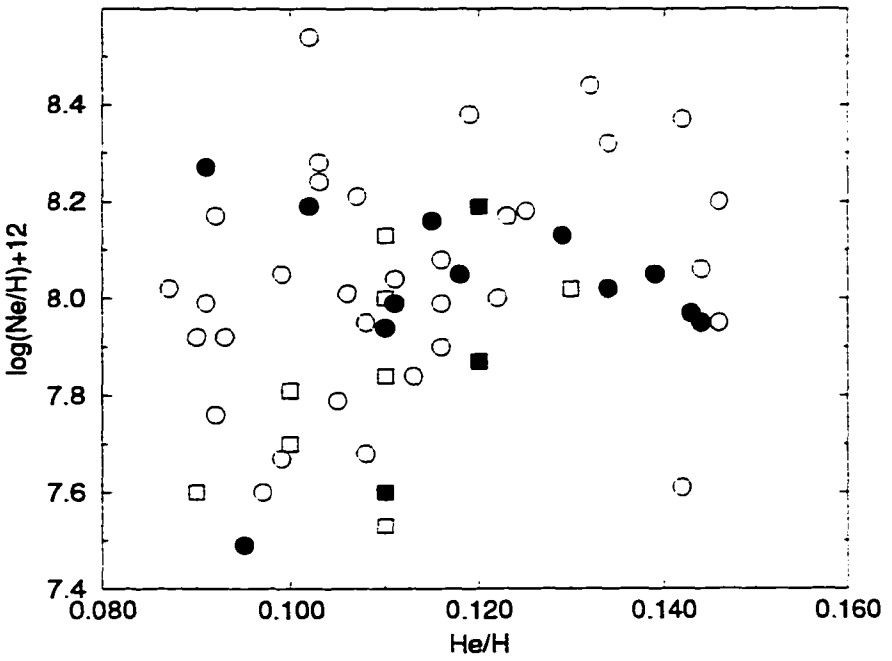

Figure 5.10: Comparison of He/H vs Ne/H. The low and high N/O PNe are indicated by open and closed circles, respectively. Note that the maximum He/H for low N/O objects increases with Ne/H.

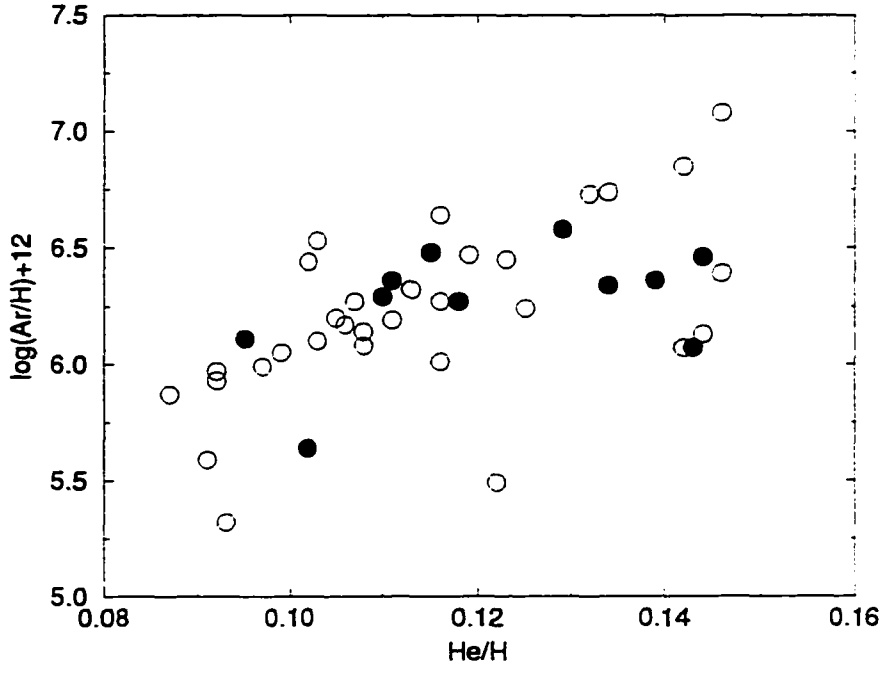

Figure 5.11: The symbols have the same meaning as in figure 5.10. Note the maximum He/H for low N/O objects increases with Ar/H.

carbon star formation, $M_{CS} \gtrsim 1.5M_{\odot}$ and for the formation of nitrogen rich stars via hot-bottom burning, $M_{hbb} \gtrsim 4.0M_{\odot}$. Models by Schaller et al. (1992) suggest that a $1.5M_{\odot}$ star requires 1.8-2.6Gyrs to reach the He core flash depending upon metallicity. This can be regarded as the lower limit to the age of the high N/O and high C/O objects.

Since all of these objects appear to come from such a narrow range in metallicity, this range may indicate an upper limit to the enhancement of the local interstellar medium. The limited range of lifetimes available to progenitors with $M_{ZAMS} \gtrsim 1.5 - 2.0M_{\odot}$ and the narrow metallicity range combined suggest the placement of limits on the rate of enhancement of the interstellar medium with

$$\frac{\Delta \log O/H}{dt} < 0.11 dex \cdot Gyr^{-1}. \tag{5.1}$$

This appears to contradict the results of Edvardsson et al. (1993), who claim that there is no unique age-metallicity relationship. They showed in their paper that at any given age a large spread of metallicities exists. However, the sample of high C/O and high N/O objects probably is not from the same population as their G and F stars. The probable mass of the PNe progenitors indicates that on the main sequence, they were probably A and B stars. Therefore, since the samples are different, there is no contradiction.

The difference in the metallicity spreads between our sample and the sample of Edvardsson et al.(1993) may point to why their sample has an age-metallicity degeneracy. If stars with $M \gtrsim 2.0M_{\odot}$ come from a narrow range of metallicities and those with $M \lesssim 2.0M_{\odot}$ come from a wide range, some process must cause stars that are degenerate in age and [Fe/H] to appear in the solar neighborhood. It is reasonable to suppose that the initial metallicity is a function of the time and place of birth, which can be expressed as:

$$[Fe/H] = f(R, t). \tag{5.2}$$

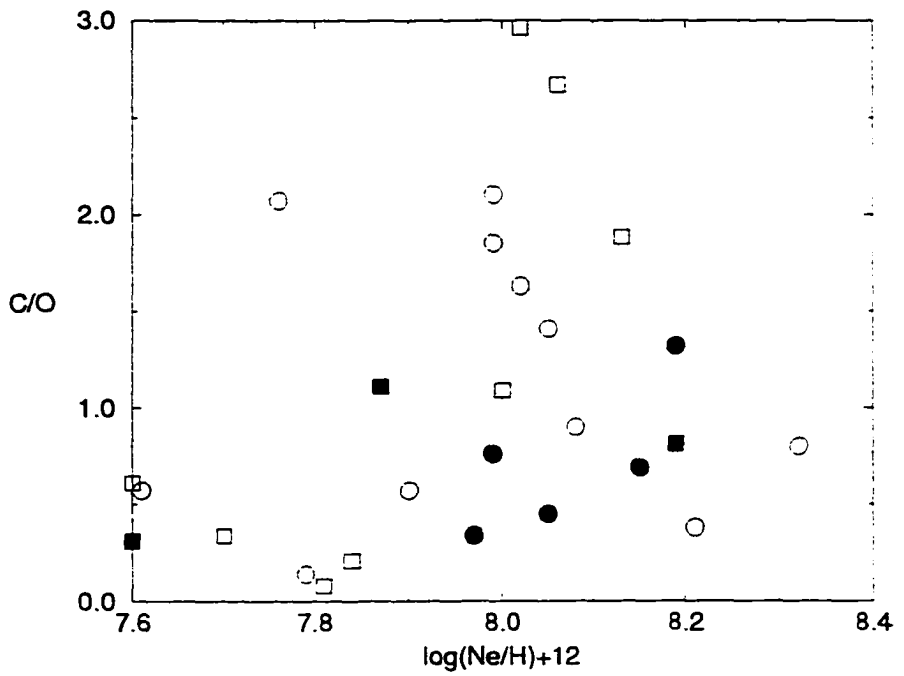

Figure 5.12: Galactic PNe plotted on the C/O-Ne/H plane. The symbols have the same meaning they do in figure 5.4. Note the narrow range in Ne/H of PNe with C/O>1.0.

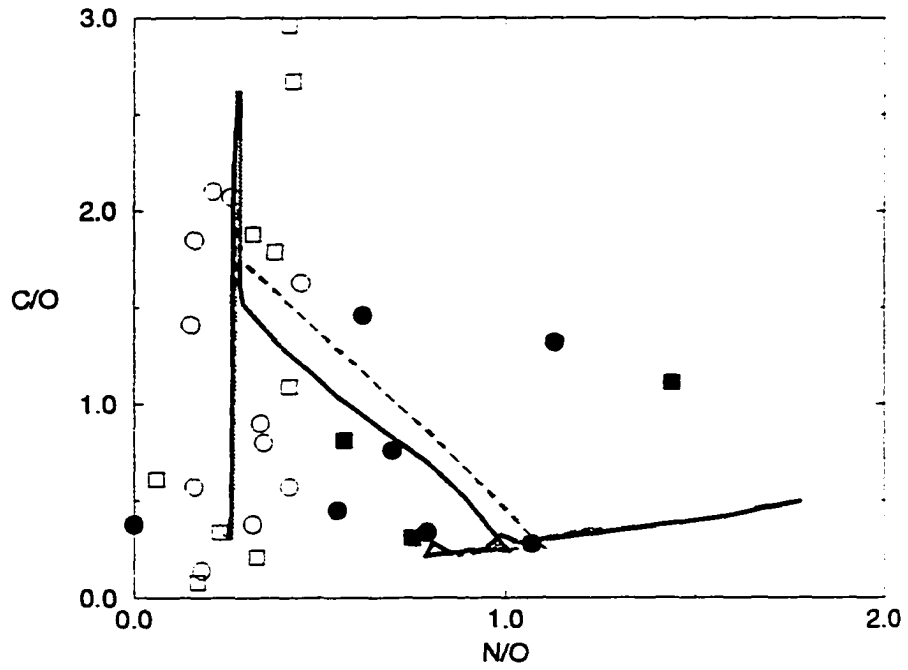

Figure 5.13: Comparison of models to data on the C/O to N/O plane.

However, as stars get older they are less likely to be found near their point of origin. A possible explanation of the trend in F and G stars is that they originated at many different positions in the Galaxy with different [Fe/H]'s and migrated to the stellar neighborhood. The reason the high N/O and high C/O PNe do not show this trend is because there is not sufficient time for the migration to occur. Note that the low C/O-low N/O PNe do show a very wide range in O/H, Ne/H, and Ar/H which is consistent with the stars of the Edvardsson sample.

5.3.3 Other Diagrams

Hot-bottom burning converts carbon to nitrogen, so when N/O is high C/O should be low and vice-versa. Figure 5.13 compares the models to the data on the N/O-C/O plane. The agreement between models and data is reasonably quantitative. C/O and N/O are related as suggested above.

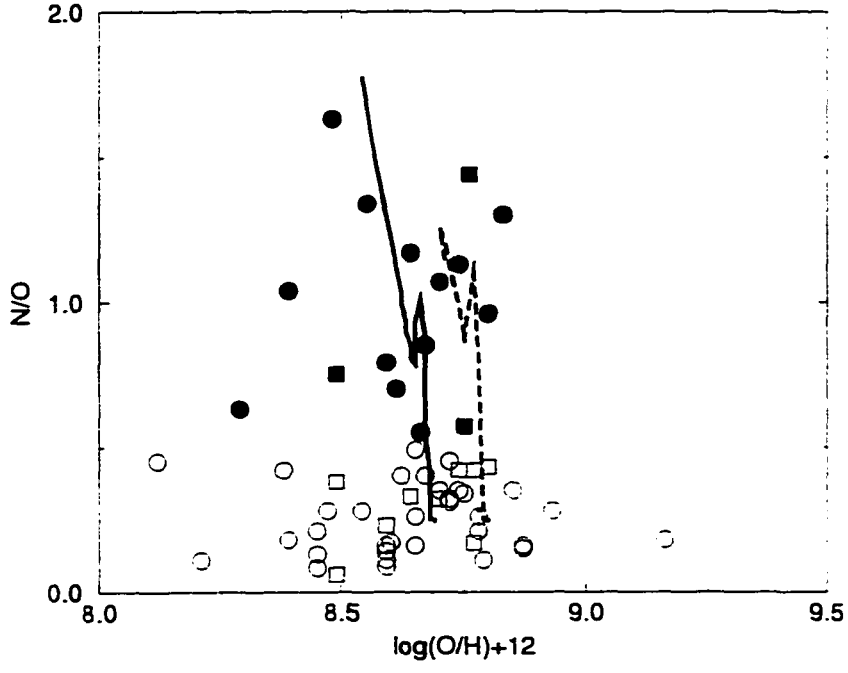

Figure 5.14:

An often used method to look for ON cycling is to plot PNe on the O/H-N/O plane and to look for an anticorrelation between the two quantities. Figure 5.14 shows that our models can fit the data. At high N/O, our models show a slight drop in O/H. However, the magnitude is very small at near solar metallicities, therefore, any anticorrelation that might exist is weak.

5.4 Summary

We have found that our models match the observed features of PNe abundance ratio data. In particular:

1. We have found examples of helium being produced by both the second and third dredge-up. In high N/O PNe, the helium is produced by the second dredge-up. In low N/O-high He/H PNe, helium is produced via the third dredge-up.

2. Nitrogen is produced via the first dredge-up and via a combination of second dredge-up and hot-bottom burning. In high N/O PNe, some of the N/O comes from the second dredge and then hot-bottom burning converts the remaining C to N. There is evidence of first dredge-up in low N/O PNe.

3. Carbon is produced in low-mass stars and is destroyed in intermediate mass stars. In low-mass stars carbon that is dredged-up is not destroyed via hot-bottom burning while in intermediate mass stars it is.

4. For low N/O PNe, the maximum possible He/H is controlled by the metallicity.

5. We can match very closely the maximum N/O and C/O seen in PNe.

We find that to match all the PNe data, a large range of metallicity progenitors are necessary. This is consistent with stellar abundances. However, to match PNe with high C/O (>1) or high N/O (>0.5) a very narrow range of metallicity progenitors are necessary.

5.5 Discussion

Overall, our models with hot-bottom burning and dredge-up do a good job of matching the PNe abundances. We can duplicate the high C/O and N/O ratios seen in many PNe. The models also predict how He/H should behave.

5.5.1 Correlations with Mass and Core-Mass

An interesting possibility is using the abundances of PNe to get a rough idea of both their core-mass and the progenitor masses. The two masses are not unrelated. Weidemann and Koester (1987) have shown a relation exists between the ZAMS mass and the mass of the resulting white dwarf, a so called initial-final relation ($M_i - M_f$). Some observational efforts have been made along these lines (Ratag

1991, Kaler and Jacoby 1990, Kaler et al.1989) who attempted successfully to correlate N/O with core-mass.

Can He/H be used to determine the mass of PNe? Clearly, there is no unique relation between He/H and mass. Our models do a reasonable job of fitting the data and predict that He/H rises with mass between $\sim$1.5$M_\odot$ and $\sim$2.5$M_\odot$, but between $\sim$2.5$M_\odot$ and $\sim$4.5$M_\odot$ He/H is anticorrelated with mass. Above 4.5$M_\odot$, He/H again rises. However, it maybe possible using N/O and He/H in conjunction to determine the mass. For high N/O PNe (N/O$\gtrsim$0.8), figure 5.4 shows that He/H is a function of progenitor mass. For high N/O PNe, N/O and He/H are correlated. Therefore, it should be in principle possible to get a rough idea of progenitor mass from He/H for high N/O PNe. More work needs to be done on the second dredge-up before predictions are made as to the actual mass of the high N/O progenitors. Also, we predict that the core-masses of PNe with N/O>0.8 will be correlated with He/H.

For the low N/O PNe, the use of He/H to determine mass is probably impossible. There is a "degeneracy" in mass for He/H, in the sense that a different mass model for each [Fe/H] will give the same He/H. In principle, a plot of He/H vs Z/H where Z is O, Ne, S, or Ar overlayed with a grid showing the masses could be used to determine masses. However, the errors in the abundances are such that it is probably impossible to accomplish this with any confidence. On the other hand, C/O could probably be used as a rough mass indicator for the low N/O PNe. The ratio of C/O seems to vary with mass and also core-mass.

5.5.2 Hot-bottom Burning

There is some debate as to whether the enhancements of nitrogen seen in PNe are due to the CN cycle, the ON cycle, or a combination of both.

The CN cycle is clearly in operation. Peimbert (1973) was the first to show that N/O is much greater than the typical HII region values. Many abundance

studies (Henry 1990. Kingsburgh and Barlow 1994. Leisy and Dennefeld 1996)have demonstrated convincingly that ^{12}C has been converted into ^{14}N by the PN progenitors.

Must hot-bottom burning occur to produce the high N/O ratios? For instance. the second dredge-up can produce nitrogen. However, figure 4.3 suggests that N/O at the end of the second dredge does not match the highest N/O PNe. Kingsburgh and Barlow (1994) suggested the maximum N/O from first and second dredge-up is 0.8. They reasoned that the first two dredge-ups can only convert carbon initially present in the star and by converting all the carbon to nitrogen they get 0.8. We suggest that a more realistic limit based on our calculation of first and second dredge-ups is $\approx$0.6. Clearly, several PNe have N/O larger than this. and the only other source is hot-bottom burning converting carbon to nitrogen.

More questions revolve around the operation of the ON cycle. Some investigators (Dufour 1991. Henry 1990. Perinotto 1991) have argued that the ON cycle must occur because they detected an anti-correlation between O/H and N/O. Other investigators (Kingsburgh and Barlow 1994) have argued against it claiming the O/H-N/O anticorrelation is not significant. Kingsburgh and Barlow also argue that there should be an anticorrelation between O/H and He/H which they do not observe.

Our results suggest however that for Galactic PNe. that ON cycling can occur and still bring into agreement the results of the many investigators.

1. The predicted amount of ON cycling will only lead to a small reduction of O/H by 0.1-0.2*dex*. Since this is comparable to the errors. any existing anticorrelation between O/H and N/O should be weak. This explains both the weak detections and the no detections.

2. Our comparison of models and data predict that the behavior of He/H as a function of mass is more complicated than previously assumed. In other

words He/H and O/H are probably not correlated. A more subtle test is to look for a correlation between He/H and O/H for PNe with N/O>0.8 which our models do predict. This correlation maybe detectable but it will be very weak.

Our models suggest that things that have been taken as evidence both for and against ON cycling are not conclusive due to the weakness of the correlations. On the other hand, the weakness of the correlations means that the case for ON cycling is still open.

Since our models fit on the plots of O/H versus N/O and O/H versus He/H and the difference between model ZAMS O/H and PNe O/H is $0.1dex$. we feel that this represents an upper limit to the O/H depletion.

In contrast, the models of Renzini and Voli (1981) suggest that O/H can be reduced by as much as $0.3dex$ or a factor of 2 which should be detectable with large samples. The difference is due to the time the models undergo hot-bottom burning. In our models, which acheive higher base temperatures than those of Renzini and Voli, the hot-bottom burning epoch approximately lasts one-tenth as long as comparable Renzini and Voli models. Therefore, their models burn more oxygen to nitrogen. Since O/H reductions of this magnitude are not seen, we feel our models better fit the observed data.

5.6 Comparison to Other Models

Our models mostly agree with the recent ones of Groenewegen and deJong (1993, 1994) and Marigo et al. (1996). These two other models indicate that the minimum mass model for hot-bottom burning is approximately $4M_{\odot}$, which agrees with our result. Our models indicate PNe with low and intermediate mass progenitors will be C-rich and N-rich, which agrees with their result.

Our models give somewhat different results in some areas than those of Groe-

newegen and deJong (1993, 1994) and Marigo (1996).

1. Our intermediate mass star models reach do not reach as high N/O ratios as either of these other models. This is due to our choice of third dredge-up model. They use a constant dredge-up parameter, λ, while ours is related to mass. For intermediate mass stars they use a λ which fits the LMC carbon star luminosity function. However, the progenitors of carbon stars are probably low-mass stars. A typical λ for our intermediate mass stars is 0.4 while they use 0.6.

2. We do not reach as high C/O ratios as they do. Both Marigo and Groenewegen and deJong achieve maximum C/O ratios greater than 5, while ours are only 3. C/O calculated from the CIII]λ1909 line is superior to that from the optical line (Rola and Stasinska 1994). Both groups however use C/O determinations using the optical carbon line which gives misleading results. Therefore, we feel that we have acheived a better fit to this important element.

Chapter 6

On the Origin of Planetary Nebula K648 in Globular Cluster M15

6.1 Introduction

The globular cluster M15 contains the well studied planetary nebula (PN) K648. This is one of the few galactic PNe with a reasonably well-determined distance. Therefore, fundamental properties such as the stellar luminosity can be determined with some confidence. Because of its globular cluster membership, many of the progenitor properties, such as the zero age main sequence (ZAMS) mass, can be inferred reliably.

Due to the importance of K648 as a halo PN, it has been the focus of several abundance studies, and all of these show the abundances of most metals to be depleted relative to the sun, consistent with a progenitor of low metallicity. Carbon is an exception; studies which determine the ratio (by number) of C/O in K648 infer values that range from $4-11$ (Adams et al. 1984; Henry, Kwitter, and Howard 1996; Howard, Henry, and McCartney 1997), which is far above C/O in the Sun of 0.43 (Anders and Grevesse 1989, hereafter AG89). This is in fact much higher than the average C/O ratio of ≈ 0.8 for solar neighborhood PNe (Rola and Stasińska 1994).

Low and intermediate mass stars that have left the main sequence, ascended the giant branch, and passed through the horizontal branch. then enter a thermally unstable phase where energy is generated by shell He and H-burning called the thermally pulsing asymtoptic giant branch (TP-AGB) stage, which is a very important yet not well understood phase [Detailed reviews of this stage can be found in Iben (1995), Lattanzio (1993), and Iben and Renzini (1983)]. During the TP-AGB stage the star alternates between a long stage where the luminosity is generated mostly by quiescent hydrogen shell burning, with a helium burning layer producing a minority of the energy, and a thermal runaway stage in the unstable helium burning layer (Schwarzschild and Härm 1965, 1967; and Weigert 1966). The second stage results in expansion of the outer layers and an extinguishing of the H burning shell. This short stage, characterized by rapid changes, with helium burning dominating the energy generation, is known as a thermal pulse or a He shell flash.

TP-AGB stars exhibit large mass-loss rates ranging from 10^{-7}–10^{-4} $M_\odot$ yr^{-1} . Indeed such high mass-loss rates are predicted to result in the ejection of the envelope, at which point the star leaves the AGB and becomes a planetary nebula central star (CSPN). The first models of CSPN tracks were made by Paczynski (1971) who showed that the CSPNs evolve horizontally on the HR diagram when nuclear burning is still taking place and then as they cool the luminosity and temperature decrease. Härm and Schwarzschild (1975) showed that a CSPN could leave the AGB as either a helium burning or hydrogen burning star. The observational consequences of hydrogen and helium burning have been studied in the more refined models including mass loss showed that the subsequent evolution of the central star depends on whether or not the star leaves the AGB as a helium or hydrogen burner [Schönberner (1981, 1983) and Iben (1984)].

Low mass stars ($M \lesssim 3$ $M_\odot$) can experience two mixing episodes or "dredge-ups". During dredge-up, material that has been processed by nuclear burning is

mixed into the surface layers. At the entrance to the giant branch, the convective region can extend into the core, leading to mixing of CNO products into the outer layers. Similarly as shown by Iben (1975), after a thermal pulse on the AGB, the convective region can extend into the core, mixing He-burning products into the outer layers. These two mixing events are known as first and third dredge up, respectively (second dredge up will not concern us here). Therefore, a third dredge-up is a natural explanation of the high carbon abundance found in K648. On the other hand, no carbon stars have been observed either in M15 or in any other globular cluster, although such stars should be the immediate progenitors of objects such as K648 if a third dredge-up occurs. Thus, the lack of carbon stars in M15 weakens the argument for a third dredge-up event.

One possible explanation for the absence of carbon stars is a delayed scenario in which the third dredge-up of carbon rich material changes the structure of the envelope during the following interpulse phase, ultimately increasing the mass-loss rate significantly and driving off the stellar envelope (Iben 1995). Thus envelope ejection is delayed until the interpulse phase following this dredge-up of carbon rich material.

Another explanation supposes that the envelope is removed during the quiescent He-burning stage that follows a thermal pulse (Renzini 1989 and Renzini and Fuci-Pecci 1988). The carbon then originates in a fast wind from the central star (CSPN). In addition, the wind produces shock-heating in the nebula, which, if not properly accounted for during an abundance analysis, may lead to the inference of a spuriously high C/O ratio. In this case the envelope would be ejected immediately after a thermal pulse while helium shell burning still dominates the luminosity. We refer to this mechanism as the prompt scenario.

In this paper we calculate detailed envelope models of thermally pulsing asymptotic giant branch star envelopes to test the predictions of the delayed mechanism, perform other calculations relevant to the prompt mechanism, and compare output

of each with observations of K648. Section 2 describes the envelope code, section 3 presents the observational data and the results for the delayed and prompt models, and a brief discussion of our findings is given in section 4.

6.2 Models

The computer code used to calculate the delayed models is a significantly updated and modified version of a program kindly provided to us by A. Renzini for modeling the envelope of TP-AGB stars during the interpulse phase. Many of the basic details of the method are enumerated in Iben and Truran (1978) and Renzini and Voli (1981) and references therein; in this section we concentrate on those features which are different. In a future paper (Buell et al. 1997) we will provide a more detailed description of the code.

The mass of the hydrogen exhausted core (M_H) at the first thermal pulse is given by the expression found in Lattanzio (1986). During each interpulse phase the code follows the mass of the hydrogen exhausted core and envelope, the evolution of envelope abundances of ^4He, ^{12}C, ^{13}C, ^{14}N, and ^{16}O, and determines $T_{\rm eff}$ by integrating the equations of stellar structure from the surface to the core. Envelope abundances at the first pulse are determined by combining published main sequence levels with changes due to the first dredge-up. The former are established by scaling the AG89 solar abundances of all metals except the alpha elements, i.e. oxygen, neon, and magnesium, to the appropriate metallicity, and then setting $[N_\alpha/Fe] = 0.4$, where N_α is the number abundance of O, Ne, and Mg. This last value is chosen from an examination of the trends in the data of Edvardsson et al. (1993) for [Fe/H]<-1.0 and by assuming that neon and oxygen vary in lockstep in PNe as shown by Henry (1989). The abundance changes due to the first dredge-up are calculated from the formulae of Groenewegen and deJong (1993).

The mass-loss both before and during the TP-AGB phase is very important, although the parameters are poorly understood. The pre-TP-AGB mass-loss is a

free parameter, while during the TP-AGB phase, mass-loss is determined by using the expression of Vassiliadis and Wood (1993), which can be written as

$$\log \dot{M} = -11.43 + 1.0467 \times 10^{-4} \left(\frac{R}{R_\odot}\right)^{1.94} \left(\frac{M}{M_\odot}\right)^{-0.9} \quad \mathrm{M_\odot\ yr^{-1}}. \qquad (6.1)$$

The above rate is used until $\log \dot{M} = -4.5$, and then it is held fixed. Equation 1 is a $\dot{M}$ – Period relation based on mass-loss from population I stars. However, recent calculations by Wilson, Bowen, and Struck (1995) suggest that the mass-loss rates of low metallicity AGB stars are also strongly dependent on radius. There is considerable uncertainty in this equation. For example, predicted mass-loss rates from other equations with a similar form (e.g. Bazan 1991) differ from predictions of eq. (1) by up to a factor of five.

The luminosity of TP-AGB stars after the first few pulses can be described by a linear relation between core-mass and luminosity as first discovered by Paczynski (1970). Models of TP-AGB stars have shown that for $M \lesssim 3.0\mathrm{M_\odot}$ this relation depends on metallicity (Lattanzio 1986, Hollowell and Iben 1988, Boothroyd and Sackmann 1988b). At the first pulse the luminosity of TP-AGB stars is less than the asymptotic core-mass-luminosity relation. The luminosity at the first pulse in our models is found by linearly extrapolating in metallicity from the expressions found in Boothroyd and Sackmann (1988b). After the first pulse, the luminosity of the AGB star rises steeply until it reaches a value predicted by the core-mass luminosity relation (CML) of Boothroyd and Sackmann (1988b). This relation predicts luminosity primarily as a function of core mass, although it has a weak dependence on helium and metal mass fractions.

Carbon rich material can be dredged from the core into the envelope following a thermal pulse. We assume that when the mass of the hydrogen-exhausted core exceeds a minimum mass ($\mathrm{M^{DU}_{min}}$) that a dredge-up occurs. The amount of material dredged up, $\Delta \mathrm{M_{dredge}}$, is determined by the free parameter λ, where

$$\lambda = \frac{\Delta \mathrm{M_{dredge}}}{\Delta M_c}. \qquad (6.2)$$

Parameter	Value	ref.
T_{eff}	36000 ± 4000 K	1,2
d	10.0 ± 0.8 kpc	3
θ	$1.0 - 2.5$arcsec	1,2,5
v_{exp}	$15 - 25$ km s^{-1}	
n_e	$1700 - 8000$ cm^{-3}	1,2
T_e	12000 K	1,2
$\log F_{H\beta}$	-12.10 ± 0.03	4

Table 6.1: Observational Data for K648: This table is a summary of the observed and inferred parameters for PN K648. The effective temperature, T_{eff}, refers to the central star, while the distance, d, is the adopted distance to K648. The following nebular parameters are also listed: the angular size of the nebula, θ; the expansion velocity, v_{exp}; the electron density, n_e; the ionized gas temperature, T_e; and the log of the measured Hβ flux in erg cm^{-2} s^{-1}. The large range in θ and n_e arise from differences between newer HST data and ground based data, The HST data give higher a value of θ and a lower value for n_e. The references are as follows: (1) Adams et al. 1984; (2) Bianchi et al. 1995; (3) Durell and Harris 1993; (4) Acker et al. 1992; (5) Gathier et al. 1983

In eq. (2) ΔM_c is the amount of core advance during the preceding interpulse phase. We determine the composition of the dredged up material from the formulas in Renzini and Voli (1981), with $^4He \approx 0.75$, $^{12}C \approx 0.23$, and $^{16}O \approx 0.01$ as the approximate mass fractions.

Finally, the code uses the opacities of Rogers and Iglesias (1992) supplemented by the low temperature opacities of Alexander and Ferguson (1994).

6.3 Results and Discussion

6.3.1 Observational Parameters

Numerous observed and inferred parameters for K648 are listed in tables 6.1 and 6.2, where the symbols in column (1) are explained in the table notes. We comment here on the method of determination for several of them.

Radio images of K648 have been made by Gathier et al. (1983) and optical images were made by Adams et al. (1984), and recently by Bianchi et al. (1995) using the HST. The HST data called into question the small size for the nebula

inferred in the radio studies of Gathier et al. (1983) and the optical studies of Adams et al. (1984), since HST was able to resolve the structure of the nebula. This leads to, e.g., a larger planetary mass and smaller electron density. In Tables 6.1 and 6.2, we quote all results.

M_{PN} was computed using equation V-7 in Pottasch (1984), while the dynamical age was estimated by dividing the nebular radius by the expansion velocity (v_{exp}). Since no v_{exp} is available for K648 we use a range which represents typical values for PNe. The central star mass for K648 was estimated by linearly interpolating/extrapolating using both hydrogen burning and helium burning post-AGB tracks of Vassiliadis and Wood (1994) in the log L-log T plane. The metallicity of M15 suggests using a low Z track, although the carbon abundance of K648, if correct, would increase the metallicity of the star, suggesting that a higher Z track is more appropriate. Since the metallicity dependence is unclear, we estimated the range of possible central star masses by performing the interpolation for each metallicity considered by Vassiliadis and Wood. Thus, the mass range of the central star is 0.55–0.58$M_{\odot}$ for the H burning tracks and 0.56–0.61$M_{\odot}$ for the He-burning tracks. We adopt a final core mass of $0.58 \pm 0.03 M_{\odot}$.

The theoretical age of the central star was estimated from the figures of Vassiliadis and Wood and linearly interpolating in log L between tracks which closely match the core mass of K648, e.g., the hydrogen burning M_c=0.56, Z=0.016 track and the helium burning M_c=0.56 $M_{\odot}$, Z=0.004 give evolutionary ages of $\sim$ 12000 yr and $\sim$1800 yr, respectively. Other tracks with $M_c \lesssim 0.6 M_{\odot}$ and different metallicities give similar results. When compared to the dynamical age a He burning track is favored.

The adopted abundances of K648 for He/H, C/O, and N/O ratios represent a range of recent literature values. Howard et al. (1997) find that in six of the nine halo PNe they studied, the C/O ratio exceeds the solar value. Many of these nebulae have stellar temperatures much higher than that of K648, implying that

Parameter	Observed Value	ref.	Delayed Scenario	Prompt Scenario
L	$3200 - 4700\ L_{\odot}$	1,2	4600	4000
M_{PN}	$0.015 - 0.090 M_{\odot}$	1,2	$0.048 \pm 0.012 M_{\odot}$	$0.064 M_{\odot}$
M_c	0.58 ± 0.03		0.57 ± 0.01	0.58
τ_{dyn}	$2000 - 8000$ yr		12000 yr	1800 yr
He/H	$0.083 - 0.10$	1,3,4	$0.087 - 0.091$	0.9
C/O	$4 - 11$	1,3,4	$4 - 25$	4
N/O	$0.05 - 0.20$	1,3,4	$0.17 - 0.19$	0.17

Table 6.2: Observational Data and Models Compared: This table compares the observed and predicted parameters for PN K648. The observed luminosity, L, refers to the central star, while the predicted luminosity is the luminosity on the AGB, but since the tracks are nearly horizontal they should be comparable. The following nebular parameters are also listed: the mass of ionized gas in the nebula, M_{PN}; the mass of the central star, M_c; the dynamic timescale, τ_{dyn}; and the abundance ratios He/H, C/O, and N/O by number. The abundances for the prompt scenario are calculated assuming 0.00014 $M_{\odot}$ of helium and carbon rich material is removed by mass-loss from the CSPN. The observed value for the dynamical timescale, τ_{dyn}, corresponds to an upper limit for the age of the nebula. The theoretical values correspond to evolutionary time scales required to reach a given central star temperature. The large range in L and M_{PN} arise from differences between HST data and ground based radio and optical data. The HST data give higher values for L and M_{PN}. References: (1) Adams et al. 1984; (2) Bianchi et al. 1995; (3) Henry, Kwitter, and Howard 1996; (4) Howard, Henry, and McCartney 1997

they are older and more evolved. Since the high C/O ratios persist into the later stages of PN evolution, this suggests that the inferred C/O is not influenced by the presence of shock heating in the nebula.

The mass-loss rate at the tip of the AGB was determined by dividing the nebular mass by the dynamical age. This is in reality a lower limit since it assumes that the nebula has a filling factor of 1, which is unrealistic. By this procedure we calculate that the lower limit to the mass-loss is 9×10^{-6} $M_\odot$ yr^{-1}. The upper limit is assumed to be 10^{-4} $M_\odot$ yr^{-1}.

The composition of the central star is uncertain, as two recent papers do not agree. McCarthey et al.(1996) find that the central star has a normal helium abundance, whereas Heber et al.(1993) find that the central star is helium and carbon rich.

6.3.2 Delayed Scenario

We have calculated several low mass, low metallicity models, but here we focus on the two models listed in table 6.3, where we present the model input parameters: the ZAMS mass (M), the core mass at PN ejection (M_c), the mass of the PN (M_{PN}), the ZAMS [Fe/H] ratio, the adopted ratio of the mixing length to pressure scale height (α), the mass of the model star at the first thermal pulse (M_{FTP}), the adopted dredge-up parameter (λ), and the minimum core mass for dredge-up ($M^{DU}_{c,min}$). The panels of Figure 6.1 show the evolution of the interpulse luminosity, the stellar radius, the mass-loss rate, and the core mass as a function of total mass. All quantities are expressed in solar units. Figure 6.2 shows the evolution of the chemical composition of the envelope as a function of total mass. Table 6.2 compares the observed quantities to our predicted ones.

We note in figure 6.1 that the interpulse radius of each model star increases dramatically after the final pulse, as compared to the preceding interpulse phase. The increase in radius leads to a large increase in the mass-loss rate in each model

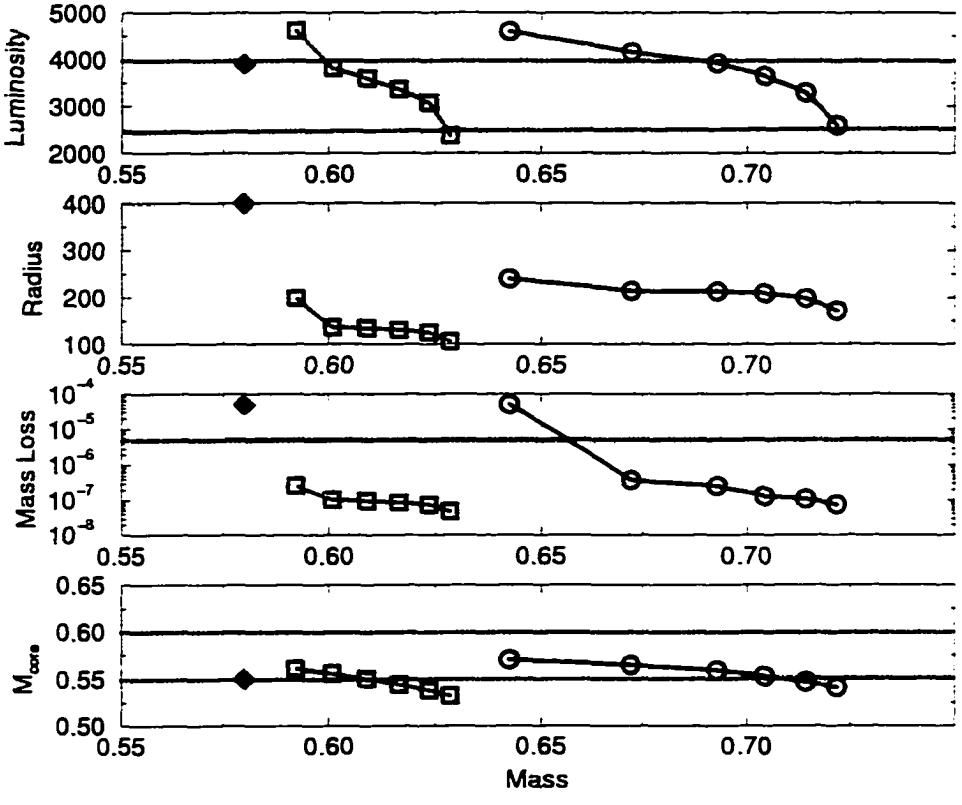

Figure 6.1: Shown in the panels of this figure are the evolution of our thermally pulsing AGB models and the parameters of our prompt model. The dotted line and open squares track model 1, the solid line and open circles track model 2, and the solid diamonds are the parameters of the prompt model. The abscissa of the graphs tracks the mass of the models in solar masses. Due to mass loss the stars move from right to left on the graphs. The parameters in the panels are for the interpulse phase. From top to bottom the parameters are stellar luminosity (in $L_\odot$), radius (in $R_\odot$), the mass-loss rate (in $M_\odot$ yr^{-1}), and the mass of the core. The observed upper and lower limits of the AGB tip luminosity are indicated with dark long dashed lines, the lower limit on the AGB tip mass-loss rate is indicated with a long dashed line, and the upper and lower limits of the central star mass are indicated with long dashed lines.

No.	M	M_c	M_{PN}	[Fe/H]	α	M_{FTP}	λ	$M^{DU}_{c,min}$
1	0.88	0.56	0.037	-2.1	1.6	0.62	0.10	0.55
2	0.85	0.58	0.060	-2.1	0.8	0.72	0.02	0.56

Table 6.3: Input Parameters and Results for Delayed Models: Note, the masses are in $M_\odot$

during the final interpulse phase: the mass-loss rate increases by almost a factor of 100 in model 2 and by a factor of 5 in model 1. This is a consequence of the steep dependence of our mass-loss law on the stellar radius. The significant increase in the mass-loss rate causes the star to lose its envelope in a few thousand years. The mass-loss rate for model 1 is clearly too small relative to the observationally derived value. However, we have found that by reducing the mixing length (α) by a factor of two, as we have done in model 2, we can make a model that essentially reproduces the observed AGB tip mass loss rate.

The significant event that occurs during the final pulse is a dredge-up of helium and carbon rich material. The mass of material dredged up is a few times $10^{-5} M_\odot$. However, given the mass of the envelope and the low initial abundances, the amount of carbon dredged into the envelope is significant enough to increase the carbon mass fraction by a large factor in each case. Consequently, the envelope opacity rises, causing a dramatic increase in the stellar radius.

The envelope of each model at the last thermal pulse is only a few times $10^{-2} M_\odot$ and, after the final carbon dredging pulse, is ejected on a timescale of a few hundred years. Each model star is a carbon star for only a few hundred years, due to the rapid mass-loss after a dredge-up of carbon. This short lifetime, coupled with the relatively low incidence of PNe in globular clusters [two confirmed and three possible candidates (Jacoby et al. 1995)], perhaps explains why carbon stars have not been observed in globular clusters.

An important check on our models is to compare the predicted AGB tip luminosity with its observed value. The predicted luminosity of our models at the top of the AGB agrees fairly well with the tip of M15's red giant branch (Adams et

al. 1984). Our models suggest that the observed AGB tip will actually correspond to the second-to-last pulse, since after the dredge-up event the star is predicted to remain as an AGB star for only ~1000 yr. The luminosity of K648 in Adams et al. (1984) appears to be 0.1dex higher than the tip of the giant branch, this may be due to the metallicity enhancement due to the dredge up. As noted earlier, the core-mass luminosity relationship depends on metallicity, with the luminosity at a set core-mass increasing with increasing metallicity. If we lower the luminosity still further to $\sim 2000 L_{\odot}$ to match the tip of the giant branch, we believe that the addition of carbon to the envelope will still cause envelope ejection.

There is some question about whether or not dredge-up can occur at the low values of $M_{c,min}^{DU}$ indicated by our models (see table 6.3). While Lattanzio (1989) found that dredge-up can occur at a core mass above $0.605 M_{\odot}$, the same study also found a dependence of the minimum dredge-up mass on metallicity, with lower metallicities giving lower mass dredge-ups. Boothroyd and Sackmann (1988c) found that if they increased the mixing length parameter α from 1 to 3, they were able to cause a dredge-up in a model with Z=0.001, $M_c = 0.566 M_{\odot}$, and $M = 0.81 M_{\odot}$, although it is unclear if a mixing length this large is justified. Additionally, to match the low luminosity end of the carbon star luminosity function of the LMC, Groenewegen and deJong (1993) had to set $M_{min}^{DU} = 0.58 M_{\odot}$. From these studies it appears that our values for $M_{c,min}^{DU}$ are not unreasonable.

Finally, we point out that each of the delayed models gives a very natural explanation of the high carbon abundance of K648 and the lack of carbon stars. Each model also predicts the observed mass of the ionized gas to be a few times $10^{-2} M_{\odot}$. The C/O ratios of each model range from 4 to 25, with model 2 giving the best fit, which agrees reasonably well with the observed values of $4 - 11$. The He/H ratios of the model stars also agree with the observed value of 0.09. The high N/O ratio inferred in the models may be an artifact of our choice of initial O abundance and hence could be reduced with a higher O abundance, which would

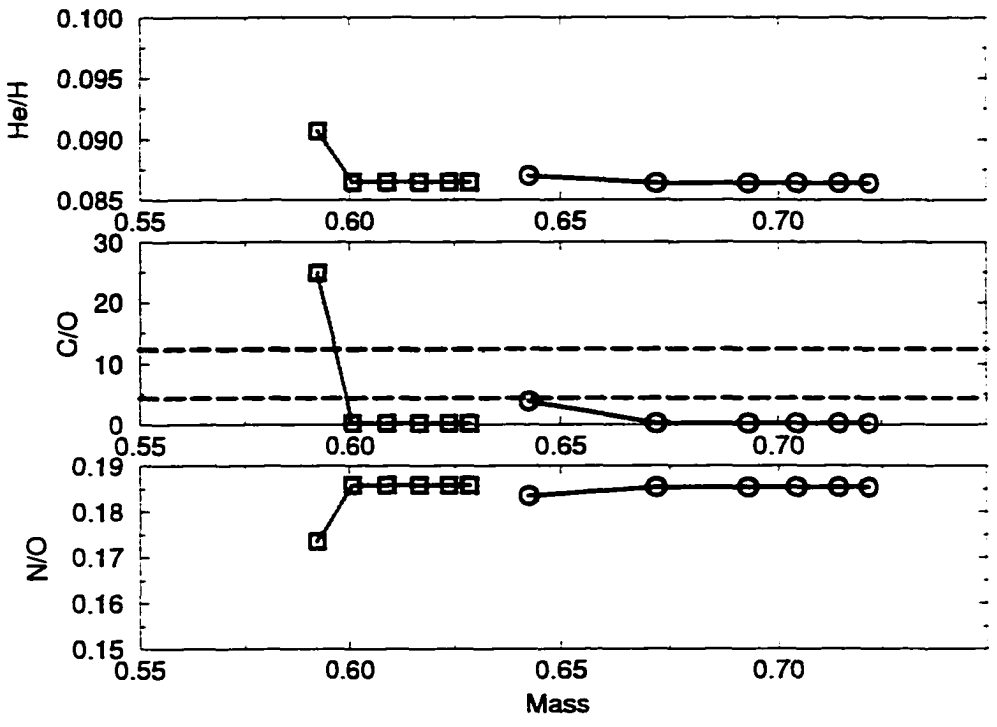

Figure 6.2: Shown in the panels of this figure is the evolution of the surface abundance ratios. The symbols have the same meaning as the first figure. In the C/O panel the upper and lower observational limits are shown on the figure with the dark long dashed line. The range of possible He/H and N/O is encompassed by the ordinates of these figures.

also slightly reduce the C/O ratio. Thus, our delayed models are consistent with several important observed properties of the K648 system.

6.3.3 Prompt Scenario

An alternative scenario results if we apply our mass-loss formulation to the secondary luminosity peak (SLP) which follows the helium shell flash of the $1M_{\odot}$, Z=0.001 model of Boothroyd and Sackmann (1988a, BS88a). The metallicity of the BS88a model is a factor of $\sim$5 higher than M15, however, no models of the appropriate metallicity exist and we attempted to use the closest one in terms of Z, M_c, and M. The SLP corresponds to the region between point C and the vertical dashed line on figure 2 of Boothroyd and Sackmann, i.e. the same place

Parameter	Value
Luminosity	4000 $L_\odot$
Radius	400 $R_\odot$
Mass	0.58
Core Mass	0.54 $M_\odot$
Mass-Loss Rate	3.2×10^{-5} $M_\odot$ yr^{-1}
Time in Stage	2000 yr

Table 6.4: Adopted Prompt PN Ejection Parameters: The values in this table are estimated from figure 2 of BS88a for a 1.0 $M_\odot$, Z=0.001 model. All values are appropriate between point C and the vertical dashed line on this figure. The radius and luminosity are the estimated lower limits. The mass and core mass are taken from their listed values. The mass-loss rate is calculated from our mass-loss prescription. The time in this stage is estimated from the BS88a graph.

that Renzini (1989) and Renzini and Fuci-Pecci (1988) predict this event to occur when the star expands. The SLP occurs when the excess luminosity produced in the helium shell flash reaches the surface. This peak can be seen in most models of low mass AGB stars [Iben(1982), BS88a, VW93].

It should be noted that this is the point where dredge-up can occur, although it does not necessarily do so. This scenario does not require a dredge-up of carbon rich material for envelope ejection. We define the prompt scenario as ejection at the SLP without the dredge-up of carbon rich material.

The adopted parameters of this model are shown in Table 6.4. The luminosity and radius are "eyeballed" lower limits from the SLP of BS88a, while the mass and core mass are parameters stated in their text. The mass-loss rate calculated from our prescription [i.e. eq. (1)] is $\sim 10^{-5} M_\odot$ yr^{-1} (essentially the Eddington limit), which will remove the $0.03 M_\odot$ envelope in a few thousand years. This model is similar to K648 in terms of core mass and envelope mass. Values for luminosity, radius, mass-loss rate, and core mass for the prompt scenario are indicated with filled diamonds in Fig. 6.1 and observed quantities are also compared to those predicted for this scenario in Table 6.2.

A carbon-rich nebula could be formed by the prompt mechanism if a sufficient

amount of helium and carbon-rich material is ejected during the post-AGB phase and mixed with the ejected hydrogen-rich envelope. The fast wind overtaking the slower wind will produce a shock which would likely be Rayleigh-Taylor unstable, causing the nebula to mix. Only $5 - 15 \times 10^{-5}$ $M_\odot$ of material with mass fractions of ^4He=0.75 and ^{12}C=0.23 needs to be mixed into the envelope to match the C/O ratio of K648. Carbon-rich material can be ejected into the nebula during the post AGB phase. As a star moves horizontally across the HR diagram from the AGB stage to CSPN position, the mass-loss rate will decrease as the wind speed increases, so the material ejected during this transition can be mixed with the slower hydrogen rich envelope. And since the currently observed mass-loss rate of the K648 central star is $10^{-9} - 10^{-10}$ $M_\odot$ yr^{-1} (Adams et al. 1984; Bianchi et al. 1995), the nebula is no longer being polluted. Examination of the models of Vassiliadis and Wood (1994) suggests that as the star moves from the AGB phase to the CSPN phase, the mass loss rate drops from 10^{-5} $M_\odot$ yr^{-1} to $\sim 10^{-10}$ $M_\odot$ yr^{-1}. indicating that during this transition the mass loss was higher in the past, and possibly high enough to account for the carbon enrichments in K648.

In the prompt scenario, the envelope is ejected when the star is burning helium and as a result the resulting CSPN will be follow a helium burning track (Schönberner 1981, 1983; Iben 1984).

Thus, in the prompt scenario, the evolved star ejects sufficient carbon into a slower moving hydrogen-rich shell to produce the PN we observe today. Mixing is assumed to occur due to shock induced instabilities. Since the prompt scenario postulates the removal of the entire H-rich envelope during the He burning stage, we expect K648 to follow a He burning track because the H-burning shell has been extinguished during the thermal pulse. Ultimately, a white dwarf of type DB will be produced.

6.4 Discussion

One additional scenario is again a delayed one, but one in which the CSPN is a helium burner. We have not as yet performed calculations relevant to it. In this case, if a dredge-up occurs, it does so at the SLP. The stellar envelope will be enriched in carbon and the added opacity may allow an even greater expansion during the SLP, making it more likely that the envelope will be ejected during this phase. The resulting PN would be carbon rich and have a helium burning CSPN. We feel that this is also a promising model, although, proper calculations of this scenario need to be done.

Both the prompt and delayed scenarios can be made to match many of the observed features of K648. With each mechanism the radius increases dramatically: in the prompt because of the increase in luminosity of the star after a thermal pulse and in the delayed because of an increase in the opacity due to an infusion of carbon rich material. In addition, both mechanisms produce ^{12}C in sufficient amounts to explain the observed C/O ratio.

The most serious difficulty with the prompt scenario is that it can only explain the enhancement of the carbon and helium abundances by essentially adhoc means, in this case assuming the central star wind pollutes the rest of the nebula or by shocks and carbon-rich pockets due to this wind. This may not be an unreasonable assumption, since the mass of K648 is low compared to a "typical" PN ($\sim 0.1 M_{\odot}$). To test the prompt scenario would require a detailed model following the star from the horizontal branch to the central star phase with attention to the details of mass-loss to see if the central star wind can truly enhance the carbon and helium abundances of the PN plus multidimensional hydrodynamics to test the mixing hypothesis.

The difficulty with the delayed scenario is it predicts that the CSPN should be a H-burner. The dynamical age of K648 favors a He-burning CSPN which is more

likely to occur in the prompt scenario as the envelope is ejected during a phase when helium burning is dominant. Since we assume that for a given metallicity only one of these scenarios will be operative, a strong observational test to determine the correct scenario would be to search for white dwarfs in M15. If they are found to be type DB, this would favor the prompt scenario, and if they are type DA, the delayed scenario is more likely.

A point favoring the prompt scenario is that it naturally accounts for the dynamical age. On the other hand, this scenario requires the assumption of efficient mixing and there is some evidence (cf. section 3.1) that signatures of the requisite shocks are not actually observed. However, until detailed models are produced, both remain as viable evolutionary scenarios for K648 and similar systems.

Chapter 7

Conclusions

The goals of this thesis were to study the origin of the abundance patterns seen in PNe. We have shown that the abundances in PNe are the result of both initial composition and nucleosynthesis. The major conclusions of this work are as follows:

1. Planetary Nebulae must be represented by a parameter space of at least two dimensions in chemical space. One axis represents metallicity axis and the other nucleosynthesis. Also, the bulge PNe have chemical compositions that are indistinguishable from disk PNe. Some of the apparent bulge PNe are of type I.

2. We have created a surface luminosity function based on stellar mass, the mass of the hydrogen exhausted core, metallicity, and the thermal pulse number. Using this function our synthetic TP-AGB models closely approximate the behavior of more realistic TP-AGB models.

3. Our synthetic TP-AGB models incorporate the most realistic available parameters and physics and produce results that match the expected behavior. Low ($M \leq 4M_{\odot}$) and intermediate ($M > 4M_{\odot}$) mass stars respectively produce PNe rich in carbon and nitrogen as expected. Intermediate mass models encounter hot-bottom burning, preventing them from becoming carbon stars.

4. Helium is produced in low and intermediate mass stars via the third and second dredge-ups, respectively.

5. There is good agreement between our synthetic TP-AGB models and PN abundances. On each abundance ratio-abundance ratio plot we have found generally good agreement.

6. In nitrogen-rich PNe (type I), we found that nitrogen is produced via hot-bottom burning, a process which depletes carbon. Helium is produced via the second dredge-up. Hot-bottom burning shortens the TP-AGB lifetime, restricting the amount of nitrogen that can be produced.

7. In carbon-rich PNe, we found that both carbon and helium are produced via the third dredge-up.

8. The evidence for ON cycling is inconclusive. We have found that the predicted amount of oxygen depletion via ON cycling is small and difficult to detect observationally.

9. When we infer the progenitor masses of C-rich ($M \gtrsim 1.7\ M_{\odot}$) and N-rich ($M \gtrsim 4.0\ M_{\odot}$) PNe, we find that they lie in a narrow metallicity range ($\approx 0.2 dex$).

10. We have examined possible models for the formation of halo PNe K648. To the best of our knowledge, we are the first group to actually attempt to model the processes involved. We found three possible models:

    - A delayed model where carbon dredged into the envelope increases the opacity, causing the envelope to expand and the mass-loss rate to increase to levels where the envelope is rapidly ($\sim$1000 years) ejected.
    - A prompt model where the surface luminosity increase at the end of the thermal pulse causes the envelope to expand, causing accelerated mass-loss.

- A combination model where the carbon dredged up and the increased luminosity at the end of the thermal pulse cause envelope expansion, also causing accelerated mass-loss.

7.1 Future Work

There is other observational evidence to consider. The only halo PN considered in detail was PN K648: we hope model other halo PNe. Also, models will be made of the Magellanic Cloud PNe. The progenitors of Magellanic Cloud PNe have a similar range as Galactic PNe, however, the initial abundances are different. By comparing models of Magellanic Cloud PNe to the abundance data, we can test our models as a function of metallicity.

Appendix A

Model Results

This appendix contains tables with the predicted PN abundance ratios as a function of mass. The free parameters are the abundance of iron relative to the solar abundance ([Fe/H]) and the mixing length parameter (α). The first column of each table indicates the ZAMS mass of each model in solar units. The second column indicates the white dwarf mass in solar units.

Mass	M_{WD}	O/H	He/H	N/O	C/O
1.00	0.555	8.94	0.112	0.244	0.329
1.10	0.568	8.94	0.111	0.246	0.327
1.20	0.575	8.94	0.110	0.248	0.324
1.30	0.588	8.94	0.109	0.250	0.322
1.40	0.602	8.93	0.108	0.252	0.320
1.50	0.617	8.93	0.107	0.255	0.318
1.60	0.626	8.93	0.106	0.256	0.316
1.70	0.640	8.93	0.105	0.259	0.388
1.80	0.648	8.93	0.107	0.261	0.634
1.90	0.654	8.93	0.108	0.262	0.916
2.00	0.659	8.93	0.111	0.264	1.352
2.10	0.666	8.93	0.114	0.265	1.816
2.20	0.676	8.93	0.117	0.267	2.249
2.30	0.680	8.93	0.116	0.269	2.173
2.40	0.690	8.93	0.118	0.271	2.399
2.50	0.699	8.93	0.118	0.274	2.432
2.60	0.710	8.93	0.118	0.275	2.559
2.80	0.726	8.93	0.117	0.279	2.523
2.90	0.735	8.93	0.116	0.281	2.500
3.10	0.752	8.93	0.116	0.283	2.500
3.30	0.773	8.93	0.116	0.283	2.588
3.40	0.782	8.93	0.116	0.283	2.624
3.50	0.786	8.93	0.116	0.283	2.570
3.60	0.805	8.93	0.114	0.283	2.388
3.70	0.822	8.93	0.111	0.283	2.032
3.80	0.844	8.93	0.110	0.283	1.892
3.90	0.869	8.93	0.109	0.283	1.778
4.00	0.885	8.93	0.107	0.284	1.603
4.10	0.854	8.92	0.104	0.889	0.519
4.20	0.860	8.91	0.102	1.007	0.245
4.30	0.873	8.90	0.101	0.920	0.247
4.40	0.891	8.90	0.100	0.785	0.219
4.50	0.900	8.89	0.102	0.804	0.284
4.60	0.906	8.89	0.104	0.853	0.229
4.70	0.913	8.88	0.106	0.899	0.247
4.80	0.919	8.88	0.108	0.942	0.249
4.90	0.927	8.87	0.111	0.991	0.324
5.00	0.933	8.87	0.112	1.035	0.286
6.00	0.991	8.81	0.130	1.560	0.412
7.00	1.037	8.79	0.142	1.778	0.498
8.00	1.079	8.80	0.150	1.660	0.459

Table A.1: [Fe/H]=0.0 α=2.3 Galaxy

Mass	M_{WD}	O/H	He/H	N/O	C/O
1.00	0.553	9.05	0.117	0.244	0.329
1.10	0.554	9.05	0.116	0.246	0.327
1.20	0.567	9.05	0.115	0.248	0.324
1.30	0.574	9.04	0.114	0.250	0.322
1.40	0.587	9.04	0.113	0.252	0.320
1.50	0.601	9.04	0.112	0.255	0.318
1.60	0.610	9.04	0.111	0.256	0.316
1.70	0.625	9.04	0.110	0.259	0.313
1.80	0.634	9.04	0.110	0.261	0.353
1.90	0.645	9.04	0.111	0.262	0.540
2.00	0.652	9.04	0.112	0.265	0.729
2.20	0.668	9.04	0.118	0.269	1.416
2.40	0.686	9.04	0.122	0.272	1.875
2.60	0.701	9.04	0.122	0.276	1.928
2.80	0.721	9.04	0.122	0.280	2.023
3.00	0.737	9.04	0.121	0.284	1.991
3.20	0.757	9.03	0.121	0.284	2.046
3.40	0.772	9.03	0.121	0.284	2.089
3.60	0.785	9.03	0.121	0.284	2.084
3.80	0.805	9.03	0.123	0.284	2.239
3.90	0.816	9.03	0.124	0.283	2.360
4.00	0.821	9.04	0.122	0.283	2.218
4.02	0.825	9.03	0.122	0.283	2.158
4.04	0.824	9.03	0.121	0.284	2.061
4.06	0.830	9.03	0.121	0.284	2.046
4.08	0.832	9.03	0.121	0.284	2.046
4.10	0.831	9.03	0.119	0.284	1.950
4.20	0.851	9.03	0.119	0.284	1.849
4.30	0.883	9.04	0.118	0.284	1.754
4.50	0.886	9.03	0.114	0.802	0.843
4.60	0.864	9.02	0.110	1.099	0.260
4.70	0.871	9.01	0.108	0.995	0.248
4.80	0.886	9.00	0.106	0.873	0.221
4.90	0.895	9.00	0.108	0.863	0.249
5.00	0.901	9.00	0.110	0.895	0.239
6.00	0.961	8.96	0.128	1.211	0.352
7.00	1.010	8.95	0.140	1.256	0.359
8.00	1.062	8.96	0.149	1.148	0.321

Table A.2: [Fe/H]=0.1 α=2.3 Galaxy

Mass	M_{WD}	O/H	He/H	N/O	C/O
1.00	0.543	9.16	0.124	0.244	0.329
1.20	0.557	9.16	0.122	0.248	0.324
1.40	0.578	9.15	0.120	0.252	0.320
1.60	0.599	9.15	0.118	0.256	0.316
1.80	0.630	9.15	0.116	0.261	0.311
2.00	0.647	9.15	0.117	0.265	0.532
2.20	0.666	9.15	0.125	0.269	1.156
2.40	0.677	9.15	0.127	0.272	1.340
3.00	0.735	9.15	0.130	0.284	1.702
3.10	0.740	9.14	0.128	0.284	1.629
3.20	0.750	9.14	0.128	0.284	1.648
3.30	0.761	9.14	0.129	0.284	1.722
3.40	0.765	9.14	0.128	0.284	1.694
3.50	0.775	9.14	0.129	0.284	1.730
3.60	0.785	9.14	0.130	0.284	1.795
3.70	0.790	9.14	0.130	0.284	1.816
3.80	0.800	9.15	0.131	0.284	1.879
3.90	0.811	9.15	0.132	0.284	1.972
4.00	0.815	9.15	0.132	0.284	1.995
4.10	0.826	9.15	0.133	0.284	2.056
4.20	0.838	9.15	0.134	0.283	2.163
4.30	0.844	9.15	0.136	0.284	2.275
4.40	0.858	9.15	0.138	0.285	2.415
4.50	0.863	9.15	0.139	0.304	2.455
4.60	0.879	9.15	0.140	0.348	2.547
4.70	0.883	9.15	0.140	0.498	2.355
4.80	0.868	9.15	0.134	1.151	1.300
4.90	0.910	9.15	0.134	0.798	1.626
5.00	0.934	9.15	0.133	0.824	1.503
6.00	0.926	9.08	0.124	1.140	0.238
7.00	0.979	9.08	0.136	1.005	0.289
8.00	1.044	9.09	0.146	0.925	0.235

Table A.3: [Fe/H]=0.2 α=2.3 Galaxy

Mass	M_{WD}	O/H	He/H	N/O	C/O
1.00	0.563	8.83	0.107	0.244	0.329
1.10	0.575	8.83	0.106	0.246	0.327
1.20	0.583	8.83	0.105	0.248	0.324
1.30	0.596	8.83	0.105	0.250	0.322
1.40	0.611	8.83	0.104	0.252	0.320
1.50	0.626	8.83	0.103	0.254	0.318
1.60	0.634	8.83	0.102	0.256	0.426
1.70	0.645	8.83	0.104	0.258	0.824
1.80	0.651	8.82	0.106	0.260	1.233
1.90	0.657	8.82	0.107	0.262	1.581
3.30	0.782	8.82	0.112	0.282	3.177
3.50	0.826	8.82	0.107	0.282	2.415
3.90	0.857	8.81	0.097	1.081	0.291
4.10	0.891	8.79	0.096	0.871	0.321
4.50	0.926	8.76	0.104	1.014	0.358
5.00	0.960	8.72	0.114	1.365	0.502
7.00	1.058	8.61	0.142	2.729	0.622
8.00	1.094	8.62	0.149	2.698	0.547

Table A.4: [Fe/H]=-0.1 α=2.3 Galaxy

Mass	M_{WD}	O/H	He/H	N/O	C/O
1.00	0.569	8.73	0.104	0.244	0.329
1.10	0.582	8.73	0.103	0.246	0.327
1.20	0.589	8.73	0.102	0.248	0.324
1.30	0.604	8.72	0.101	0.250	0.322
1.40	0.618	8.72	0.100	0.252	0.320
1.50	0.634	8.72	0.099	0.255	0.318
1.60	0.640	8.72	0.101	0.256	0.710
1.70	0.648	8.72	0.102	0.258	1.268
1.80	0.653	8.72	0.104	0.259	1.778
1.90	0.659	8.72	0.106	0.261	2.188
2.00	0.664	8.72	0.108	0.262	2.748

Table A.5: [Fe/H]=-0.2 α=2.3 Galaxy

Mass	M_{WD}	O/H	He/H	N/O	C/O
1.00	0.594	8.62	0.101	0.209	0.283
1.20	0.610	8.62	0.099	0.213	0.279
1.40	0.633	8.62	0.097	0.217	0.392
1.60	0.650	8.62	0.100	0.220	1.563
1.80	0.657	8.62	0.104	0.222	2.904
2.00	0.670	8.62	0.109	0.224	4.581
2.20	0.688	8.62	0.111	0.227	5.284
2.40	0.705	8.62	0.110	0.230	5.433
3.50	0.856	8.61	0.093	1.245	1.074

Table A.6: [Fe/H]=-0.5 α=2.3 Galaxy

Mass	M_{WD}	O/H	He/H	N/O	C/O
1.00	0.615	8.31	0.096	0.188	0.254
1.20	0.638	8.31	0.095	0.191	0.685
1.40	0.646	8.31	0.097	0.193	2.270
1.60	0.651	8.31	0.100	0.195	4.808
1.80	0.658	8.31	0.101	0.196	6.252
2.00	0.668	8.32	0.103	0.198	8.054
2.20	0.683	8.32	0.103	0.200	8.730
2.40	0.715	8.32	0.108	0.201	11.429
3.00	0.811	8.32	0.101	0.210	8.790
3.50	0.899	8.27	0.089	3.412	0.908
3.60	0.927	8.18	0.087	3.614	1.007
3.70	0.954	8.09	0.086	3.917	1.324
3.80	0.966	8.05	0.088	4.375	1.496

Table A.7: [Fe/H]=-1.0 α=2.3 Galaxy

Mass	M_{WD}	O/H	He/H	N/O	C/O
1.00	0.549	8.94	0.112	0.244	0.329
1.50	0.591	8.93	0.107	0.255	0.318
2.00	0.645	8.93	0.104	0.265	0.512
2.50	0.672	8.93	0.109	0.275	1.330
3.00	0.709	8.93	0.111	0.284	1.816
4.00	0.828	8.92	0.103	0.285	1.033
4.50	0.878	8.92	0.100	0.417	0.316
5.00	0.908	8.92	0.111	0.615	0.285
6.00	0.958	8.90	0.127	0.741	0.270
8.00	1.073	8.86	0.149	1.084	0.425

Table A.8: [Fe/H]=0.2 α=1.9 Galaxy

Mass	M_{WD}	O/H	He/H	N/O	C/O
2.60	0.725	8.93	0.122	0.275	3.020
2.70	0.732	8.93	0.121	0.277	2.938
2.80	0.743	8.93	0.121	0.279	2.944
2.90	0.754	8.93	0.120	0.281	2.917
3.10	0.772	8.93	0.119	0.282	2.871
3.20	0.783	8.93	0.119	0.282	2.891
3.30	0.794	8.93	0.119	0.282	2.965
3.40	0.804	8.93	0.119	0.282	2.965
3.90	0.899	8.93	0.111	0.284	2.023
4.10	0.876	8.92	0.105	1.374	0.265
4.50	0.925	8.86	0.103	1.156	0.284
5.00	0.962	8.82	0.115	1.521	0.417
7.00	1.059	8.70	0.146	3.221	0.624
8.00	1.090	8.70	0.154	3.296	0.533

Table A.9: [Fe/H]=0.2 α=2.5 Galaxy

Appendix B

Yields

In this chapter we present the model yields for ^{4}He, ^{12}C, ^{13}C, ^{14}N, and ^{16}O for low and intermediate mass stars.

Mass	M[H]	M[He]	M[C12]	M[N14]	M[O16]	M[C13]
1.00	-1.30E-02	1.30E-02	-3.53E-04	4.12E-04	-4.30E-05	3.11E-05
1.50	-1.79E-02	1.79E-02	-7.80E-04	9.10E-04	-8.66E-05	5.94E-05
2.00	-1.86E-02	1.71E-02	1.08E-04	1.47E-03	-1.79E-04	8.33E-05
2.50	-5.17E-02	3.82E-02	1.12E-02	2.02E-03	-6.44E-04	1.01E-04
3.00	-7.43E-02	5.15E-02	1.95E-02	2.67E-03	-1.00E-03	1.17E-04
4.00	-4.45E-02	2.95E-02	1.10E-02	3.87E-03	-7.66E-04	1.68E-04
4.50	-1.86E-02	1.72E-02	-5.99E-03	7.83E-03	-6.42E-04	1.07E-03
5.00	-1.01E-01	9.87E-02	-9.23E-03	1.42E-02	-2.11E-03	2.84E-04
6.00	-2.51E-01	2.50E-01	-1.18E-02	1.95E-02	-5.34E-03	1.84E-04
8.00	-5.36E-01	5.34E-01	-1.56E-02	3.13E-02	-1.27E-02	3.99E-04

Table B.1: [Fe/H]= 0.0 and α= 1.90

Mass	M[H]	M[He]	M[C12]	M[N14]	M[O16]	M[C13]
1.00	-1.28E-02	1.28E-02	-3.46E-04	4.04E-04	-4.21E-05	3.05E-05
1.10	-1.44E-02	1.44E-02	-4.25E-04	4.96E-04	-5.07E-05	3.63E-05
1.20	-1.57E-02	1.57E-02	-5.06E-04	5.90E-04	-5.92E-05	4.19E-05
1.30	-1.66E-02	1.66E-02	-5.89E-04	6.87E-04	-6.78E-05	4.75E-05
1.40	-1.72E-02	1.72E-02	-6.73E-04	7.85E-04	-7.60E-05	5.27E-05
1.50	-1.74E-02	1.74E-02	-7.59E-04	8.85E-04	-8.42E-05	5.77E-05
1.60	-1.74E-02	1.74E-02	-8.51E-04	9.92E-04	-9.28E-05	6.29E-05
1.70	-1.93E-02	1.85E-02	-2.14E-04	1.09E-03	-1.28E-04	6.75E-05
1.80	-2.42E-02	2.16E-02	1.52E-03	1.19E-03	-2.03E-04	7.18E-05
1.90	-3.16E-02	2.61E-02	4.13E-03	1.29E-03	-3.10E-04	7.58E-05
2.00	-4.21E-02	3.26E-02	7.87E-03	1.38E-03	-4.58E-04	7.92E-05
2.10	-5.54E-02	4.12E-02	1.23E-02	1.46E-03	-6.29E-04	8.20E-05
2.20	-6.85E-02	4.97E-02	1.67E-02	1.54E-03	-7.98E-04	8.45E-05
2.30	-7.16E-02	5.17E-02	1.77E-02	1.66E-03	-8.46E-04	8.87E-05
2.40	-8.07E-02	5.75E-02	2.07E-02	1.77E-03	-9.64E-04	9.17E-05
2.50	-8.61E-02	6.09E-02	2.25E-02	1.88E-03	-1.04E-03	9.49E-05
2.60	-9.18E-02	6.45E-02	2.45E-02	2.00E-03	-1.12E-03	9.80E-05
2.80	-9.68E-02	6.71E-02	2.64E-02	2.26E-03	-1.21E-03	1.05E-04
2.90	-1.00E-01	6.91E-02	2.78E-02	2.39E-03	-1.27E-03	1.08E-04
3.10	-1.04E-01	7.07E-02	2.96E-02	2.64E-03	-1.35E-03	1.16E-04
3.30	-1.12E-01	7.53E-02	3.28E-02	2.83E-03	-1.48E-03	1.24E-04
3.40	-1.18E-01	7.91E-02	3.47E-02	2.93E-03	-1.55E-03	1.28E-04
3.50	-1.21E-01	8.06E-02	3.56E-02	3.04E-03	-1.59E-03	1.33E-04
3.60	-1.11E-01	7.40E-02	3.25E-02	3.17E-03	-1.48E-03	1.39E-04
3.70	-9.65E-02	6.42E-02	2.80E-02	3.32E-03	-1.31E-03	1.45E-04
3.80	-8.88E-02	5.90E-02	2.56E-02	3.45E-03	-1.22E-03	1.50E-04
3.90	-8.39E-02	5.56E-02	2.39E-02	3.56E-03	-1.16E-03	1.61E-04
4.00	-7.62E-02	5.05E-02	2.12E-02	3.69E-03	-1.07E-03	2.91E-04
4.10	-5.04E-02	3.34E-02	-1.54E-03	1.86E-02	-9.15E-04	2.21E-03
4.20	-3.75E-02	2.49E-02	-6.88E-03	2.24E-02	-1.31E-03	4.47E-04
4.30	-2.70E-02	1.79E-02	-7.67E-03	2.02E-02	-2.00E-03	3.17E-04
4.40	-1.58E-02	1.04E-02	-8.32E-03	1.70E-02	-2.11E-03	2.29E-04
4.50	-2.97E-02	2.45E-02	-8.52E-03	1.76E-02	-2.64E-03	2.27E-04
4.60	-4.64E-02	4.11E-02	-8.74E-03	1.86E-02	-3.40E-03	2.36E-04
4.70	-6.36E-02	5.79E-02	-8.90E-03	1.98E-02	-4.05E-03	2.48E-04
4.80	-8.06E-02	7.45E-02	-9.08E-03	2.08E-02	-4.61E-03	2.57E-04
4.90	-9.75E-02	9.11E-02	-9.20E-03	2.20E-02	-5.29E-03	2.71E-04
5.00	-1.14E-01	1.07E-01	-9.42E-03	2.31E-02	-5.83E-03	2.80E-04
6.00	-2.75E-01	2.64E-01	-1.12E-02	3.52E-02	-1.26E-02	4.14E-04
7.00	-4.18E-01	4.07E-01	-1.32E-02	4.16E-02	-1.68E-02	4.83E-04
8.00	-5.49E-01	5.41E-01	-1.56E-02	4.21E-02	-1.85E-02	4.75E-04

Table B.2: [Fe/H]= 0.0 and α= 2.30

Mass	M[H]	M[He]	M[C12]	M[N14]	M[O16]	M[C13]
1.00	-1.24E-02	1.24E-02	-4.41E-04	5.15E-04	-5.37E-05	3.88E-05
1.10	-1.41E-02	1.41E-02	-5.46E-04	6.38E-04	-6.52E-05	4.67E-05
1.20	-1.52E-02	1.52E-02	-6.49E-04	7.57E-04	-7.60E-05	5.38E-05
1.30	-1.62E-02	1.62E-02	-7.56E-04	8.82E-04	-8.70E-05	6.09E-05
1.40	-1.67E-02	1.67E-02	-8.63E-04	1.01E-03	-9.75E-05	6.76E-05
1.50	-1.68E-02	1.68E-02	-9.72E-04	1.13E-03	-1.08E-04	7.39E-05
1.60	-1.68E-02	1.68E-02	-1.09E-03	1.27E-03	-1.19E-04	8.05E-05
1.70	-1.63E-02	1.63E-02	-1.20E-03	1.40E-03	-1.29E-04	8.65E-05
1.80	-1.65E-02	1.62E-02	-1.02E-03	1.54E-03	-1.54E-04	9.25E-05
1.90	-2.00E-02	1.81E-02	3.42E-04	1.68E-03	-2.36E-04	9.79E-05
2.00	-2.51E-02	2.10E-02	2.37E-03	1.80E-03	-3.48E-04	1.03E-04
2.20	-5.49E-02	4.01E-02	1.23E-02	2.00E-03	-8.48E-04	1.09E-04
2.40	-7.60E-02	5.36E-02	1.93E-02	2.24E-03	-1.21E-03	1.16E-04
2.60	-8.39E-02	5.83E-02	2.21E-02	2.55E-03	-1.37E-03	1.25E-04
2.80	-9.29E-02	6.35E-02	2.54E-02	2.86E-03	-1.55E-03	1.33E-04
3.00	-9.72E-02	6.56E-02	2.72E-02	3.21E-03	-1.67E-03	1.41E-04
3.20	-1.04E-01	6.91E-02	3.01E-02	3.46E-03	-1.83E-03	1.52E-04
3.40	-1.11E-01	7.34E-02	3.26E-02	3.72E-03	-1.97E-03	1.63E-04
3.60	-1.21E-01	7.94E-02	3.57E-02	3.97E-03	-2.14E-03	1.74E-04
3.80	-1.37E-01	8.99E-02	4.10E-02	4.18E-03	-2.40E-03	1.84E-04
3.90	-1.47E-01	9.64E-02	4.42E-02	4.29E-03	-2.55E-03	1.88E-04
4.00	-1.40E-01	9.18E-02	4.18E-02	4.47E-03	-2.45E-03	1.97E-04
4.02	-1.38E-01	9.07E-02	4.12E-02	4.50E-03	-2.42E-03	2.00E-04
4.04	-1.33E-01	8.71E-02	3.94E-02	4.56E-03	-2.34E-03	2.14E-04
4.06	-1.32E-01	8.65E-02	3.90E-02	4.58E-03	-2.32E-03	2.16E-04
4.08	-1.29E-01	8.45E-02	3.80E-02	4.63E-03	-2.28E-03	2.37E-04
4.10	-1.24E-01	8.12E-02	3.63E-02	4.68E-03	-2.20E-03	3.24E-04
4.20	-1.17E-01	7.66E-02	3.35E-02	4.86E-03	-2.09E-03	6.96E-04
4.30	-1.15E-01	7.52E-02	3.28E-02	4.97E-03	-2.03E-03	6.32E-04
4.50	-8.59E-02	5.62E-02	4.67E-03	2.18E-02	-1.69E-03	5.36E-03
4.60	-5.85E-02	3.83E-02	-1.02E-02	3.45E-02	-2.12E-03	5.93E-04
4.70	-4.25E-02	2.78E-02	-1.11E-02	3.09E-02	-3.19E-03	4.43E-04
4.80	-2.80E-02	1.83E-02	-1.19E-02	2.68E-02	-3.52E-03	3.42E-04
4.90	-3.80E-02	2.93E-02	-1.22E-02	2.66E-02	-4.05E-03	3.27E-04
5.00	-5.45E-02	4.57E-02	-1.25E-02	2.77E-02	-4.79E-03	3.35E-04
6.00	-2.13E-01	2.02E-01	-1.48E-02	3.87E-02	-1.19E-02	4.48E-04
7.00	-3.50E-01	3.42E-01	-1.76E-02	4.22E-02	-1.59E-02	4.71E-04
8.00	-4.79E-01	4.75E-01	-2.05E-02	4.22E-02	-1.69E-02	4.38E-04

Table B.3: [Fe/H]= 0.1 and α= 2.30

Mass	M[H]	M[He]	M[C12]	M[N14]	M[O16]	M[C13]
1.00	-1.19E-02	1.19E-02	-5.65E-04	6.60E-04	-6.88E-05	4.97E-05
1.20	-1.45E-02	1.45E-02	-8.29E-04	9.67E-04	-9.71E-05	6.87E-05
1.40	-1.58E-02	1.58E-02	-1.10E-03	1.28E-03	-1.24E-04	8.61E-05
1.60	-1.57E-02	1.57E-02	-1.38E-03	1.61E-03	-1.51E-04	1.02E-04
1.80	-1.44E-02	1.44E-02	-1.68E-03	1.96E-03	-1.77E-04	1.17E-04
2.00	-1.90E-02	1.65E-02	3.85E-04	2.30E-03	-3.50E-04	1.31E-04
2.20	-5.18E-02	3.73E-02	1.14E-02	2.53E-03	-1.07E-03	1.38E-04
2.40	-6.45E-02	4.51E-02	1.57E-02	2.88E-03	-1.37E-03	1.49E-04
3.00	-9.48E-02	6.25E-02	2.67E-02	4.04E-03	-2.17E-03	1.77E-04
3.10	-9.51E-02	6.23E-02	2.71E-02	4.23E-03	-2.22E-03	1.85E-04
3.20	-9.87E-02	6.41E-02	2.86E-02	4.38E-03	-2.33E-03	1.92E-04
3.30	-1.03E-01	6.68E-02	3.04E-02	4.53E-03	-2.45E-03	1.98E-04
3.40	-1.06E-01	6.87E-02	3.12E-02	4.70E-03	-2.52E-03	2.06E-04
3.50	-1.13E-01	7.31E-02	3.34E-02	4.84E-03	-2.67E-03	2.12E-04
3.60	-1.21E-01	7.80E-02	3.59E-02	4.98E-03	-2.83E-03	2.18E-04
3.70	-1.25E-01	8.06E-02	3.71E-02	5.15E-03	-2.93E-03	2.26E-04
3.80	-1.34E-01	8.66E-02	4.01E-02	5.28E-03	-3.13E-03	2.32E-04
3.90	-1.44E-01	9.30E-02	4.33E-02	5.40E-03	-3.33E-03	2.37E-04
4.00	-1.51E-01	9.74E-02	4.55E-02	5.55E-03	-3.48E-03	2.45E-04
4.10	-1.63E-01	1.05E-01	4.93E-02	5.66E-03	-3.72E-03	2.58E-04
4.20	-1.76E-01	1.14E-01	5.36E-02	5.77E-03	-3.99E-03	3.04E-04
4.30	-1.87E-01	1.20E-01	5.66E-02	5.91E-03	-4.21E-03	6.67E-04
4.40	-2.02E-01	1.30E-01	6.10E-02	6.05E-03	-4.52E-03	1.49E-03
4.50	-2.15E-01	1.39E-01	6.14E-02	6.86E-03	-4.79E-03	4.94E-03
4.60	-2.34E-01	1.51E-01	6.31E-02	8.55E-03	-5.17E-03	8.43E-03
4.70	-2.34E-01	1.50E-01	5.36E-02	1.46E-02	-5.17E-03	1.29E-02
4.80	-2.02E-01	1.30E-01	1.98E-02	4.34E-02	-4.61E-03	1.13E-02
4.90	-2.02E-01	1.30E-01	3.08E-02	2.85E-02	-4.52E-03	1.33E-02
5.00	-1.95E-01	1.25E-01	2.72E-02	3.05E-02	-4.35E-03	1.28E-02
6.00	-1.28E-01	1.10E-01	-1.95E-02	5.16E-02	-1.20E-02	6.00E-04
7.00	-2.46E-01	2.38E-01	-2.33E-02	4.77E-02	-1.52E-02	5.12E-04
8.00	-3.73E-01	3.70E-01	-2.70E-02	4.78E-02	-1.61E-02	4.65E-04

Table B.4: [Fe/H]= 0.2 and α= 2.30

Mass	M[H]	M[He]	M[C12]	M[N14]	M[O16]	M[C13]
1.00	-1.30E-02	1.30E-02	-2.71E-04	3.16E-04	-3.30E-05	2.38E-05
1.10	-1.47E-02	1.47E-02	-3.33E-04	3.88E-04	-3.97E-05	2.84E-05
1.20	-1.60E-02	1.60E-02	-3.97E-04	4.63E-04	-4.65E-05	3.29E-05
1.30	-1.71E-02	1.71E-02	-4.63E-04	5.40E-04	-5.32E-05	3.73E-05
1.40	-1.77E-02	1.77E-02	-5.29E-04	6.17E-04	-5.97E-05	4.14E-05
1.50	-1.79E-02	1.79E-02	-5.97E-04	6.96E-04	-6.62E-05	4.54E-05
1.60	-1.92E-02	1.88E-02	-2.98E-04	7.80E-04	-8.36E-05	4.95E-05
1.70	-2.38E-02	2.18E-02	1.23E-03	8.57E-04	-1.35E-04	5.30E-05
1.80	-3.03E-02	2.59E-02	3.44E-03	9.33E-04	-2.05E-04	5.64E-05
1.90	-3.91E-02	3.15E-02	6.50E-03	1.01E-03	-2.99E-04	5.93E-05
3.30	-1.13E-01	7.70E-02	3.30E-02	2.24E-03	-1.11E-03	9.84E-05
3.50	-8.64E-02	5.85E-02	2.47E-02	2.47E-03	-8.67E-04	1.08E-04
3.90	-3.45E-02	2.31E-02	-4.20E-03	1.76E-02	-8.22E-04	4.70E-04
4.10	-1.61E-02	1.08E-02	-5.67E-03	1.38E-02	-1.78E-03	2.05E-04
4.50	-7.09E-02	6.58E-02	-6.37E-03	1.62E-02	-3.90E-03	2.07E-04
5.00	-1.54E-01	1.47E-01	-7.01E-03	2.17E-02	-6.96E-03	2.68E-04
7.00	-4.65E-01	4.50E-01	-9.90E-03	4.34E-02	-1.72E-02	5.20E-04
8.00	-6.00E-01	5.86E-01	-1.17E-02	4.61E-02	-1.95E-02	5.50E-04

Table B.5: [Fe/H]=-0.1 and α= 2.30

Mass	M[H]	M[He]	M[C12]	M[N14]	M[O16]	M[C13]
1.00	-1.32E-02	1.32E-02	-2.12E-04	2.48E-04	-2.58E-05	1.87E-05
1.10	-1.49E-02	1.49E-02	-2.61E-04	3.04E-04	-3.11E-05	2.23E-05
1.20	-1.63E-02	1.63E-02	-3.12E-04	3.64E-04	-3.65E-05	2.58E-05
1.30	-1.74E-02	1.74E-02	-3.64E-04	4.24E-04	-4.18E-05	2.93E-05
1.40	-1.80E-02	1.80E-02	-4.16E-04	4.85E-04	-4.70E-05	3.26E-05
1.50	-1.83E-02	1.83E-02	-4.70E-04	5.48E-04	-5.21E-05	3.57E-05
1.60	-2.20E-02	2.09E-02	6.07E-04	6.11E-04	-8.18E-05	3.89E-05
1.70	-2.82E-02	2.49E-02	2.58E-03	6.72E-04	-1.30E-04	4.17E-05
1.80	-3.54E-02	2.96E-02	5.01E-03	7.31E-04	-1.87E-04	4.43E-05
1.90	-4.65E-02	3.68E-02	8.77E-03	7.86E-04	-2.72E-04	4.65E-05
2.00	-5.64E-02	4.30E-02	1.22E-02	8.42E-04	-3.51E-04	4.87E-05

Table B.6: [Fe/H]=-0.2 and α= 2.30

Mass	M[H]	M[He]	M[C12]	M[N14]	M[O16]	M[C13]
1.00	-1.27E-02	1.27E-02	-1.36E-04	1.59E-04	-1.93E-05	1.20E-05
1.20	-1.64E-02	1.64E-02	-2.07E-04	2.41E-04	-2.82E-05	1.72E-05
1.40	-1.88E-02	1.86E-02	-9.21E-05	3.23E-04	-3.94E-05	2.17E-05
1.60	-3.12E-02	2.73E-02	3.52E-03	4.03E-04	-1.06E-04	2.58E-05
1.80	-4.86E-02	3.89E-02	9.13E-03	4.82E-04	-2.03E-04	2.94E-05
2.00	-7.18E-02	5.40E-02	1.70E-02	5.54E-04	-3.32E-04	3.23E-05
2.20	-8.91E-02	6.51E-02	2.29E-02	6.36E-04	-4.27E-04	3.51E-05
2.40	-1.01E-01	7.29E-02	2.66E-02	7.32E-04	-4.89E-04	3.82E-05
3.50	-4.76E-02	3.32E-02	3.00E-03	1.14E-02	-3.17E-04	1.51E-03

Table B.7: [Fe/H]=-0.5 and α= 2.30

Mass	M[H]	M[He]	M[C12]	M[N14]	M[O16]	M[C13]
1.00	-1.25E-02	1.25E-02	-5.80E-05	6.76E-05	-9.14E-06	5.10E-06
1.20	-1.66E-02	1.65E-02	4.49E-05	1.03E-04	-1.42E-05	7.35E-06
1.40	-2.61E-02	2.38E-02	2.20E-03	1.40E-04	-3.06E-05	9.48E-06
1.60	-3.79E-02	3.22E-02	5.49E-03	1.78E-04	-5.26E-05	1.15E-05
1.80	-5.43E-02	4.33E-02	1.07E-02	2.14E-04	-8.38E-05	1.31E-05
2.00	-7.10E-02	5.41E-02	1.65E-02	2.51E-04	-1.16E-04	1.46E-05
2.20	-8.28E-02	6.16E-02	2.07E-02	2.91E-04	-1.38E-04	1.60E-05
2.40	-1.12E-01	8.12E-02	2.98E-02	3.22E-04	-1.77E-04	1.68E-05
3.00	-1.05E-01	7.53E-02	2.93E-02	4.78E-04	-1.34E-04	2.09E-05
3.50	-4.68E-02	3.31E-02	4.19E-04	1.54E-02	-5.94E-04	3.10E-04
3.60	-3.72E-02	2.61E-02	1.53E-05	1.38E-02	-1.59E-03	2.29E-04
3.70	-2.87E-02	1.98E-02	-2.04E-04	1.23E-02	-2.57E-03	1.88E-04
3.80	-4.28E-02	3.39E-02	-2.64E-04	1.29E-02	-2.99E-03	1.90E-04

Table B.8: [Fe/H]=-1.0 and α= 2.30

Mass	M[H]	M[He]	M[C12]	M[N14]	M[O16]	M[C13]
2.60	-1.06E-01	7.38E-02	2.91E-02	1.93E-03	-1.28E-03	9.52E-05
2.70	-1.06E-01	7.36E-02	2.93E-02	2.07E-03	-1.30E-03	9.92E-05
2.80	-1.10E-01	7.59E-02	3.08E-02	2.20E-03	-1.36E-03	1.02E-04
2.90	-1.14E-01	7.80E-02	3.22E-02	2.33E-03	-1.41E-03	1.05E-04
3.10	-1.18E-01	7.97E-02	3.40E-02	2.57E-03	-1.49E-03	1.13E-04
3.20	-1.21E-01	8.14E-02	3.54E-02	2.67E-03	-1.55E-03	1.17E-04
3.30	-1.26E-01	8.44E-02	3.73E-02	2.76E-03	-1.62E-03	1.21E-04
3.40	-1.32E-01	8.84E-02	3.93E-02	2.85E-03	-1.70E-03	1.25E-04
3.90	-9.50E-02	6.30E-02	2.70E-02	3.52E-03	-1.26E-03	7.19E-04
4.10	-6.15E-02	4.08E-02	-6.10E-03	3.01E-02	-1.39E-03	5.92E-04
4.50	-4.13E-02	3.21E-02	-8.38E-03	2.39E-02	-5.23E-03	2.90E-04
5.00	-1.28E-01	1.16E-01	-9.14E-03	3.13E-02	-9.14E-03	3.65E-04
7.00	-4.60E-01	4.32E-01	-1.24E-02	6.42E-02	-2.32E-02	7.42E-04
8.00	-5.97E-01	5.70E-01	-1.46E-02	6.94E-02	-2.69E-02	8.04E-04

Table B.9: [Fe/H]= 0.0 and α= 2.50

Mass	M[H]	M[He]	M[C12]	M[N14]	M[O16]	M[C13]
1.00	-1.23E-02	1.23E-02	-4.40E-04	5.13E-04	-5.35E-05	3.87E-05
1.20	-1.51E-02	1.51E-02	-6.43E-04	7.50E-04	-7.52E-05	5.33E-05
1.40	-1.64E-02	1.64E-02	-8.51E-04	9.92E-04	-9.61E-05	6.66E-05
1.60	-1.65E-02	1.65E-02	-1.07E-03	1.25E-03	-1.17E-04	7.94E-05
1.65	-1.64E-02	1.64E-02	-1.13E-03	1.32E-03	-1.22E-04	8.24E-05
1.70	-1.68E-02	1.66E-02	-9.49E-04	1.38E-03	-1.39E-04	8.54E-05
1.75	-1.83E-02	1.74E-02	-4.13E-04	1.45E-03	-1.73E-04	8.82E-05
1.80	-2.22E-02	1.99E-02	9.49E-04	1.51E-03	-2.45E-04	9.07E-05
2.00	-3.94E-02	3.03E-02	7.16E-03	1.74E-03	-5.72E-04	9.97E-05
2.20	-7.56E-02	5.35E-02	1.93E-02	1.90E-03	-1.17E-03	1.05E-04
2.40	-9.28E-02	6.45E-02	2.50E-02	2.15E-03	-1.46E-03	1.12E-04
2.50	-9.89E-02	6.83E-02	2.70E-02	2.29E-03	-1.57E-03	1.16E-04
2.70	-1.03E-01	7.05E-02	2.86E-02	2.61E-03	-1.68E-03	1.25E-04
2.80	-1.07E-01	7.27E-02	3.00E-02	2.77E-03	-1.76E-03	1.29E-04
3.10	-1.15E-01	7.64E-02	3.33E-02	3.24E-03	-1.95E-03	1.42E-04
3.20	-1.18E-01	7.82E-02	3.48E-02	3.36E-03	-2.03E-03	1.48E-04
3.30	-1.20E-01	7.90E-02	3.55E-02	3.50E-03	-2.07E-03	1.54E-04
3.40	-1.26E-01	8.31E-02	3.76E-02	3.62E-03	-2.18E-03	1.59E-04
3.50	-1.33E-01	8.75E-02	3.98E-02	3.73E-03	-2.29E-03	1.64E-04
3.60	-1.37E-01	8.99E-02	4.11E-02	3.86E-03	-2.36E-03	1.70E-04
3.70	-1.45E-01	9.51E-02	4.37E-02	3.97E-03	-2.49E-03	1.74E-04
3.80	-1.54E-01	1.01E-01	4.67E-02	4.07E-03	-2.63E-03	1.82E-04
4.00	-1.57E-01	1.03E-01	4.71E-02	4.36E-03	-2.68E-03	6.22E-04
4.10	-1.41E-01	9.24E-02	3.82E-02	5.25E-03	-2.43E-03	3.74E-03
4.30	-1.28E-01	8.36E-02	3.02E-02	7.31E-03	-2.20E-03	5.93E-03
4.35	-1.22E-01	8.00E-02	2.45E-02	1.04E-02	-2.12E-03	7.32E-03
4.40	-1.16E-01	7.62E-02	1.84E-02	1.49E-02	-2.04E-03	7.74E-03
4.45	-1.11E-01	7.27E-02	1.19E-02	2.11E-02	-1.98E-03	7.14E-03
4.50	-9.80E-02	6.41E-02	-6.49E-03	4.36E-02	-2.03E-03	1.71E-03
5.00	-7.07E-02	5.60E-02	-1.22E-02	3.65E-02	-8.30E-03	4.22E-04
6.00	-2.42E-01	2.20E-01	-1.43E-02	5.46E-02	-1.75E-02	6.17E-04
7.00	-3.91E-01	3.66E-01	-1.67E-02	6.57E-02	-2.45E-02	7.43E-04

Table B.10: [Fe/H]= 0.1 and α= 2.50

Mass	M[H]	M[He]	M[C12]	M[N14]	M[O16]	M[C13]
1.00	-1.18E-02	1.18E-02	-5.60E-04	6.53E-04	-6.81E-05	4.93E-05
1.20	-1.44E-02	1.44E-02	-8.21E-04	9.58E-04	-9.61E-05	6.81E-05
1.40	-1.56E-02	1.56E-02	-1.08E-03	1.27E-03	-1.22E-04	8.49E-05
1.60	-1.55E-02	1.55E-02	-1.37E-03	1.60E-03	-1.49E-04	1.01E-04
1.80	-1.64E-02	1.56E-02	-9.31E-04	1.93E-03	-2.20E-04	1.16E-04
2.00	-1.29E-02	1.29E-02	-2.16E-03	2.52E-03	-2.21E-04	1.43E-04
2.50	-9.38E-02	6.36E-02	2.57E-02	2.90E-03	-1.99E-03	1.47E-04
3.10	-1.13E-01	7.35E-02	3.30E-02	4.07E-03	-2.55E-03	1.79E-04
3.20	-1.15E-01	7.46E-02	3.42E-02	4.23E-03	-2.64E-03	1.86E-04
3.30	-1.19E-01	7.71E-02	3.58E-02	4.38E-03	-2.76E-03	1.93E-04
3.40	-1.23E-01	7.92E-02	3.68E-02	4.56E-03	-2.83E-03	2.00E-04
3.90	-1.63E-01	1.05E-01	4.97E-02	5.23E-03	-3.67E-03	2.88E-04
4.10	-1.82E-01	1.17E-01	5.45E-02	5.58E-03	-4.07E-03	1.76E-03
4.20	-1.95E-01	1.26E-01	5.63E-02	6.09E-03	-4.32E-03	3.89E-03
4.30	-2.05E-01	1.32E-01	5.24E-02	9.15E-03	-4.54E-03	8.94E-03
4.40	-2.20E-01	1.42E-01	5.13E-02	1.30E-02	-4.84E-03	1.19E-02
4.50	-2.33E-01	1.50E-01	4.43E-02	2.34E-02	-5.12E-03	1.47E-02
4.60	-2.51E-01	1.62E-01	4.15E-02	3.25E-02	-5.48E-03	1.57E-02
4.70	-2.51E-01	1.62E-01	2.82E-02	5.03E-02	-5.51E-03	1.37E-02
4.80	-2.23E-01	1.43E-01	-3.53E-03	8.72E-02	-5.18E-03	3.83E-03
4.90	-2.19E-01	1.41E-01	5.33E-03	7.18E-02	-4.92E-03	7.21E-03
6.00	-7.96E-02	7.96E-02	-9.03E-03	1.21E-02	-2.53E-03	4.20E-04
7.00	-2.91E-01	2.66E-01	-2.23E-02	7.42E-02	-2.56E-02	8.19E-04

Table B.11: [Fe/H]= 0.2 and α= 2.50

Mass	M[H]	M[He]	M[C12]	M[N14]	M[O16]	M[C13]
1.00	-1.27E-02	1.27E-02	-2.64E-04	3.08E-04	-3.21E-05	2.32E-05
1.50	-1.84E-02	1.82E-02	-3.81E-04	6.88E-04	-7.15E-05	4.49E-05
2.00	-6.48E-02	4.82E-02	1.51E-02	1.03E-03	-5.44E-04	6.01E-05
2.50	-1.05E-01	7.43E-02	2.85E-02	1.43E-03	-9.43E-04	7.27E-05
3.00	-1.21E-01	8.35E-02	3.46E-02	1.94E-03	-1.13E-03	8.54E-05
3.50	-9.93E-02	6.71E-02	2.89E-02	2.41E-03	-9.57E-04	1.05E-04
4.00	-3.76E-02	2.51E-02	-5.13E-03	2.16E-02	-2.58E-03	3.12E-04
4.50	-8.18E-02	7.29E-02	-6.23E-03	2.23E-02	-6.30E-03	2.72E-04
5.00	-1.67E-01	1.55E-01	-6.84E-03	2.92E-02	-9.64E-03	3.45E-04
6.00	-3.38E-01	3.16E-01	-8.02E-03	4.62E-02	-1.60E-02	5.37E-04
8.00	-6.61E-01	6.22E-01	-1.05E-02	7.67E-02	-2.58E-02	9.17E-04

Table B.12: [Fe/H]=-0.1 and α= 2.50

Bibliography

[1] Abia, C., Boffin, H.M.J., Isern, J., and Rebolo, R. 1991, A&A245, L1

[2] Acker, A. 1980, A&A, 89, 33

[3] Acker, A., Marcout, J., Ochsenbein, F. Stenholm, B. and Tylenda, R. 1992, (Garching: ESO)

[4] Adams, S., Seaton, M.J., Howarth, I.D., Auriére, M., and Walsh, J.R. 1984, MNRAS, 207, 471

[5] Afflerbach, A., Churchwell, E., and Werner, M.W. 1997, ApJ, 478, 190

[6] Alexander, D.R. and Ferguson, J.W. 1994, ApJ, 437, 879

[7] Amnuel, P.R. 1993, MNRAS, 261, 263

[8] Amnuel, P.R., Guseinov, O.H., and Rustanov, Yu.S. 1989, Ap&SS, 154, 21

[9] Anders, E. and Grevesse, N. 1989, Geochimica et Cosmochimica Acta, 53, 197

[10] Balick, B. 1987, AJ, 94, 671

[11] Bazan, G. 1991, Ph.d Thesis, University of Illinois

[12] Becker, S.A. and Iben, I. Jr. 1979, ApJ, 232, 831

[13] Becker, S.A. and Iben, I. Jr. 1980, ApJ, 237, 111

[14] Bianchi, L., Ford, H., Bohlin, R., Paresce, F., and De Marchi, G. 1995, A&A, 301, 537

[15] Blöcker, T. 1995, A&A, 297, 727

[16] Blöcker, T. and Schönberner, D. 1991, A&A, 244, L43

[17] Blackwell, S.R. and Burton, C.R. 1981, A&A, 46, 181

[18] Boeshaar, G.O. 1975, ApJ, 195, 695

[19] Boothroyd, A.I. and Sackmann, I.-J. 1988a, ApJ, 328, 632 (BS88a)

[20] Boothroyd, A.I. and Sackmann, I.-J. 1988b, ApJ, 328, 641 (BS88b)

[21] Boothroyd, A.I. and Sackmann, I.-J. 1988c, ApJ, 328, 653

[22] Boothroyd, A.I. and Sackmann, I.-J. 1988c, ApJ, 328, 671 (BS88d)

[23] Boothroyd, A.I. and Sackmann, I.-J. 1992, ApJ, 393, L21

[24] Boothroyd, A.I. and Sackmann, I.-J. 1997, preprint

[25] Boothroyd, A.I. and Sackmann, I.-J. 1993, ApJ, 416, 762

[26] Bowen, G.H. 1988, ApJ, 329, 299

[27] Bowen, G.H. and Willson, L.A. 1991, ApJ, 375, L53

[28] Brosche, P. 1973, A&A, 23, 259

[29] Buell, J.F., Henry, R.B.C, Baron, E., and Kwitter, K. 1997, ApJ, 483, 837

[30] Buell, J.F., Henry, R.B.C., and Baron, E. 1998, in preparation

[31] Busso, M., Gallino, R., Lambert, C.M., Raiteri, C.M., and Smith, V.V. 1992, ApJ, 399, 218

[32] Busso, M., Lambert, D.L., Beglio, L., Gallino, R., Raitieri, C.M., and Smith, V.V. 1995, ApJ, 446, 775

[33] Cahn, J.H., Kaler, J.B., and Stanghellini, L. 1992, A&AS, 94, 399

[34] Caughlan, G.R., Fowler, W.A., Harris, M.J., and Zimmerman, B.A. 1988, Atomic Data and Nuclear Data Tables, 32, 198

[35] Clegg, R.E.S 1991, IAU Symp. 145, G. Michaud and Tutokov, A., Dorecht, Holland: Kluwer Academic Publishers, 139

[36] Corradi, R.L.M. and Schwarz, H.E. 1995, A&A, 293, 871

[37] Costa, R.D.D., Chiappini, C., Maciel, W.J., de Freitas Pacheco, J.A. 1996, A&AS, 116, 249

[38] Dufour, R.J. 1991, PASP, 103, 857

[39] Durell, P.R. and Harris, W.E. 1993, AJ, 105, 1420

[40] Dutra, C.M. and Maciel, W.J. 1990, Rev. Mex. Astr. Astf., 21, 264

[41] Edvardsson, B., Andersen, J., Gustafsson, B., Lambert, D.L., Nissen, P.E., and Tomkin, J. 1993, A&A, 275, 101

[42] Faúndez-Abans, M. and Maciel, W.J. 1987, A&A, 183, 324

[43] Faúndez-Abans, M. and Maciel, W.J. 1988, Revista Mexicana Astron. Astrof., 16, 105

[44] Forestini, M. and Charbonnel, C. 1997, A&A, accepted

[45] Frantsman, J. 1997, A&A, 319, 511

[46] Frost, C.A. and Lattanzio, J.C. 1996, ApJ, 473, 383

[47] Garnett, D. 1995, in: From Stars to Galaxies, ASP Conference Series 98, eds. C. Leitherer, U. Fritze-v. Alvensleben, and J. Huchra, p 543

[48] Gathier, R., Pottasch, S.R., and Goss, W.M. 1983, A&A, 127, 320

[49] Gies, D.R. and Lambert, D.L. 1992, ApJ, 387, 673

[50] Gutman, L. 1954, Psychometrika, 19, 149

[51] Groenewegen, M.A.T. and deJong 1993, A&A, 271, 180

[52] Härm, R. and Schwarzschild, M. 1975, ApJ, 200, 324

[53] Hauschildt, P.H. 1992a, JQSRT, 47, 433

[54] Hauschildt, P.H. 1992b, JQRST, 50, 301

[55] Hauschildt, P.H. 1993, ApJ, 398, 224

[56] Heber, U., Dreizler, S., and Werner, K. 1993, Acta Astronomica, 43, 337

[57] Henry, R.B.C. 1989, MNRAS, 241, 453

[58] Henry, R.B.C. 1990, ApJ, 356, 229

[59] Henry, R.B.C., Kwitter, K., and Howard, J. 1996, ApJ, 458, 215

[60] van den Hoek, L.B. and Groenwegen, M.A.T. 1996, A&A, preprint

[61] Hollowell, D. and Iben, I. Jr. 1988, ApJ, 333, L25

[62] Hollowell, D. and Iben, I. Jr. 1988, ApJ, 340, 966

[63] Hollowell, D. and Iben, I. Jr. 1988, ApJ, 349, 208

[64] Howard, J.W., Henry, R.B.C., and McCartney, S. 1997, MNRAS, in press

[65] Iben, I. Jr. 1964, ApJ, 140, 1631

[66] Iben, I. Jr. 1967, ARA&A, 5, 571

[67] Iben, I. Jr. 1975, ApJ, 196, 525

[68] Iben, I. Jr. 1977, ApJ, 217, 788

[69] Iben, I. Jr. 1982, ApJ, 260, 821

[70] Iben, I. Jr. 1984, ApJ, 277, 333

[71] Iben, I. Jr. 1995, Phys. Rep., 250, 1

[72] Iben, I. Jr., Kaler, J.B., Truran, J.W., and Renzini, A. 1983, ApJ, 264, 605

[73] Iben, I. and Renzini, A. 1983, ARA&A, 21, 271

[74] Iben, I. Jr. and Truran, J.W. 1978, ApJ, 220, 980

[75] Jacoby, G.H. 1996, private communication

[76] Jacoby, G.H., Morse, J., Fullton, L., and Phillips, M. 1995, BAAS, 27, 1417

[77] Kaler, J.B. 1988, PASP, 100, 620

[78] Kaler, J.B. 1985, ARA&A, 23, 89

[79] Kaler, J.B. and Jacoby, G.H. 1989, ApJ, 345, 871

[80] Kaler, J.B. and Jacoby, G.H. 1990, ApJ, 362, 491

[81] Kendall, M.G. 1975, Multivariate Analysis, London: Charles Griffin and Company Limited

[82] Kilian, J. 1992, A&A, 262, 171

[83] Kingsburgh, R.L. and Barlow, M.J. 1994, MNRAS, 271, 257

[84] Kwitter, K.B. and Henry, R.B.C. 1996, ApJ, 473, 304

[85] Kwitter, K.B. and Henry, R.B.C. 1996, ApJ, submitted

[86] Lattanzio, J.C. 1986, ApJ, 311, 708

[87] Lattanzio, J.C. 1989, ApJ, 344, 25

[88] Lattanzio, J.C. 1992, Proc. ASA, 10, 120

[89] Lattanzio, J.C. 1993, in: Planetary Nebulae, Proceedings of IAU Symposium 151. eds. R. Weinberger and A. Acker, 235.

[90] Leisy, P. and Dennefeld, M. 1996, A&AS, 116, 95

[91] Maciel, W.J. and Dutra, C.M. 1992, A&A, 262, 271

[92] Maciel, W.J. and Köppen, J. 1994, A&A, 282, 436

[93] McCarthey, J.K., Mendez, R.H., Becker, S., Butler, K., and Kudritzki, R.-P. 1996, to appear in Proc. IAU Symp. 180: Planetary Nebulae, P.R. Wasselius and H.G.J.M. Lamers eds. (Dordrecht: Kluwer)

[94] McWilliam, A. and Rich, R.M. 1994, ApJS, 91, 749

[95] Meyer, J.P. 1985, ApJS, 27,21

[96] Murtagh, F. and Heck, A. 1987, Multivariate Data Analysis, Dordrecht, Holland: D. Reidel Publishing

[97] Olive, K.A. and Steigman, G. 1995, ApJS, 97, 49

[98] Paczyński, B. 1971, Acta. Astronomia, 21, 417

[99] Pagel, B.E.J., Simonson, E.A., Terlevich, R.J., and Edmunds, M.G. 1992, MNRAS, 255, 325

[100] Pasquali, A. and Perinotto, M. 1993, A&A, 280, 581

[101] Peimbert, M. 1978, IAU Symp. 76, Y. Terzian, Dordrecht, Holland: D. Reidel Publishing, 215

[102] Pottasch, S.R. 1984, Astrophysics and Space Science Lib. No. 107, Planetary Nebulae. Reidel. Dordrecht

[103] Peimbert, M. and Serrano, A. 1980, Rev. Mex. Astr. Af., 5, 9

[104] Perek, L. and Kohoutek, L. 1967, Catalogue of Galactic Planetary Nebula, Prague, Czechoslovokia: Academic Publishing House

[105] Perinotto, M. 1991, ApJS, 76, 687

[106] Ratag, M.A. 1991, Ph.D. Thesis

[107] Reimers, D. 1975, MmRAS, 8, 369

[108] Renzini, A. 1981, in: Physical Processes in Red Giants, I. Iben Jr. ed. (Reidel:Dordrecht) 431

[109] Renzini, A. 1989, in IAU Symposium 131, Planetary Nebulae, S. Torres-Peimbert, ed. (Dordrecht: Kluwer) 391

[110] Renzini, A. 1992, private communication

[111] Renzini A. 1994, A&A, 285, L5

[112] Renzini, A. and Fuci-Pecci 1988, ARA&A, 26, 199

[113] Renzini, A. and Voli, M. 1981, A&A, 94, 175

[114] Rogers, F.J. and Iglesias, C.A. 1992, ApJS, 79, 507

[115] Rola, C. and Stasinska, G. 1994, A&A, 282, 199

[116] Rummel, R.J. 1970, Applied Factor Analysis, Evanston: Northwestern University Press

[117] Sackmann, I.-J. and Boothroyd, A.I. 1992 ApJ, 392, L71

[118] Sackmann, I.-J., Smith, R.L., and Despain, K.H. 1974, ApJ, 187, 555

[119] Scalo, J.M., Despain, K.H., and Ulrich, R.K. 1975, ApJ, 196, 805

[120] Schaller, G., Schaerer, D., Meynet, G., Maeder, A. 1992, A&A, 96, 269

[121] Schneider, S.E., Terizan, Y., Purgathofer, A., and Perinotto, M. 1983, ApJS, 52. 399

[122] Schönberner, D. 1981, A&A, 103, 119

[123] Schönberner, D. 1983, ApJ, 272, 708

[124] Schwarzschild, M. and Härm, R. 1965, ApJ, 142, 855

[125] Schwarzschild, M. and Härm, R. 1967, ApJ, 150, 961

[126] Shaver, P.A., McGee, R.X., Newton, L.M., Danks, A.C., and Pottasch, S.R. 1983, MNRAS, 204. 53

[127] Smith, V.V. and Lambert, D.L. 1989, ApJ, 345, L75

[128] Smith, V.V. and Lambert, D.L. 1990, ApJ, 361, L69

[129] Snow, T.P. and Witt, A.N. 1996, ApJ, L65

[130] Stanghellini, L., Corradi, R.L.M., and Schwarz, H.E. 1993, A&A, 276. 463

[131] Stasińska, G. and Tylenda, R. 1990, A&A, 240, 467

[132] Straniero, O., Chieffi, A., Limongi, M., Busso, M., Gallino, R., and Arlandini, C. 1997, ApJ, 478. 332

[133] Terndrup, D.M. 1988, AJ, 96, 884

[134] Terzian, Y. 1993, in Proceedings of the 155th IAU Symposium, R. Weinberger and A. Acker eds., 109

[135] Tuchman, Y., Glasner, A., and Barkat, Z. 1983, ApJ, 268, 356

[136] Uus, U. 1970 Nauch. Inform. Acad. Nauk., 17. 3

[137] Van Winckel, H. 1997, A&A, 319, 561

[138] Vassiliadis, E. and Wood, P.R. 1993, ApJ, 413, 641

[139] Vassiliadis, E., and Wood, P.R. 1994, ApJS, 92, 125

[140] van der Veen, W.E.C.J. and Habing, H.J. 1990, A&A, 231, 404

[141] Wagenhuber, J. and Weiss, A. 1994, A&A, 286, 121

[142] Walter, D.K., Dufour, R.J., and Hester, J.J. 1992, ApJ, 397, 196

[143] Ward, J.H. 1963, Journal of the American Statistical Association, 58, 236

[144] Webster, B.L. 1988, MNRAS, 230, 377

[145] Weidemann, V. 1987, in Late Stages of Stellar Evolution, S. Kwok and S.R. Pottasch eds. (Dordrecht: Reidel), 347

[146] Weidemann, V. and Koester, D. 1983, A&A, 121, 77

[147] Weigert, A. 1966, Z. Ap., 64, 395

[148] Whitelock, P. 1992, IAU Symposium 153, DeJonghe, H. and Habing, H.J., Dordrecht: Kluwer Academic Publishers, 39

[149] Whitmore, B.C. 1984, ApJ, 278, 61

[150] Wood, P.R. and Zarro, D.M. 1981, ApJ, 247, 247

[151] Wilson, L.A., Bowen, G.H., and Struck, C. 1996, in: From Stars to Galaxies, ASP Conference Series 98, eds. C. Leitherer, U. Fritze-v. Alvensleben, and J. Huchra, p 197

IMAGE EVALUATION
TEST TARGET (QA-3)

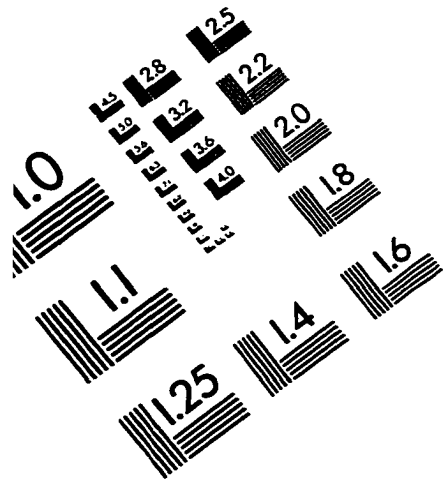

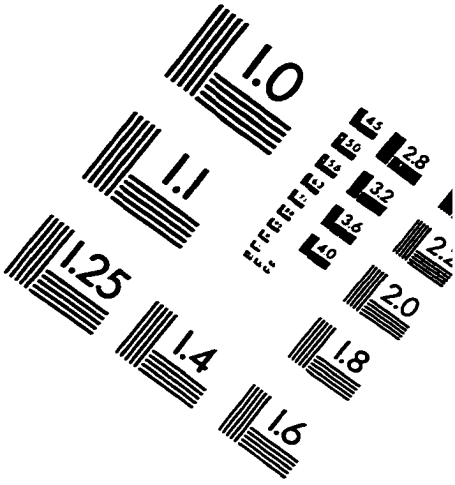

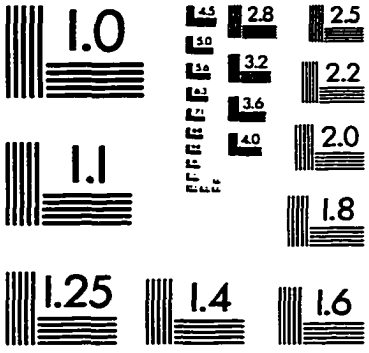

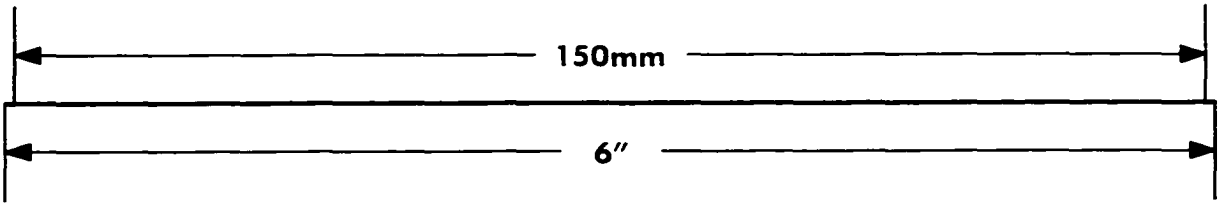

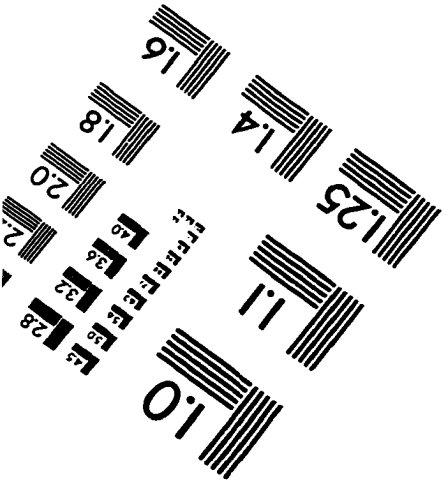

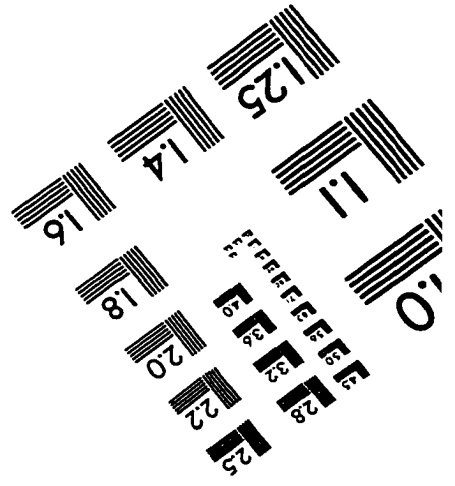

APPLIED IMAGE, Inc
1653 East Main Street
Rochester, NY 14609 USA
Phone: 716/482-0300
Fax: 716/288-5989

© 1993, Applied Image, Inc., All Rights Reserved